BRNO UNIVERSITY OF TECHNOLOGY
VYSOKÉ UČENÍ TECHNICKÉ V BRNĚ

FACULTY OF ELECTRICAL ENGINEERING AND COMMUNICATION
FAKULTA ELEKTROTECHNIKY
A KOMUNIKAČNÍCH TECHNOLOGIÍ

DEPARTMENT OF PHYSICS
ÚSTAV FYZIKY

NOISE, TRANSPORT AND STRUCTURAL PROPERTIES OF HIGH ENERGY RADIATION DETECTORS BASED ON CDTE
TRANSPORTNÍ, ŠUMOVÉ A STRUKTURÁLNÍ VLASTNOSTI DETEKTORŮ VYSOKOENERGETICKÉHO ZÁŘENÍ NA BÁZI CDTE

DOCTORAL THESIS
DIZERTAČNÍ PRÁCE

AUTHOR — **Ing. Ondřej Šik**
AUTOR PRÁCE

SUPERVISOR — **prof. Ing. Lubomír Grmela, CSc.**
ŠKOLITEL

BRNO 2016

Abstract

Because of demands from space research, healthcare and nuclear safety industry, gamma and X-ray imaging and detection is rapidly growing topic of research. Improved manufacturing technology of CdHgTe that is primarily for infrared imaging, gave the possibility of development of a new semiconductor material with high atom number, relatively high density and wide bandgap: CdTe and its alloy CdZnTe. These materials are suitable to detect high energy photons in range from 10 - 500 keV. Their 1.46 -1.6 eV band gap gives the possibility of high resistivity crystals production that is high enough for room temperature X-ray detection and imaging.

CdTe/CdZnTe detectors under various states of their defectiveness were used in my work. Investigation of detector grade crystals, crystals with lower resistivity and enhanced polarization, detectors with asymmetry of electrical characteristics and thermally degenerated crystals were subject of my work in terms of analysis of their current stability, additional noise, electric field distribution and structural properties. The results of the noise analysis showed that enhanced concentration of defects resulted into change from monotonous $1/f$ noise to spectrum that showed effects of generation-recombination mechanisms. Next important feature of w quality of investigated samples was higher increase of the noise power spectral density than 2 with increasing applied voltage. Structural and chemical analyses showed diffusion of metal material and trace elements deeper to the crystal bulk. Part of this work is also focused on surface modification by argon ion beam and its effect on chemical and morphological properties of the surface.

Keywords: CdTe, CdZnTe, thermal degradation, noise, metal-semiconductor junction, elemental concentration depth profile, surface modification, heterostructure, polarization, electric field distribution, SIMS, XPS, Auger, XRD, ion bombardment.

Abstakt

Poptávka ze strany vesmírného výzkumu, zdravotnictví a bezpečnostního průmyslu způsobila v posledních letech zvýšený zájem o vývoj materiálů pro detekci a zobrazování vysokoenergetického záření. Vylepšená technologie CdHgTe, který je primárně určen pro operaci infračervené oblasti umožnila vývoj polovodičového materiálu s vysokým atomovým číslem, vysokou hustotou a širokou šířkou zakázaného pásma: CdTe and CdZnTe. Tyto polovodiče umožnují detekci záření o energiích v rozsahu 10 - 500 keV. Šířka zakázaného pásma u CdTe / CdZnTe je 1.46 -1.6 eV, což umožňuje produkci vysokoodporových krystalů vhodných pro použití CdTe / CdZnTe při pokojové teplotě.

V mé práci byly zkoumány detektory CdTe/CdZnTe v různých stádiích jejich poruchovosti. Byly použity velmi kvalitní spektroskopické detektory, materiál s nižší rezistivitou a výraznou polarizací, detektory s asymetrií elektrických parametrů kontaktů a teplotně degenerované vzorky. Z výsledků analýzy nízkofrekvenčního šumu je patrný obecný závěr, že zvýšená koncentrace defektů způsobí změnu povahy původně monotónního spektra typu $1/f$ na spektrum s výrazným vlivem generačně-rekombinačních procesů. Další výrazná vlastnost degenerovaných detektorů a detektorů nižší kvality je nárůst spektrální hustoty šumu typu $1/f$ se vzrůstajícím napájecím napětí se směrnicí výrazně vyšší než 2. Strukturální a chemické analýzy poukázaly, že teplotní generace detektorů způsobuje difuzi kovu použitého při kontaktování a stopových prvků hlouběji do objemu krystalu. Část mé práce je věnována modifikaci povrchu svazkem argonových iontů a jejímu vlivu na chemické složení a morfologii povrchu.

Klíčová slova CdTe, CdZnTe, teplotní degradace, šum, přechod polovodič-kov, hloubkový profil prvkového složení, modifikace povrchu, heterostruktura, polarizace, rozložení elektrického pole, SIMS, XPS, Auger, XRD, bombardování ionty

ŠIK, O. *Transportní, šumové a strukturální vlastnosti detektorů vysokoenergetického záření na bázi CdTe.*. Brno: Vysoké učení technické v Brně, Fakulta elektrotechniky a komunikačních technologií, 2016. 95 s. Vedoucí disertační práce prof. Ing. Lubomír Grmela, CSc.

DECLARATION

I declare that I have written my doctoral thesis on the theme of " Noise, transport and structural properties of high energy radiation detectors based on CdTe " independently, under the guidance of the doctoral thesis supervisor and using the technical literature and other sources of information which are all quoted in the thesis and detailed in the list of literature at the end of the thesis. As the author of the doctoral thesis I furthermore declare that, as regards the creation of this doctoral thesis, I have not infringed any copyright. In particular, I have not unlawfully encroached on anyone's personal and/or ownership rights and I am fully aware of the consequences in the case of breaking Regulation § 11 and the following of the Copyright Act No 121/2000 Sb., and of the rights related to intellectual property right and changes in some Acts (Intellectual Property Act) and formulated in later regulations, inclusive of the possible consequences resulting from the provisions of Criminal Act No 40/2009 Sb., Section 2, Head VI, Pt. 4.

Brno, 24th August 2016 ……

Ondřej Šik

\

Acknowledgements

I would like to thank prof. Ing. Lubomír Grmela, CSc. For his supervision of my work. Furthermore, my gratitude also goes to all members of the Department of Semiconductors and Semiconductor Optoelectronics at the Institute of Physics, Charles university, for supply of samples and fruitful discussion during my whole study. Next, I would like to thank Prof. Paul Sellin, Dr.Annika Lohstroh and Dr. Michael Hodgson for the great opportunity to carry out the Time-of-Flight experiments at the University of Surrey, UK. I also thank to Dr. Adriano Cola, Dr. Isabella Farella and Dr. Jerome Pousset from the National Research Council, Institute of Microelectronic and Microsystems in Lecce, Italy for guidance during my fellowship.

Research described in this thesis was financially supported by the European Centre of Excellence CEITEC 2020 LQ1601, by project Sensor, Information and Communication Systems SIX CZ.1.05/2.1.00/03.0072.

Ondřej Šik

Faculty of Electrical Engineering
and Communication
Brno University of Technology
Purkynova 118, CZ-61200 Brno
Czech Republic
http://www.six.feec.vutbr.cz

PODĚKOVÁNÍ

Výzkum popsaný v této doktorské práci byl realizován v laboratořích podpořených z projektu SIX; registrační číslo CZ.1.05/2.1.00/03.0072, operační program Výzkum a vývoj pro inovace.

Brno ....

(podpis autora)

EVROPSKÁ UNIE
EVROPSKÝ FOND PRO REGIONÁLNÍ ROZVOJ
INVESTICE DO VAŠÍ BUDOUCNOSTI

Contents

1 Introduction 6

2 State of art 7

2.1 Basic physical parameters of CdTe / CdZnTe 7

2.2 Crystal growth 7

2.3 Contacts 9

2.3.1 Physical definition of metal-semiconductor contact 10

2.4 Surface 15

3 Noise in the semiconductor optical devices 17

3.1 Thermal noise 18

3.2 Shot noise 18

3.3 Generation-Recombination noise 20

3.4 1/f noise 22

3.4.1 Hooge's model 23

3.4.2 McWhortel's Model 24

3.4.3 Models validity: The problem of Number vs. Mobility fluctuations 25

4 Experimental part – electrical characterization 26

4.1 Localization of the noise sources in CdZnTe detector system 26

4.1.1 *I-V* characteristics analysis: Separation of bulk and surface leakage current 27

4.1.2 Noise power spectral density Analysis: separation of noise sources 28

4.2 Analytical investigation of bias induced polarization in CdZnTe detectors 31

4.2.1 Electric field distribution in the sample 33

4.2.2 Current instability measurements and parameters retrieval of the structure 34

4.2.3 Investigation of 1/*f* noise evolution during polarization 35

4.3 Analysis of the contact symmetry and its impact on the low frequency noise. 36

4.3.1 Current-Voltage characteristics asymmetry 37

4.3.2 Comparison of the noise properties of asymmetric contacts 38

5 Investigation of thermal stress effect on CdTe detectors 39

5.1 Effect of high temperatures on transport characteristics 40

5.2 Effect of high temperatures on noise properties 42

5.3 Structural and morphological investigation of Metal- Semiconductor interface of CdTe detector exposed to heat stressing. 44

5.3.1 X-ray photoemission analysis 44

5.3.2 XPS depth profiling of the M-S structure 55

5.3.3 Secondary Mass Ion Spectroscopy depth profiling 64

5.3.4 Morphological, SEM, AES and XRD study of craters after depth profiling 68

5.4 Analysis of the effect of thermal stressing on charge transport properties by Schottky theory . 76

6 Investigation of the effect of the argon ion beam on CdZnTe single crystals surface structural properties 77

6.1 SEM study of irradiated areas 78

6.2 AFM study of irradiated areas 81

6.3 XPS study of irradiated areas 84

7 Conclusion 86

8 References 89

Curriculum Vitae 95

List of figures:

Figure 2.1: Energy diagram of the most common defects in CdTe. V_{cd} is a Cd vacancy and its ionization states denoted by sign, Te_{Cd} is an interstitial defect. Cd_I^{2+} is a deep donor that appears after high temperature annealing or Te. Data taken from [6]. 9
Figure 2.2: Work functions of metals (in vacuum). Image taken from [9]. 13
Figure 2.3: Energy band diagram of Au and an n-type CdTe connection. 13
Figure 2.4: Energy band diagram of Au and an n-type CdTe contact at equilibrium at zero bias (left) and energy band diagram of Au and an n-type CdTe contact with applied external potential in reverse polarity (right). 14
Figure 2.5: Energy band diagram for an Au MIS junction on n-CdTe with native oxide as the insulator. Units are in electronvolts. 15
Figure 3.1: Typical subscription of noises sources in photodetector. a) Noise due to the relaxation of material defects ($1/f^{-2}$), b) Generation recombination noise or thermal relaxation noise, c) Shot noise or photon noise, d) $1/f$ noise. 17
Figure 3.2: Distribution of time constants for traps for the McWhortel model. 25
Figure 4.1: Current – voltage characteristics of the detector without connected guard ring (left) and with connected guard ring (right). 28
Figure 4.2: The low frequency noise spectra of the detector with disconnected guard ring electrode. Reverse biased contact A (left), reverse biased contact B (right). 29
Figure 4.3: Low frequency noise spectra of the detector with connected guard ring electrode. Reverse biased contact A (left), reverse biased contact B (right). 29
Figure 4.4: Dependence of power spectral density of the noise signal on the applied bias voltage at $f = 10$ Hz. Configurations with and without connected guard ring electrode are shown. 30
Figure 4.5: Pockels effect experimental setup. Collimated testing light cut by narrow band filter at 980 nm passes through the biased sample situated between two crossed polarisers is sensed by NIR InGaAs CCD camera. Excitation radiation (laser or X-rays) passes through semi-transparent cathode. 32
Figure 4.6: Distribution of the electric field with time through the sample acquired by the Pockels effect measurements. 34
Figure 4.7: Left: Linear relationship between electric field and the square root of the applied voltage. Right*:* Electric field decay at different bias at $x = 0.059$ mm from the anode. 34
Figure 4.8: Current stability of studied sample at 100 V. 35
Figure 4.9: Noise spectral density evolution during polarization of the analyzed detector (left) and an increase of the noise spectral density with current. Applied voltage was 100 V. 35
Figure 4.10: Current- Voltage characteristics of the “poss” (left) and of the “neg” (right) biased detector. Operating temperatures were 305 K, 315 K and 325 K. 37
Figure 4.11:Comparison of the Low frequency noise spectra of the detector for both bias orientations. The applied bias was ±25 V, measured at temperature 305 K. Black line denotes noise background. 38
Figure 4.12:The values of the. noise spectral density of sample at frequency $f = 10$ Hz vs. applied voltage. “poss” (left) and “neg” (right) bias voltage orientation. Temperatures were 305 K, 315 K and 325 K..... 38
Figure 5.1: The I-V characteristics of detector before (left) and after (right) exposure to 400K for 48 h. 40
Figure 5.2:Current transients after the detector biasing of the detector before thermal stressing. Applied voltage was 20 V. 41
Figure 5.3: Current transients after the detector biasing of the detector after thermal stressing. Applied voltage was 20 V. 41

Figure 5.4: Low frequency noise spectra of the detector before(left) and after(right) thermal stressing. Applied voltages were 88 V, 63 V and 50V 42
Figure 5.5: Dependence of the power spectral density of the noise signal on the applied bias voltage at f = 10 Hz..... 43
Figure 5.6: A simplified explanation of the atom ionisation by emission of electron from its core level. 45
Figure 5.7:Survey (wide) XPS spectrum of the unstressed sample. 47
Figure 5.8:Survey (wide) XPS spectrum of the stressed sample. 48
Figure 5.9:The detail scan of the Te 3d 5/2 photoemission peak. The spectrum of the unstressed sample is on the left. 49
Figure 5.10:The detail scans of the Cd 3d photoemission peak. The spectrum of the unstressed sample is on the left. 50
Figure 5.11: Detailed scans around binding energy of oxygen on surface Au-CdTe interfacial structure. Spectrum for thermally stressed sample are on the right, the ustressed sample is on the left. 52
Figure 5.12: Secondary (left) and backscattered (right) emission micrographs of unstressed detector after gold layer removal by argon sputtering. Horizontal lines denote existence of grain boundaries in the detector bulk. SE and BSE are slightly shifted due to charging effect of semi-insulating CdTe. 53
Figure 5.13: Detailed scans around binding energy of oxygen on surface Au-CdTe interfacial structure. Spectrum for thermally stressed sample are on the right, non-stressed sample is on the left. 54
Figure 5.14:SEM image of gold surface exposed to molecular oxygen (B) and a part covered from exposition to oxygen (A). Image taken from [55]..... 55
Figure 5.15: Survey XPS spectra during depth profiling of the unstressed sample. 57
Figure 5.16:Survey XPS spectra during depth profiling of the stressed sample. 57
Figure 5.17:The depth profile of the detail scans of the O 1s photoemission peak. The spectrum of the unstressed sample is on the left. 58
Figure 5.18:Depth profile of the detail scans of the Cd 3d photoemission peak. The spectrum of the unstressed sample is on the left. 59
Figure 5.19:Comparison of chemical shifts of the Cd 3d photoemission peaks with the atomic content of Cl and Te sub-oxide. The unstressed sample is on the left. 59
Figure 5.20: Depth profile of the detail scans of the Te 3d photoemission peak. The spectrum of the unstressed sample is on the left. 60
Figure 5.21:Depth profiles of atomic concentrations of Te in its metallic form, oxidized form and sub-oxide form. The unstressed sample is on the left. 61
Figure 5.22: Depth profile of the detail scans of the Au 4f photoemission peak. The spectrum of the unstressed sample is on the left. 62
Figure 5.23:XPS depth profile of the M-S interface of the unstressed sample. 63
Figure 5.24:XPS depth profile of the M-S interface of the stressed sample. 63
Figure 5.25:Typical schematics of the functional principle of a ToF-SIMS instrument and options for surface and bulk analysis of solid catalyst samples by (i) mass spectrometric analysis of surface borne secondary ions, (ii) imaging of the lateral distribution of secondary ions, and (iii) sputter depth profiling. Image taken from [60]. 65
Figure 5.26: 3D ToF SIMS profiles of Au, Cd,Te, Cl, In and Na of the unstressed sample. 67
Figure 5.27: 3D ToF SIMS profiles of Au, Cd, Te, Cl, In and Na of the stressed sample. 67
Figure 5.28: SEM micrographs of the surface after depth profiling. Unstressed sample is on the left. 69
Figure 5.29: SEM micrograph taken on Ultra High Resolution microscope. Black spots on the crater show their solidity. 70
Figure 5.30: SEM micrograph of AES scanned spot in black square. The change of the contrast at AES scan area is caused by the sample charging. Right: Typical AES spectrum. 70
Figure 5.31: Auger maps of Cd (left) and Te (right) of area indicated in Fig. 5.30. Colour closer to white stands for higher concentration. 71
Figure 5.32: AFM scan of the sputter crater of the non-stressed sample. 72
Figure 5.33:AFM scan of the sputter crater of the stressed sample. 72
Figure 5.34: Constructive interference of X-rays in the crystal structure 73
Figure 5.35: Bragg-Brentano configuration for XRD measurements. 74
Figure 5.36: X-ray diffraction patterns of both samples. For sake of readiness, the pattern of the unstressed sample is divided by 1000 and vertically shifted. 75
Figure 5.37: I-V characteristics of stressed and unstressed samples (left). Right picture: Transformed ln(J)-V curves for low biases of each sample. 76
Figure 6.1: SEM images of CdZnTe surface a) freshly etched before ion irradiation b) After Ar^+ ion fluence 3.7×10^{15} Ar^+ ions / cm^2, c) 7×10^{15} Ar^+ ions / cm^2, d) 1.4×10^{16} Ar^+ ions / cm^2, e) 4.9×10^{16} Ar^+ ions / cm^2 and f) 2×10^{17} Ar^+ ions / cm^2..... 80

Figure 6.2: 3D AFM images of CdZnTe surface a) freshly etched before ion irradiation b) After Ar^+ ion fluence 3.7 $\times 10^{15}$ Ar^+ ions / cm^2, c) 7 $\times 10^{15}$ Ar^+ ions / cm^2, d) 1.4 $\times 10^{16}$ Ar^+ ions / cm^2, e) 4.9 $\times 10^{16}$ Ar^+ ions / cm^2 and f) 2 $\times 10^{17}$ Ar^+ ions / cm^2 82
Figure 6.3:Dependence of the surface RMS roughness (squares) and the sputter rate (dots) on ion dose. 83
Figure 6.4: Map of relative concentration of Te to Cd+Zn. Craters are marked by numbers (left). Signal from the center of the crater was averaged and plotted depending on the ion dose (right). Spot 9 was used for calibration and as an orientation point. 84
Figure 6.5: Map of relative concentration of C to Te and Cd. Relative concentration of C in craters is ~ 2% and outside of the crater the concentration reaches ~ 18%. 85

List of used symbols:

a	Lattice constant	m_n	Effective mass of electrons
A^*	Effective Richardson constant	N	Total number of carriers
A_{coll}	Collection area	n	Concentration of electrons, diffraction maximum order
at%	Atomic concentration	n_0	Average concentration of electr.
Cd_I^{2+}	Doubly charged Cd	N_0	Average concentration of N
CdTe	Cadmium Telluride	N_a	Concentration of acceptors
CdZnTe	Cadmium-Zinc Telluride	N_c	Effective density of states in conduction band
C_n	Cross section of electrons	N_d	Concentration of donors
C_p	Cross section of holes	n_i	Concentration of intrinsic carriers
d	Interplanar distance	N_t	Trap concentration
e	Elementary electron charge	N_v	Effective density of states in valence band
E_A	Acceptor energy level	p_0	Average concentration of holes
E_a	Activation energy	P_{opt}	Optical power
E_C	Conduction band energy	R_p	Recombination rate of holes
E_D	Donor energy level	R_n	Recombination rate of electrons
E'_F	Fermi energy	R	Electric resistance
E_g	Band gap	$R(z)$	Recombination rate of all carriers
E_k	Kinetic energy	r_{41}	Linear optoelectric coefficient
E_t	Trap level energy	$\mathbf{S}$	Spin vector
E_v	Valence band energy	$S_{1/f}$	Spectrum of $1/f$ noise
E_{vac}	Vacuum level energy	$S_{1/f\hat{}2}$	Spectrum of noise related to material defect relaxation noise
G_n	Generation rate of electron	S_{amp}	Noise of amplifier
G_p	Generation rate of hole	S_{GR}	Generation-Recombination noise
$G(z)$	Generation rate of all carriers	S_i	Current power spectral density
h	Planck constant	S_{shot}	Shot noise
$H(f)$	Transfer function	S_U	Voltage power spectral density
I	Electric current	S_x	Fourier Transformation of power spectral density
I_0	Saturation current	T	Thermodynamic temperature, period
I_g	Generation Current	Te_{Cd}	Interstitial defect
I_{ph}	Photon current	U	Bias voltage
I_r	Recombination current	U_{12}	Voltage drop on forward biased metal-semiconductor interface
$\mathbf{J}$	Total angular momentum	U_d	Temperature gradient of pn junction
J	Current density	V_{bi}	Built-in potential
J_s	Saturation current density	V_{bif}	Forward biased potential
k	Bolzmann constant	V_{bir}	Reverse biased potential
$\mathbf{L}$	Orbital angular momentum	V_{Cd}	Cadmium vacancy
L_d	Depletion layer length	V_{ext}	Extrenal potential
m	Slope of the $1/f$ current	W	Space charge region width
m_{dh}	Effective mass of holes	$U(z)$	Difference between generation and recombination rate

List of used symbols (Greek alphabet)

μ_e	Electron mobility	ε_0, ε_r	Permittivity of vacuum and relative permittivity
μ_h	Hole mobility	ϕ_b	Potential barrier height
τ_e, τ_n	Electron lifetime	ϕ_s	Work function of semiconductor
τ_h, τ_p	Hole lifetime	ϕ_m	Work function of metal
χ	Electron affinity	η	Quantum efficiency
ω	Angular velocity, angle between X-ray and sample in XRD	ρ	volumetric mass density
θ	Bragg angle	Δ	Fluctuation of specific quantity
Φ_{ph}	Photon flux	ΔE_{sm}	energy barrier between semiconductor and metal
α	Hooge constant	ΔE_{ms}	energy barrier between metal and semiconductor
σ	Conductivity, trap cross section	Δf	Frequency band
φ	Contact potential, field potential function	μ'_{Fp}	$E_F - E_v$
λ	wavelength	μ'_{Fn}	$E_F - E_c$-

List of abbreviations

AES	Auger Electron Spectroscopy	LTI	Linear-Time-Invariant system
AFM	Atomic Force Microscopy	M	Metal
BE	Binding Energy	NIR	Near InfraRed
BM	Bridgman Method	p-i-n	Positive-Intrinsic-Negative
BSE	BackScattered Electrons	RF	Rodio Frequency
C	Czochralski method	RMS	Root-Mean-Square
CCD	Charge-Coupled Device	RSF	Relative Sensitivity Factor
const	constant	S	Semiconductor
CPS	Counts Per Second	SEM	Secondary Emission Microscope
CVD	Chemical Vapour Deposition	SIMS	Secondary Ion Mass Spectroscopy
FWHM	Full Width at Half Maximum	THM	Travelling Heater Method
GPIB	General Purpose Interface Bus	ToF	Time-of-Flight
GR	Generation-Recombination, GuardRing electrode	UHV	Ultra High Vacuum
H_2T-VPE	H_2 Transport Vapour Phase Epitaxy	USB	Universal Serial Bus
HPB	High Pressure Bridgman	VGF	Vertical Gradient Freeze
I-V	Current-Voltage characteristics	XPS	X-ray Photoemission Spectroscopy
LPB	Low Pressure Bridgman	XRD	X-Ray Diffraction

1 Introduction

Because of demands from space research, healthcare and nuclear safety industry, gamma and X-ray imaging and detection is rapidly growing topic of research. Many materials are studied to develop detectors with high stopping power, high spectral resolution and capability of imaging. Because of its high atomic number and high density, scintillators are frequent instrumentation for X-ray sensing. Nevertheless, their biggest disadvantage is the low spectral resolution. Furthermore, conversion of radiation into electric signal is indirect and expensive photomultipliers are needed. Semiconductors offer the benefit of direct conversion, have presumptions to give excellent spectral resolution and well developed lithographic technologies predestine semiconductors as a successful candidate for X-ray imaging.

Most common semiconducting materials like Si, Ge can provide good energy resolution, but Si offers low stopping power and Ge has small band gap that requires cryogenic conditions for operation. Improved manufacturing technology of CdHgTe that is primarily for infrared imaging, gave the possibility for development of a new semiconductor material with high atom number, relatively high density and wide bandgap – CdTe /and its alloy CdZnTe. These materials are suitable to detect high energy photons in range from 10 keV to 500 keV. Their 1.46 -1.6 eV band gap gives the possibility of high resistivity (10^{10}-10^{11} Ωcm) crystals production that is high enough for room temperature operation. Even though research of CdTe / CdZnTe started in 1970s, the most significant progress in crystal quality and better availability of CdTe / CdZnTe on the market happened in recent years.

In spite of recent progress, the quality of CdTe CdZnTe detectors is still far from perfect. Compared to Si, CdTe / CdZnTe crystals exhibit higher concentration of defects. It is difficult to obtain large volume (>1 cm^3) crystals suitable for > 500 keV photons detection. Large work function of CdTe / CdZnTe and not well defined properties of the surface brings difficulties in proper crystal metallization. From these imperfections, three basic issues arise for CdTe / CdZnTe detectors: i) lower resistance of the detector than the theoretical one, ii) higher additive noise and iii) instability of spectral sensitivity and electrical parameters in time. Such difficulties limit the performance, especially for operation under high fluxes of radiation.

Above mentioned facts led me to investigate the properties of CdTe/CdZnTe detectors under various states of their defectiveness. Investigation of detector grade crystals, crystals with lower resistivity and enhanced polarization, detectors with asymmetry of electrical characteristics and thermally degenerated crystals were subject of my work in terms of analysis of their current stability, additional noise, electric field distribution and structural properties.

2 State of art

CdTe based radiation detector are a system, whose parameters are affected by three key parts: i) Detector active volume (Crystal), ii) Points of biasing and signal extraction (metal contacts) and iii) Detector surface. All of these have crucial effect on the properties of the detector and none of them can be neglected in the manufacturing process and analysis. This chapter is dedicated to inform about function and properties of each basic part of the detector system.

2.1 Basic physical parameters of CdTe / CdZnTe

CdTe is a Compound semiconductors derived from elements of groups II (Cd)and VI (Te). For X-ray detection CdHgTe is a good material for infrared detectors. Content of Hg can be used to adjust desired band gap from 0 eV (HgTe) to 1.5 eV (CdTe). $Cd_xZn_{1-x}Te$ and $Cd_xMn_{1-x}Te$ are nowadays in field of interest for X-ray detection and imaging.

Table 1: Typical physical properties of compound semiconductors. Growth methods abbreviations are C = Czochralski, CVD = chemical vapor deposition, THM = traveler heater method, BM = Bridgman method, HPB = high-pressure Bridgman [1].

Material	Si	Ge	GaAs	CdTe	$Cd_{0.9}Zn_{0.1}Te$
Crystal structure	Cubic	Cubic	Cubic ZB	Cubic ZB	Cubic ZB
Growth method	C	C	CVD	THM, BM	HPB THM
Atomic number	14	32	31, 33	48, 52	48, 30, 52
Density (g/cm^3)	2.33	5.33	5.32	6.2	5.78
Band gap (eV)	1.12	0.67	1.43	1.44	1.57
p^+ e^- energy (eV)	3.62	2.96	4.2	4.43	4.6
Resistivity (Ω cm)	10^4	50	10^7	10^9	10^{10}
$\mu_e\tau_e$ (cm^2/V)	> 1	> 1	10^{-5}	10^{-3}	10^{-3} - 10^{-2}
$\mu_h\tau_h$ (cm^2/V)	~ 1	> 1	10^{-6}	10^{-4}	10^{-5}

Table 1 shows basic physical properties of semiconductors. Reasonable electron mobility ~1000 cm/Vs and the mobility- lifetime product ~10^{-3} cm^2/V mm are good preconditions for a spectroscopic X-ray detector made from CdTe / CdZnTe.

2.2 Crystal growth

Development of high-resistivity single crystals (ρ = 10^{10} Ωcm) is done by optimization of the crystal growth technologies based on traditional melt-growth or vapour-growth techniques. During the past few years, crystals show decreasing concentration of impurities and better homogeneity of material properties. Substrate alloyed with added zinc ($Cd_xZn_{1-x}Te$) shows higher uniformity of grown crystals, leading to easier production of large volume detectors. The most successful ones are [2]:

Vapour growth methods are based on the **Basic Bridgman method**. This method involves the movement of a crucible containing the melt through a furnace designed to provide a desirable temperature profile. The furnace may be either vertical or horizontal. The crucible may be transported through the heater, or the crucible stationary with a moving heater, or alternatively, both stationary and the temperature profile altered by a programmed temperature controller. The last mentioned method is known as Vertical gradient freeze method. Is a variation of the Bridgman method. This method is used for at the crystal growth laboratory of the Institute of Physics of Charles University and most of the samples used in this work were grown by this method. Unlikely to classical vertical BM, both the crucible and heater are stationary while the necessary temperature gradient is ensured by electronically-controlled heating coils

In the **High Pressure Bridgman method** (HPB), an over-pressure of 10 ± 150 atm of an inert gas, typically argon is maintained over the melt to suppress the loss of volatile components. While the elevated pressure reduces the loss of these components, the losses are not eliminated. Continuous losses of cadmium, the highest vapour pressure component, causes the melt to become enriched in tellurium during growth Before initiation of the growth cycle, the charge is heated in a programmed schedule. Following the growth phase the crystal is gradually brought to room temperature and ambient pressure. The crystal grows at high temperature, above 1100^0 C and the growth rate varies around 0.1-1 mm per hour. The complete growth cycle is 3-4 weeks. High concentration of crystal flaks limits the yield of large $>1cm^3$ devices from the crystal is only around 10%.

Low pressure Bridgman (LPB) method also succeeded in production of spectrometer grade crystals. Two basic varieties are used. i) Horizontal LPB has possible advantages, given by perpendicular orientation of the crystal growth to the growth axis. The growth interface is not exposed to the load of liquid phase. Furthermore, the geometry allows better stoichiometry control by metal vapors between liquid and solid phases of the solution. The modified horizontal LPB with a stationary load and furnace with electronically controlled thermal gradient and Cd vapor control during the crystal growth showed good results. This modification has 25-30 % for 2×2 cm3 wafers. On the other hands side, apart from HPB, the photoluminescence measurements show strong donor-to-acceptor recombination that degrade spectral sensitivity of such grown crystals. Growth rates vary but are typically in region of 0.1 ± 1 mm/h

Travelling heater method (THM) is probably the most often used method of the CdTe / CdZnTe crystals growth used by commercial vendors, such as ACRORAD [3] and REDLEN [4]. In this method, the crystals grow from tellurium solution. The melting point of is usually set to 650°C by control of Cd to Te ratio. A moving RF heating coil is used to melt a narrow region of the crystal and as a segregator of impurities, which are pushed to ends of the ingot. This method produces high quality crystals, but growth of the crystals, is very slow: approx. 15mm a day for an ingot with diameter of 7.5 cm [3].

A new attitude to detector substrate production has recently appeared: growth of thick CdTe epitaxial layers by the hydrogen transport **Vapour phase epitaxy** (H_2T-VPE)

[5]. (100)-oriented CdTe epilayers are successfully grown by H_2T-VPE on hybrid ZnTe / GaAs (100) substrates prepared by metal organic vapour phase epitaxy. Growth rates are up to 10 μm / h. H_2T-VPE is a potential alternative to traditional melt- and vapour-growth methods for the synthesis of detector-grade CdTe for application for the 1 – 50 keV X-ray energy range.

CdTe crystallises into Zinc-Blende structure, which is a combination of two face-centred cubic lattices shifted to each other by Miller indices (¼, ¼, ¼). Such structure makes growth of CdTe / CdZnTe is much more difficult than it is for Si. Complicated crystal arrangement result into more frequent lattice defects. Probably the most common crystal defects are Cd vacanci V_{Cd} that acts as an acceptor due to missing electrons from the Cd atom. This defect is compensated by doping with Cl, In and others. Te_{Cd} is the Te antisite that has the opposite effect from V_{Cd} and acts as a donor. Band diagram of these defects is sketched in Fig. 2.1.

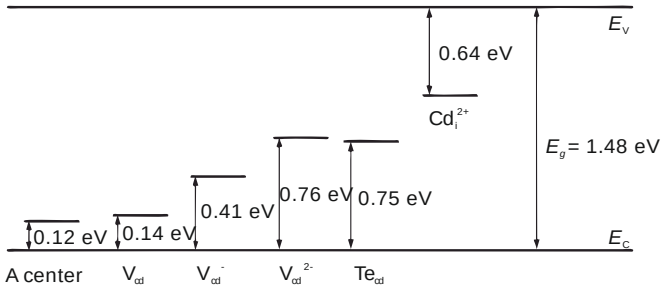

Figure 2.1: Energy diagram of the most common defects in CdTe. V_{cd} is a Cd vacancy and its ionization states denoted by sign, Te_{Cd} is an interstitial defect. Cd_I^{2+} is a deep donor that appears after high temperature annealing or Te. Data taken from [6].

Beside lattice defects, charge transport and spectroscopic performance is also limited by macroscopic defects like **Dislocation networks**, which are result of thermal stress during solidification and cooling down. **Grain boundaries** can be formed during crystal growth at high temperature gradients or high growth speeds. Normally, the grain boundaries are introduced at the very early stage of crystal growth when the nucleation of numerous grains appears, or resulting from the instabilities at the growth interface**. Te inclusions / precipitates** generally are originated from the morphological instabilities at the growth: Te-rich melt droplets are captured from the boundary layer before the melt interface.

2.3 Contacts

Metallization of the crystals have also crucial effect on the detector performance. The nature of interface formation between CdTe/CdZnTe and metal results in formation of Ohmic or Schottky contacts. Improper interface reactions often result into degeneration of the contact. This can lead to lowering of rectification efficiency for Schottky contacts and for all cases, creation of trapping centers and sources of additive noise in the detector system. On the other hand, some interfacial layers can be beneficial: CdTe detectors based

on homoepitaxial p–i–n diode structures, in which the intrinsic part is a high-resistivity (detector-grade) bulk crystal, while the n- and p-doped ones are homoepitaxial layers, should be able to show much lower values of the dark current [7].

2.3.1 Physical definition of metal-semiconductor contact

Behaviour of electrons in the semiconductor crystal is described by the Fermi-Dirac statistics. Probability of occupancy of energy level E is defined as [8]

$$f_{FD}(E) = \frac{1}{1+(E'-E'_F)}, \quad (1)$$

where E'_F is the Fermi level. E'_F is defined as an energy level whose probability of occupancy is equal to ½. Position of E'_F strongly depends on temperature and semiconductor doping. For intrinsic semiconductor, is E'_F located in vicinity of the midgap $E_g/2$, whereas for extrinsic semiconductors, E'_F depends on concentration of dopants. For n-type and p-type semiconductor, the position of E'_F is

$$\mu'_{F_n} = \frac{E_D}{2} - \frac{kT}{2}\ln\left(\frac{N_D}{N_C}\right), \quad (2)$$

$$\mu'_{F_p} = \frac{E_A}{2} - \frac{kT}{2}\ln\left(\frac{N_A}{N_V}\right), \quad (3)$$

where E_D is the energy level of donors, N_D is the donor concentration, T is temperature in K. For the case of p-type semiconductor, μ'_{F_p} is the difference between the Fermi energy E_F and the valence band edge E_v. E_A is the acceptor energy level, N_A is the concentration of acceptors and. For an n-type semiconductor, μ'_{F_n} is the difference between the Fermi energy E_F and the conductive band edge E_c. N_D is the concentration of donors. The effective densities of states in valence (N_V) and conduction (N_C) level are

$$N_C = 2\left(\frac{2\pi m_n kT}{h^2}\right)^{\frac{3}{2}}, \quad (4)$$

$$N_V = 2\left(\frac{2\pi m_{dh} kT}{h^2}\right)^{\frac{3}{2}}, \quad (5)$$

where m_{dh} defines the effective mass of holes and in the valence band and m_n is the mass of the electrons.

The metal-semiconductor contact is in every case heterogeneous: it is an interconnection of two materials with various band gap. Besides statistical modelling of electrons behaviour, some quantities are needed to quantify the metal-semiconductor interface. These quantities are:

1. **Work function of metal ϕ_m** is the energy necessary to relocate electron from fermi level of metal to the vacuum

$$\phi_m = E_{vac} - E_F(m). \quad (6)$$

2. **Work function of semiconductor ϕ_s.** – the same meaning as in the case of metal

$$\phi_S = E_{vac} - E_F(s). \quad (7)$$

3. **Electron affinity of semiconductor χ.** Is given as the energy obtained by moving an electron from the vacuum to the bottom of the conduction in the semiconductor.

$$\chi = E_{vac} - E_C. \quad (8)$$

Choosing relative energy of E_c to zero, the relationship between eq. 7 and eq. 8 is

$$\phi_S = \chi - E_F(s). \quad (9)$$

4. **Energy barrier from metal to semiconductor ΔE_{ms}** is the difference between Fermi level of metal and the highest value of E_c (n-type) or the lowest value of E_v (p-type).
5. **Energy barrier from semiconductor to metal ΔE_{sm}** is defined as the highest difference between the highest and the lowest value of E_c (n-type) or the highest value of E_v (p-type) in the semiconductor.

Depending on the values of ϕ_m, ϕ_s and conductivity type of semiconductor, two basic kinds contacts can be formed An *ohmic contact* is defined as a metal-semiconductor contact that has a negligible contact resistance relative to the bulk or series resistance of the semiconductor. A *Schottky (rectifying) contact* refers to a metal-semiconductor contact having a large barrier height ($\phi_b >> kT$) and a low doping concentration that is less than the density of states in the conduction band or valence band [9]. Following cases of M-S interface can appear**:**

n-type semiconductor:

1. **$\phi_m > \phi_s$ … rectifying contact is expected**
   -The barrier between M and S for electrons is

$$\Delta E_{ms} = \phi_m - \chi > 0. \quad (10)$$

   -The barrier between S and M for electrons is

$$\Delta E_{sm} = \phi_m - \phi_s > 0. \quad (11)$$

   -With increasing conductivity of S, ΔE_{ms} remains constant and ΔE_{sm} increases.
2. **$\phi_m < \phi_s$ … ohmic contact is expected**
   -The barrier between M and S for electrons is

$$\Delta E_{ms} = \phi_s - \chi > 0. \quad (12)$$

   -The barrier between S and M for holes is

$$\Delta E_{sm} = \phi_m - \phi_s < 0. \quad (13)$$

-With increasing conductivity of S, ΔE_{ms} decreases and ΔE_{sm} increases.

p-type semiconductor:

1. **$\phi_m > \phi_s$ … ohmic contact is expected**
   - The barrier between M and S for electrons is

$$\Delta E_{ms} = \phi_s - (\chi + E_g) < 0. \quad (14)$$

   - The barrier between S and M for holes is

$$\Delta E_{sm} = \phi_m - \phi_s < 0. \quad (15)$$

   - With increasing conductivity of S, ΔE_{ms} increases and ΔE_{sm} increases.
2. **$\phi_m < \phi_s$ … rectifying contact is expected**
   - The barrier between M and S for electrons is

$$\Delta E_{ms} = (\chi + E_g) - \phi_m > 0. \quad (16)$$

   - The barrier between S and M for holes is

$$\Delta E_{sm} = \phi_s - \phi_m > 0. \quad (17)$$

   - With increasing conductivity of S, ΔE_{ms} remains constant and ΔE_{sm} increases.

The effect of the work function of metals used for contacts deposition can be predictable. Table. 2 summarizes the limit conditions of metal work functions for existence of eider ohmic or rectifying contacts [8].

Table 2 Border values of metal work functions for ohmic / Schottky contacts formation with CdTe.

				Contact type	
E_g (eV) at 300K	**χ (eV)**	**Conductivity type**	**Limiting value of ϕ_m (eV)**	**Ohmic**	**Rectifiing**
1.47	4.5	n	4.5	max	min
		p	5.97	min	max

Figure 2.2 shows summary of work functions of metals. As can be seen from Table 2, to create an ohmic contact on a p-type CdTe, metal with work function higher than 5.97 eV is needed. Nevertheless, the metal with work function higher than 5.97 eV does not exist. Near ohmic contacts on p-type CdTe are created by electroless deposition of Pt or Au and behave as the tunnelling contacts. Most frequent metals used to create Schottky contacts on p-type CdTe are In, Al, Ni. Cu is often used as a back contact for CdTe/CdS solar cells. However, work function of CdTe differs by its surface conditions and it is difficult to obtain the work function by conventional analysis methods. Furthermore, Te-terminated or Cd-terminated side of (111) oriented crystal show differences in electrical behaviour of the contacts since Te-face is more conductive and has more n-type nature [4].

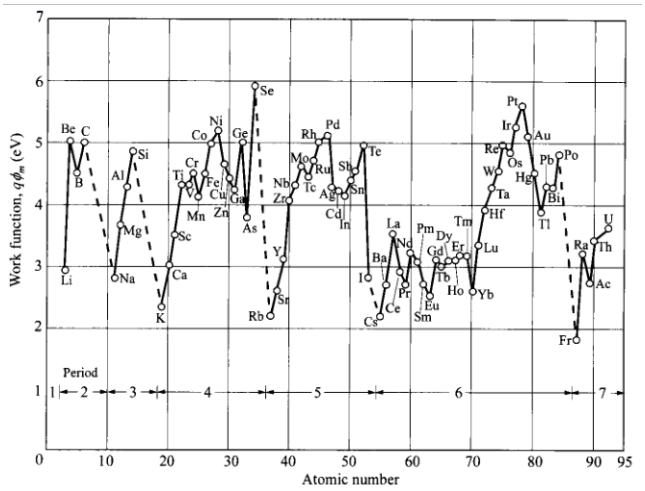

Figure 2.2: Work functions of metals (in vacuum). Image taken from [9].

For further explanation of M-S interface properties, the case of an n-type semiconductor and Au contact ($\phi_{Au} > \phi_{CdTe}$) will be used since all of the experiments in this thesis were done on such configuration.

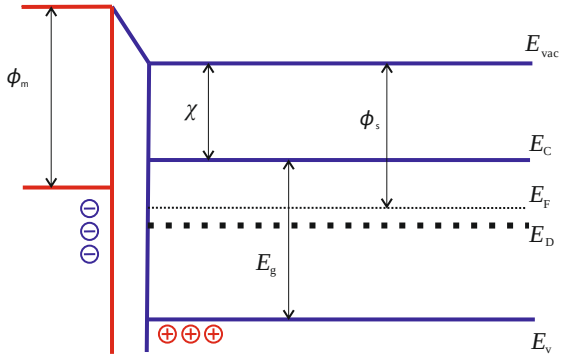

Figure 2.3: Energy band diagram of Au and an n-type CdTe connection.

In the moment of the M-S interface creation, the interface between metal and semiconductor becomes transparent for electrons. Different work functions of Au and CdTe cause relocation of electrons from the metal surface to the semiconductor. This electron current will continue until the Fermi levels in semiconductor and metal become the same. This process of stabilization results in creation of area with the positive charge on the semiconductor surface. Such situation is shown Fig. 2.3.

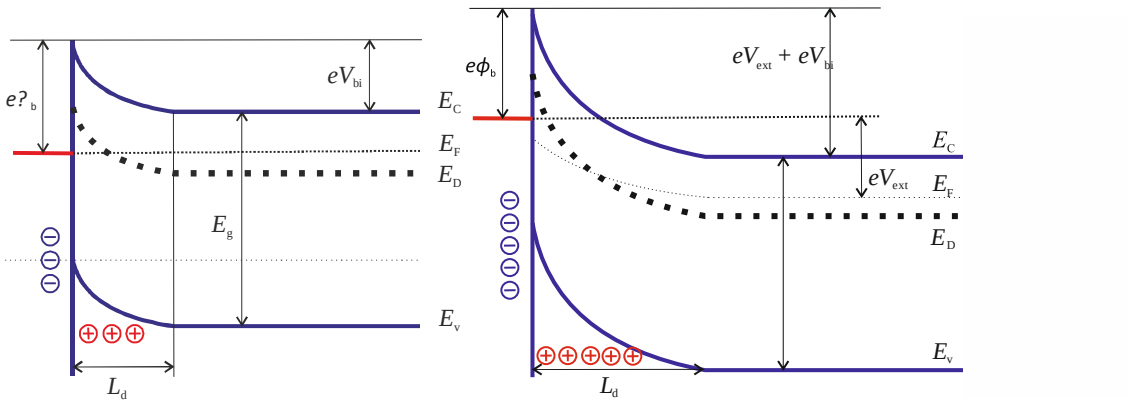

Figure 2.4: Energy band diagram of Au and an n-type CdTe contact at equilibrium at zero bias (left) and energy band diagram of Au and an n-type CdTe contact with applied external potential in reverse polarity (right).

Monatomic surface layer does not contain enough carriers to obtain equilibrium of Fermi levels of metal and semiconductor. So, the recombination process continues deeper into the bulk, resulting in creation of region with the thickness L_d, which is depleted from charge carriers. Due to high concentration of carriers in metal, band bending in it is negligible. In semiconductor, all energy levels bend inside the depletition region. As shown in Fig 2.4(left), band bending defines the height of the potential barrier. As was shown above, this height is defined by

$$\Delta E_{ms} = e\phi_b = e(\phi_m - \chi) > 0 \tag{18}$$

and the diffusion (built-in) potential, as a difference between ϕ_m and ϕ_s related to μ_F is

$$eV_{bi} = e\phi_m - e\phi_s = e\phi_m - e(\chi + \mu_F), \tag{19}$$

Where the relationship between the built-in potential and depletition length is

$$eV_{bi} = \frac{2\pi e^2 N_D L_d^{\ 2}}{\varepsilon_0 \varepsilon_r}. \tag{20}$$

If an external potential is with the same polarity is applied, the diffusion potential will be increased by the value of external potential.

$$V_{bir} = V_{bi} + V_{ext}, \tag{21}$$

$$V_{bif} = V_{bi} - V_{ext}. \tag{22}$$

This means the interface is reverse biased. As expected, the opposite polarity from reverse one, forward polarity, acts against positive space charge in M-S interface and therefore reduces V_{bi} and L_d. Once $V_{ext} > V_{bi}$,all the energy levels in increase as the value eV_{bi}. The effect of external potential and its polarity on L_d can be expressed as

$$L_{dr} = \sqrt{\frac{2\varepsilon_0 \varepsilon}{eN_D}(V_{bi} + eV_{ext})}, \tag{23}$$

$$L_{df} = \sqrt{\frac{2\varepsilon_0 \varepsilon}{eN_D}(V_{bi} - eV_{ext})}. \tag{24}$$

The effect of reverse external potential is shown in Fig. 2.4 (right). Theory above describes the ideal case of the contacts formation. The real M-S interface are strongly influenced by surface states and residual impurities. Presence of inhomogeneous distribution of surface states in energy spectrum of band diagram or presence of the interfacial layer can be modelled as a Metal-Insulator-Semiconductor (M-I-S) structure. This constellation is sketched in Fig. 2.5. Proposed band diagram describes situation with native oxide $CdTeO_3$ in M-S interface. The input parameters for design of the band diagram are: ϕ_{Au} = 5.1 eV, χ of CdTe is 4.3 eV, χ of $CdTeO_3$ is 1.3 eV (determined by Ultraviolet Photoemission Spectroscopy) E_g of CdTe is 1.5 eV and 5.0 eV for $CdTeO_3$. Fermi level is situated 0.1 eV below the conduction band of CdTe [10].

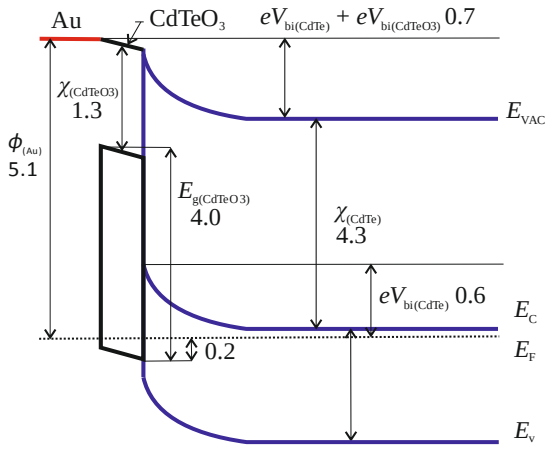

Figure 2.5: Energy band diagram for an Au MIS junction on n-CdTe with native oxide as the insulator. Units are in electronvolts.

Beside the change of the potential barrier height, different nature of charge transport appears. The oxidation to $CdTeO_3$ at M-S interface reduces number of free electrons in high resistivity oxide situated between Au and CdTe. Another change occurs as a result of well-known fact that oxidation redistributes impurities in M-S interface. Two conduction mechanisms appear for forward low biases: i) weak excitation of holes in Au that move through the oxide and recombine with the interface states or ii) strong excitation of holes that move directly to the n-CdTe valence band. Mechanism i) is considered to be more likely [10]. Under high forward biases, tunneling is dominant transport mechanism. Thickness of the oxide layer is a current limiting factor.

2.4 Surface

After mechanical cutting of the crystal from ingot, mechanically damaged layer is removed by grinding. In most cases, Al_3O_3 or B_4C grits are used since diamond-based grids are too hard and leave deep mechanical scratches on the surface. This procedure is followed by fine free abrasive polishing. Al_2O_2 powders are most frequently used in a few steps with decreasing diameter of grain of the powder, typically from 10 μm to 0.3 μm. Intermediate procedure between mechanical and chemical processing is chemo-

mechanical polishing. It is performed by using a polishing member made from soft natural or synthetic tissues, on which the etchant solution or suspension containing the etchant and abrasive particles is supplied [11].

After mechanical processing of the surface, the mechanically damaged and oxidised layer is still present. This layer is removed chemically. The most widely used solution is the solution of elemental bromine in organic and inorganic solvents. Such mixtures polishing properties and their etching rate are limited by the diffusion stages of heterogeneous properties and their toxicity. Such treated substrate is, however, Te rich [12] and contaminated by bromine. CdTe treatment using Br solution in CH_3OH leads to formation of a layer with an increased concentration of cadmium vacancies [13]. Another often used etchant is nitric acid and its mixtures. This acid acts as an oxidant and forms surface layer of 50 nm thickness [14]. This layer contains a very high density of fixed charge and causes performance degradation. The oxide can be removed with NH_4OH [15]. Still, the surface layer has two orders higher resistivity than the crystal bulk [16]. Chromium (VI) compounds are strong oxidants used for the surface treatment of CdTe crystals. A low quantity of tellurium is presented after etching. Using solutions with high content of K_2CrO_7 result in absence of tellurium dioxide. The depth of Cd depleted layer can reach up to 800 nm. [17]. unfortunately, a diffusion of Cr into ingot worsening bulk properties was reported.

Beside chemical methods, "dry" methods can be applied. Plasma etching or ion bombardment are involved in these processes. Ar, H_2, O_2, CH_4 and their mixtures are used for plasma processing. The gas flow, ratio between gasses, energy and frequency of RF generator, processing time and temperature are input parameters of dry etching. As expected, the surface with the O_2 plasma treatment is almost completely oxidized. Ar/H_2 plasma treatment seems to be the most promising for CdTe. Exposure to low flows (~1.5 sccm) succeeded in removal of carbon based organic residuals, removed excess Te from the Br-MeOH etched surface [18]. Unfortunately, this procedure caused serious surface roughening for CdZnTe due to ZnTe built-up on the surface. Addition of CH_4 to Ar/H_2 mixture increased etch rate of Zn and the surface roughness and Zn segregation decreased. The limiting factor for CH_4 is increased segregation of hydro carbonates on the surface. Ar ion beam bombardment seems to be very promising. 1.0 keV was established as an optimal sputtering energy, sufficient to remove contaminants and debris without causing irreversible surface roughening, while causing minimal compositional changes (with respect to Cd and Te) [19]. On the other hand, Te enrichment at the outermost surface but Te depletion in the subsurface was found [20]. This might be the result of thermally activated segregation since the local temperature at sputtered area significantly increases.

3 Noise in the semiconductor optical devices

Noise properties, as a result of unwanted electric signal fluctuations in time, are very important parameter that seriously limits manufacturing X-ray semiconductor detector with good spectral resolution and fast response. Determination of the noise sources and its neutralization is important for improved performance of the detector.

Not only manufacturing quality of the device has impact on the noise properties. At higher ambient temperatures, the impedance of such devices becomes significantly lower than required. Thermally generated carriers and diffusion currents increase additive noise of the device. Cooling of the detector bring complications into final device design, increase power consumption and is bulky. Reduction of the dark currents by Schottky contacts architecture decreases the current, but, on the other hand, Schottky contacts exhibit higher 1/*f* noise due to low concentration of charge carrier below the reverse biased contact [21]. 1/*f* noise is dominant for imaging devices that operate at low frame rate [27] or for X-ray detectors with long collection time, understanding the mechanism of 1/*f* noise is crucial.

Beside the 1/*f* noise, there are other "basic" forms of noise, such as Johnson-Nyquist noise, Generation-Recombination noise, and shot noise. Idealized subscription of each noise type on the detector system is shown in Fig. 3.1.

Fluctuations related to the thermal relaxations have typical Lorenzian spectrum, non-stationary noise originated from relaxation of material defects have spectral component with slope of 2. Combination with different noise types can give a power law with an exponent less than -2 over a limited frequency band [22]. Total noise of the X-ray detection system can be expressed as:

$$S_n^2 = S_{1/f}^2 + S_{1/f^2}^2 + S_{GR}^2 + S_{shot}^2 + S_{ph}^2 + S_{amp}^2, \tag{25}$$

where $S_{1/f}^2$ is the 1/*f* noise, S_{amp}^2 is the amplifier noise, S_{1/f^2}^2 is the material defect relaxation noise, S_{GR}^2 is the Generation –Recombination noise, S_{shot}^2 is the shot noise and S_{ph}^2 is the photon noise.

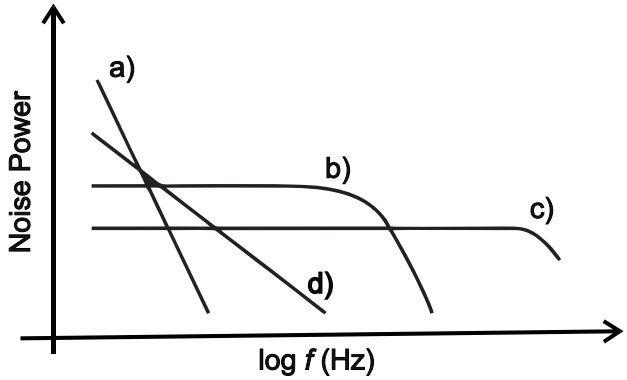

Figure 3.1: Typical subscription of noises sources in photodetector. a) Noise due to the relaxation of material defects (1/*f* $^{-2}$), b) Generation recombination noise or thermal relaxation noise, c) Shot noise or photon noise, d) 1/*f* noise.

Contributions of each noise component S_x is expressed by means of its the power spectral density. This parameter is described as follows: Noise has stochastic nature with unpredictable values. Nevertheless, in some practical systems, the average noise power can be predicted by statistical models. The average power of the signal in time $x(t)$ can be described as

$$\lim_{T\to\infty}\frac{1}{T}\int_{-T/1}^{T/1}x^2(t)dt \quad . \tag{26}$$

The meaning of the noise power is more informative when the distribution of the noise power is expressed as its distribution in frequency. The power spectral density $S_x(f)$ of the noise signal is defined as the signal average power in 1 Hz bandwidth at frequency f. When a signal with known power spectral density is applied to a Linear Time Invariant (LTI) system described by its transfer function $H(s)$, the power spectral density on output of the LTI system is

$$S_y(f)=S_x(f)\left|H(f)\right|^2 \quad . \tag{27}$$

The autocorrelation function of the signal and its power spectral density and its power spectral density are Fourier transform pairs

$$S_x(\omega)\Leftrightarrow\overline{X(t)X(t+\tau)} \quad . \tag{28}$$

3.1 Thermal noise

Thermal (Johnson-Nyquist, White) noise is mainly caused by random, Brownian motion of the charge carriers and their collusions with the material atoms. This noise is present without applied voltage. Under zero voltage condition, under dark and stable temperature, the power spectral density of thermal noise is expressed for short-circuit current as:

$$S_I=4kT/R \quad , \tag{29}$$

where k is the Boltzmann constant; S_I are noise spectral density of current. Sometimes, relation is multiplied by Δf as the bandwidth interval. This quantity is independent on material, has constant, "white" spectrum. The only quantities that influence thermal noise are temperature and electrical resistance R, respectively. The equivalent expression of Eq. 29 for the open circuit voltage noise power spectral density S_U is

$$S_U=4kTR \quad . \tag{30}$$

3.2 Shot noise

Shot (Schottky) noise has its origin in discrete nature of electrons and holes, resulting in current shows burs-like character in time when travelling through the p-n junction or meta-semiconductor interface. In general, a condition for the shit noise is

existence of a potential barrier, which has to be passed through by the charge carriers. The spectral density if the shot noise is given by the relation

$$S_I = 2qI, \tag{31}$$

where q is the elemental charge and I is the current flowing through the specimen. For the case of Metal-Semiconductor interfaces (Schottky diodes), two types of carriers have to be taken into account.

- Carriers that reach the potential barrier on their flow from metal to semiconductor. These carriers produce the saturated current I_0, which is independent on the bias voltage.
- Carriers flowing from semiconductor to metal, which reach potential barrier of height e(ϕ_B-U), where ϕ_B is the contact potential and U is the voltage drop developed between the semiconductor and metal. So, the total shot noise current spectral density is given by currents of charge carriers of both "polarities" and its value is given as

$$S_I = 2q(I + 2I_0). \tag{32}$$

The ideal nature of shot noise is unreachable, because this model takes into account ballistic transport mode, that does not take account any interaction between charge carriers (repulsion forces between carriers with the same sign), with the lattice atoms /impurities during the drift of the carrier. The interactions enhance randomness resulting in smoothening of the carrier's bursts. Shot noise reduction can be reached by low density of the carrier in semiconductor, combined with high applied field. Similar effect on shot noise has space charge build-up as a cause of Au/CdZnTe/Au detector structure, as I show in section 4.2.3.

From the nature of function of CdTe as an electro optical device, it is necessary to mention the photon noise, which is closely related to the shot noise. For the ideal diode, the current through the junction is only due to diffusion and the current I_{ph} generated by the photon flux Φ_{ph}, the total junction current is given as

$$I = I_0\left[\exp\left(\frac{eU}{kT}\right) - 1\right] - I_{ph}, \tag{33}$$

$$I_{ph} = \eta e \Phi_{ph} A_{coll}, \tag{34}$$

where A_{coll} is the irradiated area (optical collection area) and η is the quantum efficiency. Because the diffusion current and the photon current can vary independly on each other, they both exhibit shot noise. This station can be described by relation [8]

$$S^2 = 2eI_0\left[\exp\left(\frac{eU}{kT}\right) + 1\right] + I_{ph}, \tag{35}$$

which is for the zero-bias resistance R_0 for diode with diffusion limited current is

$$R_0 = \frac{eI_0}{kT}. \tag{36}$$

The band limited current noise at zero bias is

$$S^2_{I(U=0)} = \left(\frac{4kT}{R_0} 2\eta e^2 \Phi_{ph} A_{coll} \right) \Delta f, \tag{37}$$

that is thermal noise (eq. 29) with an additional term for the photon current.

For high performance of the detector, it is crucial to meet the criterion that the detector is background limited, i.e. the thermal generation is much lower than the photon generation even in the lowest flux rates. The condition for background-limited performance is therefore often written as [8]

$$R_0 = \frac{2kT}{2\eta e^2 \Phi_{ph} A_{coll}}. \tag{38}$$

For large reverse bias voltages, the shot noise is reduced by half and the total noise for diffusion limited junctions is

$$S^2_{I(U<0)} = \left(\frac{2kT}{R_0} + 2\eta e^2 \Phi_{ph} A_{coll} \right) \Delta f. \tag{39}$$

Typically, HgCdTe photodiodes are operated in very low reverse biases, from -5mV to -50mV. If higher biases are applied, eq. 39 applies and the other noise sources become dominant. For the case of CdTe, around the equilibrium condition (0 ÷ 0.5V) the measured noise density of then noise with white spectrum agrees with the calculated Johnson produced by equivalent resistor, exactly with the same resistance as the value effectively measured with zero Volt across the detector. [81]. Higher biases exhibit shit noise with power spectral density proportional to $2qI$.

3.3 Generation-Recombination noise

Generation – Recombination noise (GR) is the result of presence of electrically active impurities or defects. For wide gap semiconductors, the GR centres are Shockley-Read-Hall type. Defects located closest to the midgap have the highest contribution to the GR noise [23]. Generated electron-hole pairs are pushed out in the depletion region by electric field. This current is known as the generation-recombination current. The basis of GR fluctuation current is based on fluctuation around equilibrium (state, when electron densities e and hole densities p are equal, i.e. $np = n_i^2$, where n_i is the intrinsic carrier concentration) of generated and recombined charge carriers between two conditions: When there are some excess carriers, $np > n_i^2$, the rate of recombination is higher than the rate of generation. Similarly, in the case of lack of carriers, $np < n_i^2$, the generation rate becomes higher than the recombination rate [24].

Acknowledged models proposed by Sah at al [25] and Choo [23] yield the same results at the zero bias conditions, but Choos's model that extends Sah's model takes into

account non-symmetry of the junctions. The current density of GR current is calculated as an integration of steady-state recombination rate

$$J_{GR} = e\int_0^w U(z)dz \quad , \tag{40}$$

where $U(z)$ is defined as the difference between recombination rate and generation rate [23] that is expressed as

$$U(z) = \frac{np}{\tau_{p0}(n+n_1)+\tau_{n0}(p+p_1)} - \frac{n_i^2}{\tau_{p0}(n+n_1)+\tau_{n0}(p+p_1)} \tag{41}$$

and

$$\begin{aligned} n_1 &= N_C \exp\left(\frac{E_t - E_g}{kT}\right) \\ p_1 &= N_V \exp\left(\frac{-E_t}{kT}\right), \end{aligned} \tag{42}$$

where N_c and N_v are effective densities of states in conduction and valence band and E_t means the energy of the trap. Considering non-degenerated semiconductor and linear potential distribution in the depletion region, the GR current is expressed as

$$J_{GR} = \frac{2qn_i W \sinh(qU/2kT)\, f(b)}{\theta\sqrt{\tau_{p0}\tau_{n0}}} \quad , \tag{43}$$

where

$$f(b) = \begin{cases} \left(1-b^2\right)^{-1/2} \arctan\left[\alpha(1-b^2)^{1/2}/\beta\right] & b^2 < 1 \\ \alpha/\beta & b^2 = 1 \\ \left(b^2-1\right)^{-1/2} \arctan\left[\alpha(b^2-1)^{1/2}/\beta\right] & b^2 > 1 \end{cases} \quad , \tag{44}$$

$$b = \exp\left(\frac{-qU}{2kT}\right)\cosh\left(\frac{E-E_i}{kT} + \frac{1}{2}\ln\frac{\tau_h}{\tau_e}\right) \quad , \tag{45}$$

$$\alpha = \sinh(\theta/2) \quad , \tag{46}$$

$$\theta = q\left(U_{bi} - U\right)/kT \quad , \tag{47}$$

$$\beta = \left(\tau_n p/\tau_p n\right)^{1/2} + \left(\tau_p n/\tau_n p\right)^{1/2} + 2b\cosh\left(\theta/2\right) \quad . \tag{48}$$

The electron lifetime τ_n and the hole lifetime τ_p depend on the concentration of recombination centers and differ with the quality of the semiconductor material. This fact can be expressed as

$$\tau_n = \frac{1}{C_n N_t}, \tag{49}$$

$$\tau_p = \frac{1}{C_p N_t}, \tag{50}$$

where C_n and C_p are capture coefficients for the electrons and for the holes. N_t stands for the concentration of recombination traps in unit volume. From above can be seen that GR

centres can be both acceptors and donors. For simplification, let's take just a single carrier τ as a characteristic relaxation time of a single GR process. Spectrum of such GR signal is given by formula [26]

$$S_i = \frac{S_N(\omega)}{N_0^2} = \frac{\overline{\delta N^2}}{N_0^2} \frac{4\tau}{1+(\omega\tau)^2}, \tag{51}$$

where ω is the angular frequency, N_0 is the average number of free carriers and δ is the variance of carrier number fluctuations. The spectrum of the fluctuations in eq. 51 is Lorentzian type with two parameters: the relative variance of number fluctuations and the lifetime of charge carriers. The above spectrum generally refers to thermal equilibrium conditions [26]. Beside the space charge layer of every junction, the GR noise has important role for intrinsic or weakly doped semiconductors, as CdTe for the X-ray detection is.

For irradiated photosensitive detectors, interesting relation between the shot and the GR currents appear. As previously mentioned, the GR current is result of composition of recombination current I_r and generation current I_g within the space charge region with thickness W:

$$I_{GR} = I_R - I_G = eA\int_{-W}^{0} R(z)dz - eA\int_{-W}^{0} G(z)dz. \tag{52}$$

In the case when the carriers are generated by illumination with radiation with energy higher than the band gap of the semiconductor, an electron-hole pair is generated: The electron is removed from the valence band and lands at the conduction band. The photon annihilates after its energy is given to electron. Generation rate for electrons or holes of such process is

$$G_{p,ph}(z)dz = G_{n,ph}(z)dz = \alpha \frac{P_{opt}}{E_{ph}A_{coll}}, \tag{53}$$

where P_{opt} is the optical power, E_{ph} is the energy of photon and α is the material dependent optical absorption coefficient.

For high reverse voltages where $eU >> kT$, subscription of the photo generation enhances further lowers the importance of recombination mechanism in the GR current. Thus, the noise current is then given as:

$$I_{GR}^2 = 2eI_g, \tag{54}$$

which is the shot noise of the generation current [26].

3.4 1/f noise

1/f noise is typically present only if the current flows though the device. This source of additional noise distinguishes by its typical shape of the power spectral density spectrum that follows the law f^{-m}, where m is typically around unity. The 1/f noise is also commonly called pink, flicker, contact or excess noise. It has been observed not only in

electrical systems like resistors, semiconductors, liquid metals, electrolytes, but also in biological systems like human heartbeat, neuro membranes etc. The same characteristics like 1/*f* noise have, were found not only for electric signals. For example, in financial systems, relict radiation from the space, music, metrological data etc. One can see that occurrence of 1/*f* fluctuations is really vast. From this, the general origin of such fluctuation is not well understood so far.

For electronic systems, the most accepted explanation of 1/*f* noise origin is that 1/*f* noise is closely linked with crystallographic defects, deep levels, surface states and the quality of the interfaces. The 1/*f* noise can be modelled by various mathematical, physical or experimental models based on empirical relationships for the evaluation of the noise spectral density. Among numerous models, the basic ones are:

1. McWorthel model – based on the number of carrier's fluctuations.
2. Hooge model – based on fluctuation of mobility of the carriers.

3.4.1 Hooge's model

Hooge's model, proposed in late 1960s assumes that the source of 1/*f* noise is a free carrier scattering. When a constant voltage is applied to a semiconductor resistor of resistance *R*, a fluctuating current *I*(*t*) is developed. This can only come about because the resistance *R*(*t*) of the device fluctuates [22].

$$\frac{\Delta I}{I} = -\frac{\Delta R}{R} \Rightarrow \frac{S_I(f)}{I^2} = \frac{S_R(f)}{R^2} \quad . \tag{55}$$

If *R* and its fluctuation ΔR are independent on current, the spectrum $S_I(f)/I^2$ is also current independent. This result is valid for the GR spectrum with the Lorenzian shape $S_I(f)/I^2 = \text{const}/(1+\omega^2\tau^2)$ caused by carrier trapping. The resulting 1/*f* spectrum is a superposition of Lorenzians. Clarke and Voss [22] proposed relation also dependent on resistance fluctuations that was irrespective of 1/*f* noise. $S_I(f)/I^2$ can be written as

$$\frac{S_I(f)}{I^2} = \frac{\text{const}}{f} \quad . \tag{56}$$

Hooge solved the question what is the content of the constant in eq. 56. He proposed that the missing parameter is the number of carries *N* and weakly temperature dependent material constant α. This empirical formula has form

$$\frac{S_I(f)}{I^2} = \frac{S_R(f)}{R^2} = \frac{\alpha}{fN} \quad . \tag{57}$$

Apparently, the eq. 57 does not prove or predict anything, just gives operational definition of the parameter α. This equation is always valid and fits the 1/*f* spectra and is only useful to obtain the Hooge parameter α [22]. Hooge made experiments with large series of semiconductor bars with defined length *L*, cross-sectional area *A* and resistance given by $R = L^2/(e\mu N)$ and extracted the α parameter via eq. 57. He found very low variation of α, which was around 10^{-3} for various semiconductors (GaAs,CdHgTe, Si) with various

carrier concentrations. The near constancy of α, suggests that this l/*f* noise is due to a fundamental mechanism of unknown origin [22].

On the other hand, numerous studies contradicted validity of the Hooge formula. Severe dependence of α on temperature was reported in [28], the strong dependence of the 1/*f* noise on oxidation state of the surface was published in [29] etc. The most accurate results were obtained on material with metalized contacts, so it is quite possible that the Hooge's formula describes rather contact noise than the noise originated in the semiconductor bulk.

3.4.2 McWhortel's Model

This model, commonly known as the Charge trapping model, assumes that the source of 1/*f* noise is a fluctuation of the carrier number in the system. The resulting spectrum is given as superposition of *N* generation-recombination Lorezian fractional spectra with vast range of relaxation times within the limits τ_2 and τ_1. This model is considered to be valid in cases if following conditions are fulfilled [22]:

- In the silicon oxide near the silicon surface there are uniformly distributed trap centers.
- The probability of the carrier penetration to trap centers is decreasing exponentially with the distance from the surface.
- Time constants of trap centers increases with the distance from the surface.
- Trapping mechanisms by separate centers are independent.

Then, the noise spectral density according to McWhorter is

$$S_N = \overline{4\Delta N^2}\int_{\tau_1}^{\tau_2} g(\tau_N)\frac{\tau_N}{1+\omega\tau_N{}^2}d\tau_N = (\overline{\Delta N})^2\frac{1}{f} \qquad (58)$$

The power spectral density has white character up to the frequency $f_2 = 1/2\pi\tau_2$. After this limit, the power spectral density is proportional to 1/*f* in frequencies up to $f_1 = 1/2\pi\tau_1$. At higher frequencies than f_1, the proportion becomes $1/f^{-2}$. This situation and effect of τ_1 and τ_1 is illustrated in Fig. 3.2. If certain trap plays dominating rule in the fluctuation process (e.g. conductive surface oxidised to specific oxide), hill-like shape can appear in the "straight" 1/*f* spectrum as a result of its superimposition of it.

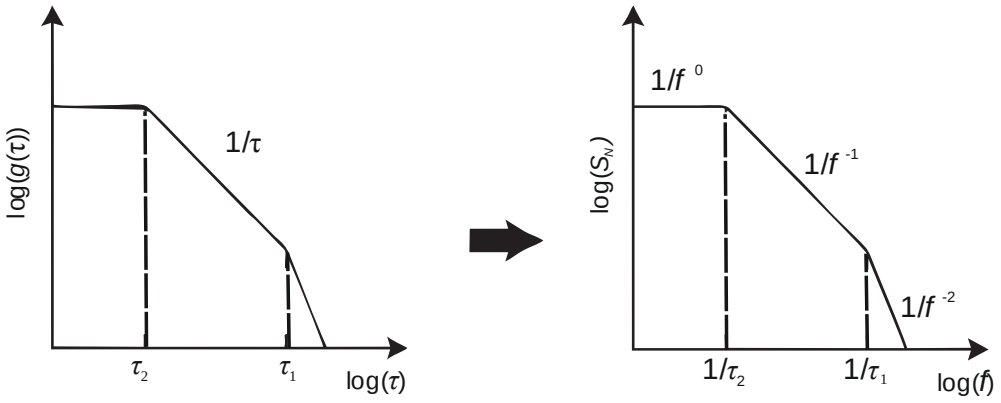

Figure 3.2: Distribution of time constants for traps for the McWhortel model.

McWhortel's model based on the carriers' number fluctuation noise gives a l/*f* spectrum caused by a distribution of time constants specific for each defect. This case is possible when there are distributed traps in the surface oxide (MOSFETs, BJTs); it results in a current dependence that is different from what is expected from Hooge's theory [22].

3.4.3 Models validity: The problem of Number vs. Mobility fluctuations

Both number of carriers and their mobility in the semiconductor system affect conductivity. Conductivity of semiconductor is given by

$$\sigma = q\mu n, \tag{59}$$

Each case of fluctuation ($\Delta\mu$ or Δn) is expressed as

$$\Delta\sigma = \frac{d\sigma}{dn}\Delta n = q\mu\Delta n, \tag{60}$$

$$\Delta\sigma = \frac{d\sigma}{d\mu}\Delta n = q\Delta\mu n, \tag{61}$$

so the dependence of noise on the total number of carriers assumes that number fluctuations are the cause of the conductivity fluctuations. The mobile carriers can be trapped in electrically active defects. Because of charge neutrality in semiconductors, this exchange must happen between discrete internal states, so if fluctuations occur, trapping must happen. The resistance fluctuation from the Hooge's theory, integrated over 10 decades is [22]

$$\frac{S_R}{R_0^2} = \frac{10\alpha_H}{N}\ln 10 \cong \frac{1}{20N}. \tag{62}$$

Situation described by Eq.62 can occur only if the number of traps equals to the number of carriers in the system. In metals, the carrier density is roughly the same as the number of atoms per unit volume, we can exclude number of caries fluctuation as a cause of 1/*f* noise in thin metal films, since the number of traps is not high enough.

In the case of semiconductors, the carrier density is of the orders lower than the number of atoms (for intrinsic CdTe $n_i \sim 10^6$ cm^{-3} [30] vs. atomic density ~ 10^{22}cm^{-3}), the

case of carrier number fluctuations is possible. Shallow donors and acceptors cannot cause 1/*f* noise since they are located close to the conduction or valence band edges. Traps around the midgap can cause 1/*f* fluctuations, which should to be very temperature sensitive, but it is not observed. 1/*f* noise studies [31, 32] conclude that the conductivity fluctuation in time is a result of fluctuation of mobility and fluctuation of carriers' number can be ruled out. The utilization of McWhortel model is limited to application on heavily oxidized surfaces or Metal-Oxide-Semiconductor structures.

4 Experimental part – electrical characterization

My field of interest was investigation of detector grade crystals, crystals with lower resistivity and enhanced polarization, detectors with asymmetry of electrical characteristics and thermally degenerated crystals were subject of my work in terms of analysis of their current stability, additional noise, electric field distribution and structural properties. Short motivation why I conducted each experiment I used and brief description of advanced methods employed in experiments is given. Work was done systematically on detectors from two ingots. List of detectors and the basic reason why was each one used is in Table 3. Further information about the samples is given in introduction of each experiment.

Table 3: List of samples used in experiments

Label	Material	Section	Reason of use
E46-GR	Au/CdZnTe/Au	4.1	Guard-Ring structure
E46D3A	Au/CdZnTe/Au	4.2	Enhanced polarization, optical quality of edges
B39D1G	Au/CdTe(In)/Au	4.3	Contacts asymmetry
B39D1H	Au/CdTe(In)/Au	5	Thermal degeneration
B39N2G	Au/CdTe(In)/Au	5	Thermal degeneration- control sample
E46D3F	CdZnTe	6	Not metalized

4.1 Localization of the noise sources in CdZnTe detector system

As explained in Introduction, three basic parts of the detector: Contacts, Crystal and the Surface are the fundamental sources of the detector additive noise and their manufacturing quality influences the whole system. In this part of my work, the noise spectral density analysis is used to find the bottleneck of the detector system by means of evaluation of each detector part contribution to the total noise of the detector system. Contact quality is estimated from its rectifying properties, which indicate the amount of impurities and the quality of contact metal deposition, which influences Schottky contact electrical properties.

For all electrical quantities and noise measurements, following configuration was used: Samples with a load resistor are placed into the cryostat. The cryostat allows controlling operating temperature in the range from 77 K to 400 K by a heating spiral and liquid nitrogen dosing. As a temperature sensor inside cryostat, diode fed by constant current 10 μA is used. The thermal gradient of U_d is -2.421 mV/K. U_d is used as an input parameter for temperature control, which is an implementation of PID control algorithm. The cryostat also acts as an undesired electrical field screening. The programmable digital-analog converter Agilent E34401A is used for the *I-V* characteristics measurements. Measuring instruments are interconnected by the data acquisition unit Agilent 34970A with the plug-in module Agilent 34902A, which is used for data conversion and is connected with PC via GPIB / IEEE488 interface. Noise measurements in the dark were carried out at the room temperature. The sample was fed from the dry cell batteries, which show negligible noise, compared to the measuring electronics. The applied voltage was 12, 24, 37 and 50 V. The sample fluctuating voltage was amplified by the ultra-low-noise voltage amplifier FEMTO DLPVA-100-F-S on the load resistor. Output voltage of the amplifier is sampled by an external data acquisition card National Instruments USB-6216. The noise voltage was transformed into the corresponding noise spectral density using the Fast Fourier Transformation algorithm. Our set-up allows us to measure the sample current and noise voltage simultaneously without any effect on the noise. The measured values were recorded and analyzed in a personal computer.

The investigated sample was made from an n-type CdZnTe crystal, grown by the Vertical Gradient Freeze method at the Institute of Physics, Charles University, Prague. The dimensions of the sample are 6 × 6 × 1.5 mm^3. The sample specific resistivity is 10^7 Ωcm. Sides of the detector were mechanically polished by the 5 μm grit. Surface chemical treatment was carried out by etching in 1 % Br-methanol solution. Geometrically identical gold electrodes and the guard ring electrode surrounding cathode were chemically deposited on the opposite surfaces of the sample from an aqueous solution of $AuCl_3$.

4.1.1 *I-V* characteristics analysis: Separation of bulk and surface leakage current

Figure 4.1 presents the *I-V* characteristics of the examined detector. The picture on the left shows the *I-V* characteristics of the sample with disconnected guard ring electrode, whereas the picture on the right shows *I-V* characteristics with connected guard ring. Marking “contact A” and “contact B” indicates which of two contacts was biased in reverse mode, thus acting as rectifying.

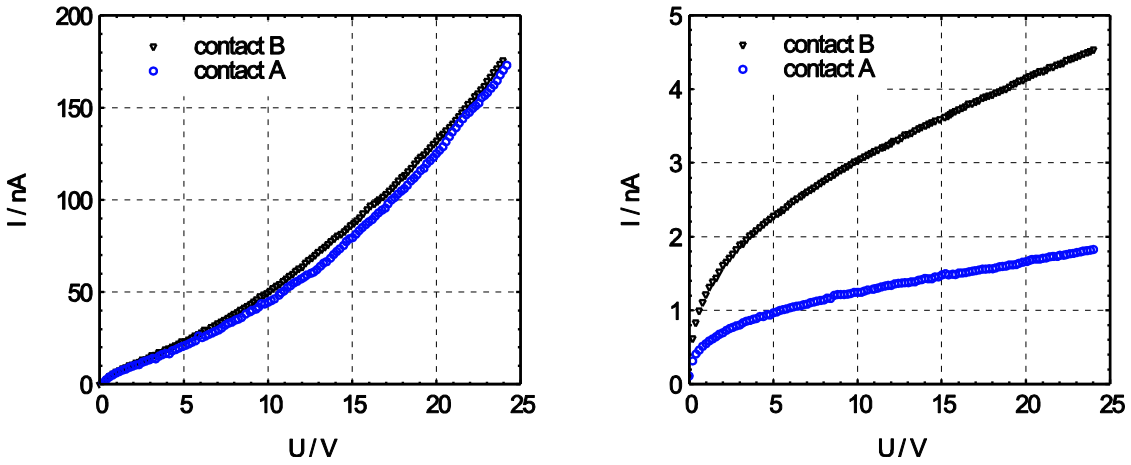

Figure 4.1: Current – voltage characteristics of the detector without connected guard ring (left) and with connected guard ring (right).

In the case of unutilized guard ring electrode (fig. 4.1 left), I observed very symmetric behavior of both contacts, showing nearly identical rectifying properties. The characteristics bend upwards from the applied bias voltage U = 5 V due to the hole injection. If injection is not present, the increase of the current is due to thermally generated carriers linear with increasing applied voltage. In our case, the current increases with the second power of applied bias voltage, i.e. $I \sim U^2$. The steeper rise of the detector leakage current indicates a higher concentration of traps located in the detector system [33]. The *I-V* characteristics with connected guard ring electrode, shown in fig. 4.1 right, exhibit nearly two orders lower leakage currents. Apparently, the highest contribution to the "unprotected" detector leakage current has the conductive surface layer. Starting from U = 7 V (contact A) and U = 10 V (contact B), the characteristics exhibit linear behavior, typical for non-injecting contacts. Compared with *I-V* characteristics of the detector with unutilized guard ring electrode, The *I-V* characteristics asymmetry is clearly visible. This asymmetry uncovers the difference of rectifying efficiency of each contact. At U = 25 V, contact A produces leakage current 1.95 nA, whilst the contact B has leakage current of 4.7 nA. This asymmetry points to the presence of higher concentration of imperfections at the area of the contact B.

4.1.2 Noise power spectral density Analysis: separation of noise sources

Figure 4.2 shows the noise spectra of detector with disconnected guard ring electrode. Solid black line in fig. 4.2 (right) indicates the limit of the measurement apparatus. The key limitation is the load resistor thermal noise $S_U = 4kTR = 1.58 \times 10^{-15}$ V^2s, where k is the Boltzmann constant, T is operating temperature and R is the resistance of the load resistor 100 kΩ.

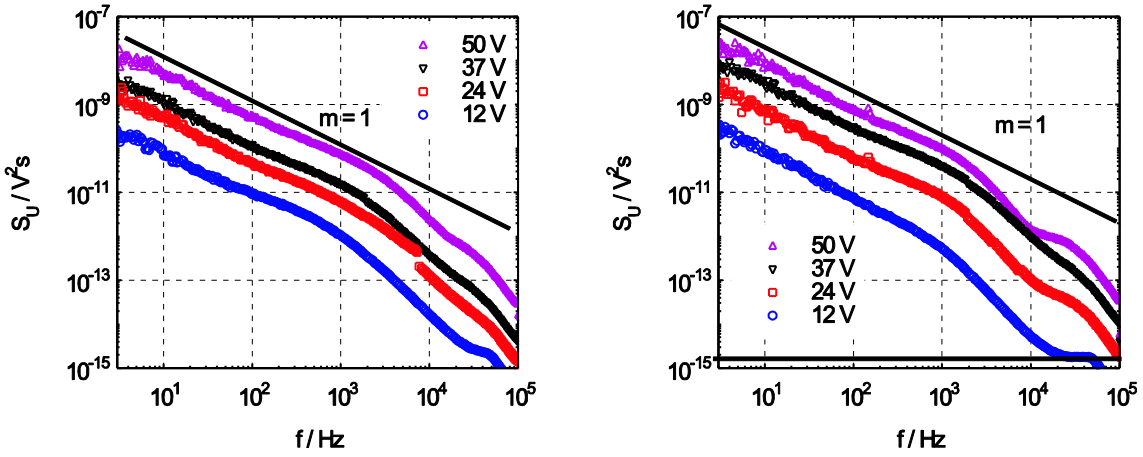

Figure 4.2: The low frequency noise spectra of the detector with disconnected guard ring electrode. Reverse biased contact A (left), reverse biased contact B (right).

The noise measurements of the studied CdZnTe detector show that the dominant noise is of the $1/f^{\,m}$ type. The $1/f^{\,m}$ noise, with parameter m close to 1, is present at frequencies below 1000 Hz. At higher frequencies, the parameter m increases to the value m = 1.5 due to an enhanced effect of generation –recombination noise. In the case of the reverse biased contact A and also for the reverse biased contact B, the shape of the spectra is similar. The reverse biased contact B shows slightly higher magnitude of the noise spectra that is in agreement with higher leakage current measured for the reverse biased contact B, as plotted in fig. 4.1 (left). Nevertheless, the order of magnitude of the spectra is the has the same order (e.g.: 10^{-8} V^{2}s for U = 50 V and 10^{-10} V^{2}s for U = 12 V, measured at f = 10 Hz).

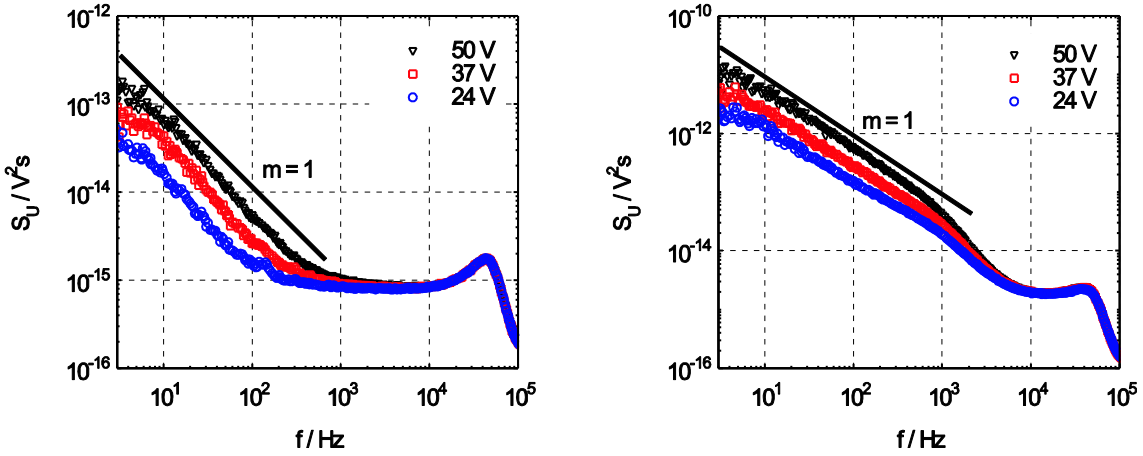

Figure 4.3: Low frequency noise spectra of the detector with connected guard ring electrode. Reverse biased contact A (left), reverse biased contact B (right).

The low frequency noise spectra of the investigated detector with connected guard ring are in fig. 4.3. In the monitored frequency range, which was limited to 1000 Hz due to internal noise of the measuring system, I observed an excess noise spectrum of generic $1/f^{\,1}$ type. The magnitudes of the noise spectral densities at f = 10 Hz were 2.4 × 10^{-12} V^{2}s for U = 24 V and 1.32 × 10^{-11} V^{2}s for U = 50 V when the contact B was reverse biased. The reverse biased contact A exhibited noise spectral densities: 4.4 × 10^{-14} V^{2}s for

U = 24 V and 1.75 × 10^{-13} V^2s for U = 50 V, which are 2 orders of magnitude lower. Detector bulk acts as the same source of excess noise, regardless of defects distribution in the sample volume; this apparent difference is caused by an increased number of defects or imperfections in the area of contact B. In case of disconnected of guard ring electrode, this behavior is masked.

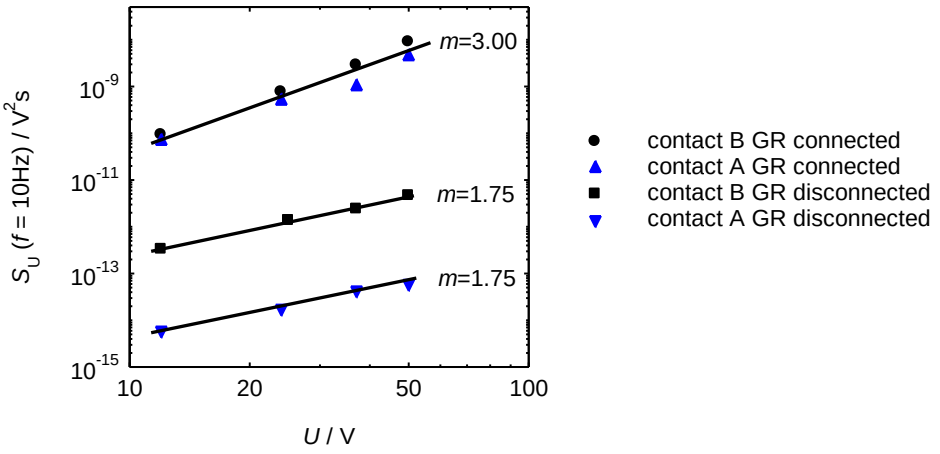

Figure 4.4: Dependence of power spectral density of the noise signal on the applied bias voltage at f = 10 Hz. Configurations with and without connected guard ring electrode are shown.

Figure 4.4 shows dependences of power spectral densities of the noise signal on the applied bias voltage The power spectral density of the noise signal generated by the surface increases with the power 3.091 (reverse biased contact A) and 2.873 (reverse biased contact B) with increase of the applied voltage. The power spectral density of the noise signal, generated by the bulk and contacts, rises with the power of 1.75 (reverse biased contact A) and the same value was obtained for the reverse biased contact B. As can be seen, the increase of power spectral density with the applied voltage is independent on the bias polarity.

This experiment showed that untreated detector surface was found as the bottleneck of detector system; it generates the highest contribution to the total leakage current of the detector. Surface acts as a conductive layer with high concentration of unwanted impurities. Increased concentration of defects worsens rectifying properties of both Schottky contacts by means of the potential barrier height lowering. The resulting *I-V* characteristics of the detector investigated with unutilized guard ring electrode mask the properties of the contacts and the bulk. The *I-V* characteristics with disconnected guard ring electrode for both bias polarities were very symmetrical and their shape indicates the presence of the carriers' injection, which leads to non-linearity of the *I-V* characteristics. After employing the guarding electrode, the contact asymmetry was revealed. The contact A showed better rectification efficiency and has lower contribution to the detector total additive noise. Utilization of the guard ring electrode caused two orders lower leakage currents and suppressed the total magnitude of the detector noise by 5 orders. Observed low frequency noise had $1/f^m$ character with the slope m close to 1. At frequencies above 1 kHz, the slope m has increased. This was caused by the generation-recombination processes induced by irregularities at the contact area. Surface treatment (passivation

or/and the guard ring electrode utilization) is beneficial processing step in CdTe based radiation detectors manufacturing to obtain a high quality spectroscopic radiation detector.

4.2 Analytical investigation of bias induced polarization in CdZnTe detectors

The main reason why Schottky (or diode) type CdTe detectors are fabricated is to suppress the league current. Unfortunately, it has been showed instability with time under bias voltage and their collection properties degraded on the hour time scale showing polarization effect [34, 35]. This effect has been observed through many years in CdTe detectors and its origin is not fully attributed.

The ionization of the deep acceptor by hole detraping and inducing a space charge buildup is most often reported as a responsible mechanism for polarization phenomena that happened on short time (detrapping time is on munutes time scale) [35]. On the other hand, electrode interfaces were showed an effective role on the polarization effect [36]. From these reasons, the instability problem is studied by investigation of the dynamics of the space charge in the depletion region at the metal-semiconductor interface. In this part of my work, the Pockels effect and current-time measurements were performed in this work.

This study includes the experimental results acquired on Au/CdZnTe/Au Schottky planar detector with dimensions 5 × 5 × 2.5 mm^3 made of (111) oriented single crystal CZT. (111) oriented single crystal and perfect surface smoothness are the essential requirements to obtain Pockels images of a good quality. In this case, gold was deposited on opposite surfaces of the sample by evaporation. The sides of the sample were optically polished with final 0.05 mm grit and chemically etched in 1 % Br-methanol solution for 1 min. The CdZnTe sample used in the study was detector-grade with mobility-lifetime product of electrons $\mu\tau_e \approx 1x10^{-3}$ cm^2/V. All measurements were carried out at a temperature of 300 K and steady-state conditions. The measurement setup was upgraded. Previously used system based on Agilent instruments was replaced by the Keithley 6517 electrometer with integrated 1kV source. This change required design of a new measurement software that was done in the LabView environment.

Pockels effect measurements were used to monitor the spatial distribution of the electric field through the studied detector. CdZnTe is a zinc-blend crystal exhibiting a linear electro-optic (Pockels) effect. It acts as an optically isotropic material in the absence of an applied voltage. When a voltage is applied, CdZnTe becomes a double-axis anisotropic material and its refractive indices are dependent on the electric field *E*. Using this effect, the distribution of the electric field through the sample can be estimated by a crossed-polarizer technique, where the local electric field strength in the direction perpendicular to light propagation is given by:

$$E(x,y) = \arcsin\frac{\sqrt{I(x,y)/I_0(x,y)}}{\gamma},\ \gamma = \frac{\sqrt{3}\pi n_0^3 r_{41} d}{2\lambda}. \quad (63)$$

With respect to the direction of the applied electric field and crystal orientation, where I (x,y) is the transmitted light intensity; I_0 (x,y) is the transmitted light intensity with parallel polarizers under zero bias. λ = 980nm is the wavelength of the used light; n_0 =2.8 is the field-free refractive index of CdZnTe at 980 nm; r_{41} = 6.5×10 −12 m/V the linear electro-optic coefficient and d = 5mm is the optical path length. The experimental setup is sketched in Fig 4.5.. A Near- Infrared InGaAs CCD camera was used for sensing the testing light. Ag target X-ray tube and tunable Ti:Sapphire laser were used for sample excitation.

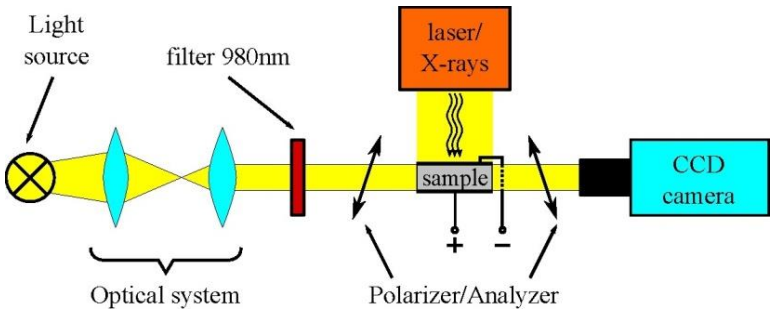

Figure 4.5: Pockels effect experimental setup. Collimated testing light cut by narrow band filter at 980 nm passes through the biased sample situated between two crossed polarisers is sensed by NIR InGaAs CCD camera. Excitation radiation (laser or X-rays) passes through semi-transparent cathode.

According to the conventional model of charge accumulation, it has been considered that the application of a bias voltage to a CdTe detector with a Schottky contact sweeps the holes out of the depletion volume from the deep acceptors level (called detrapping). In this process, deep acceptors negatively ionize with a detrapping time τ given by

$$\tau = \frac{1}{N_V \sigma v}\exp\left(\frac{E_T}{kT}\right), \quad (64)$$

where $N_V = 2\left(\frac{2\pi m^* kT}{h^2}\right)^{3/2}$ and $v = 2\left(\frac{kT}{2\pi m^*}\right)^{1/2}$ are the effective densities of states at the valence band edge and the thermal velocity of holes, respectively. E_t is the trap ionization energy, σ is the acceptor capture cross section.

When a bias voltage is applied at time t = 0, the concentration of the ionized deep acceptor N^- will change as

$$N^-(t) = N_T[1-\exp(-t/\tau)] \quad (65)$$

and the field potential function $\varphi(x,t)$ will be obtained by solving Poisson's equation as

$$\frac{d^2\varphi(x,t)}{dx^2} = \frac{eN^-(t)}{\varepsilon_s} = \frac{eN_T}{\varepsilon_s}[1-\exp(-t/\tau)], \quad (66)$$

where x is the position from the interface of the Schottky contact. Almost, all the bias voltage develops across the depletion layer L_d,, (this is observed from the Pockels measurements) therefore the distribution of electric field $E(x,t) = -d\varphi/dx$ in the depletion region is obtained by solving eq. 66 with the boundary conditions $\varphi(0) = U$, and $\varphi(L_d) = U_{12}$.

Here U_{12} is the part from the external applied voltage that develops across the bulk semiconductor sample and the forward bias contact ($U >> U_{12}$), then

$$E(x,t) = \frac{eN_T}{\varepsilon_s}[1-\exp\left(\frac{-t}{\tau}\right)](L_d - x) + E_{12}. \quad (67)$$

Here, $E_{12} = U_{12}/(D-L_d) \approx U_{12}/D$, D is the sample thickness, and the depletion layer thickness, L_d, is given by

$$L_d(t) = \sqrt{\frac{2\varepsilon_s U}{eN_T[1-\exp(-t/\tau)]}}. \quad (68)$$

Using eq. 67 in eq. 4 yields

$$E(x,t) = \sqrt{2\alpha U} - \alpha x + E_{12}, \ \alpha(t) = \frac{eN_T}{\varepsilon_s}[1-\exp(-t/\tau)]. \quad (69)$$

For certain time, t and thickness $x < L_d$, the relation between the internal electric field E and $U^{1/2}$ is straight line with the slope α from which the total acceptors concentration, N_t and τ will be determined from the Current –time measurements.

4.2.1 Electric field distribution in the sample

The electric field distribution through the sample is obtained from the Pockels measurements and eq. 69. Fig. 4.6 represents the one-hour time decay of the internal electric field profiles in the studied sample when the bias is 50 V. It is observed that most of the bias is developed across the reverse biased contact of the structure.

Redistribution of electric field in time is apparent. Right after biasing, the electric field is distributed towards cathode up to distance of 0.15 mm. As time goes on, the electric field distribution changes and grows in vicinity of the anode. As can be seen, the dead layer that has no electric field grows during the polarization. This effect reduces collection efficiency and spectral sensitivity of the detector since the carrier collection becomes more and more incomplete.

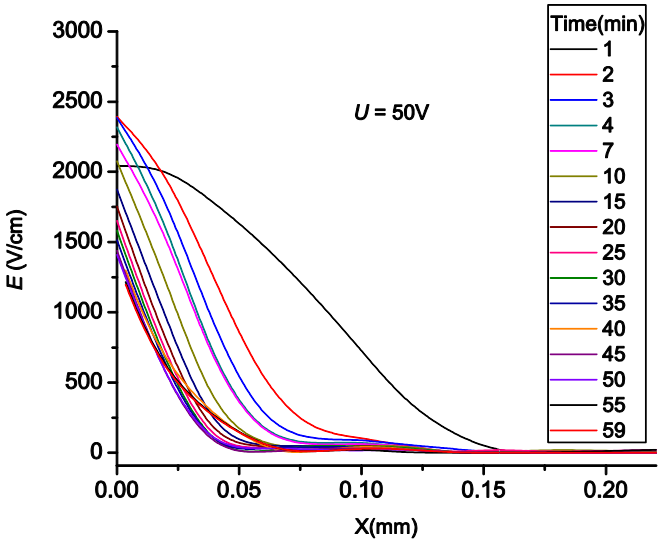

Figure 4.6: Distribution of the electric field with time through the sample acquired by the Pockels effect measurements.

The Pockels measurements were performed for different applied voltages across the studied sample. At certain thickness $x < L_d$ from the anode, the electric field is determined as function of time and of the applied voltage. The results of these measurements when x = 0.059 mm is presented in Fig. 4.7 (right). At certain time, t = 900 s, the value of electric file is plotted versus the $U^{1/2}$. The result is a straight line that is in agreement with eq. 69, shown Fig. 4.7 (left), the slope α = 528.85 V / cm^2

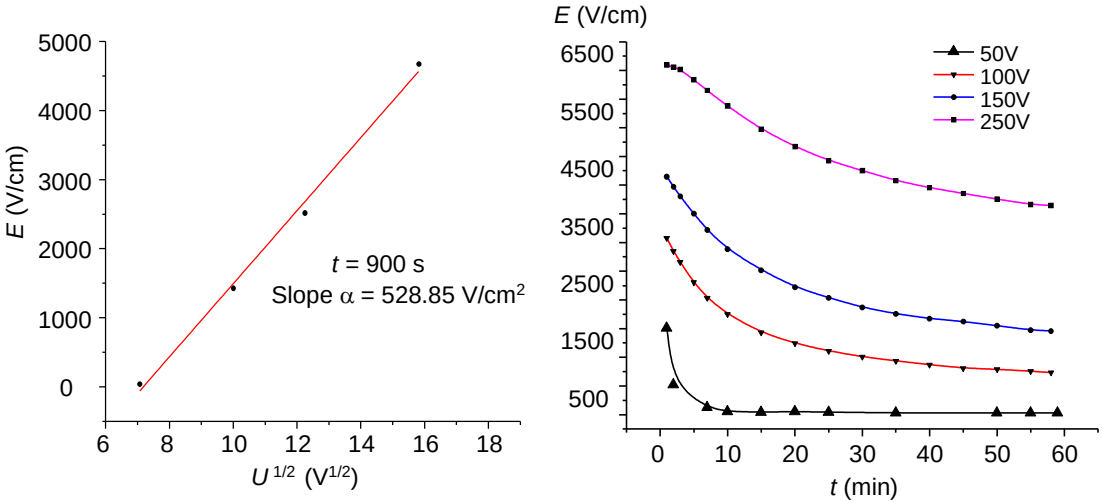

Figure 4.7: Left: Linear relationship between electric field and the square root of the applied voltage. Right: Electric field decay at different bias at x = 0.059 mm from the anode.

4.2.2 Current instability measurements and parameters retrieval of the structure

The instability in current of the studied sample at 100 V bias is presented in Fig. 4.8. The best fitting of data gives detrapping time τ =2728 s. Using values of τ and α to eq. 69,the carrier concentration found to be $N_t = 1 \times 10^{10}$ cm^{-3}, which is reasonable value for

such detector material. Supposing the electron capture cross section is $\sigma = 10^{-17}$ cm^2 and using τ =2728 s in eq. 69, the trap energy level is found to be E = 0.88 eV.

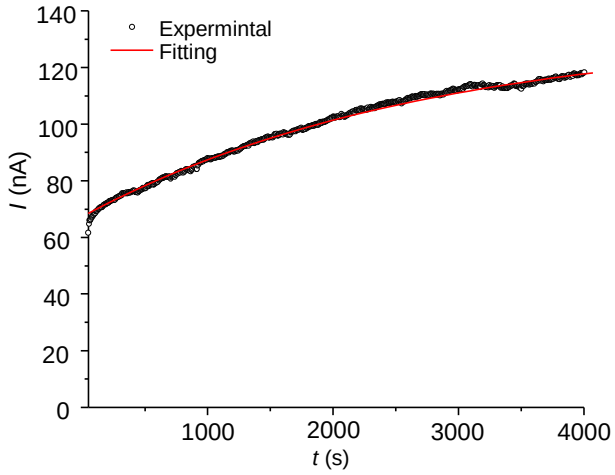

Figure 4.8: Current stability of studied sample at 100 V.

4.2.3 Investigation of 1/*f* noise evolution during polarization

Figure 4.9 (left) shows the evolution of the low frequency noise spectrum of the analysed detector in time. $1/f^{\,m}$ noise is again the dominant noise type in observed frequency band. At frequencies below 100 Hz, the slope m of the $1/f^{\,m}$ noise was very close to 1. The corner frequency of the $1/f^{\,m}$ noise with m = 1 gets lower during the polarization. This trend follows the $1/f^{\,m}$ noise with $m > 1$. The increase of the m parameter is caused by an increasing ratio of the generation-recombination processes in the total noise spectrum.

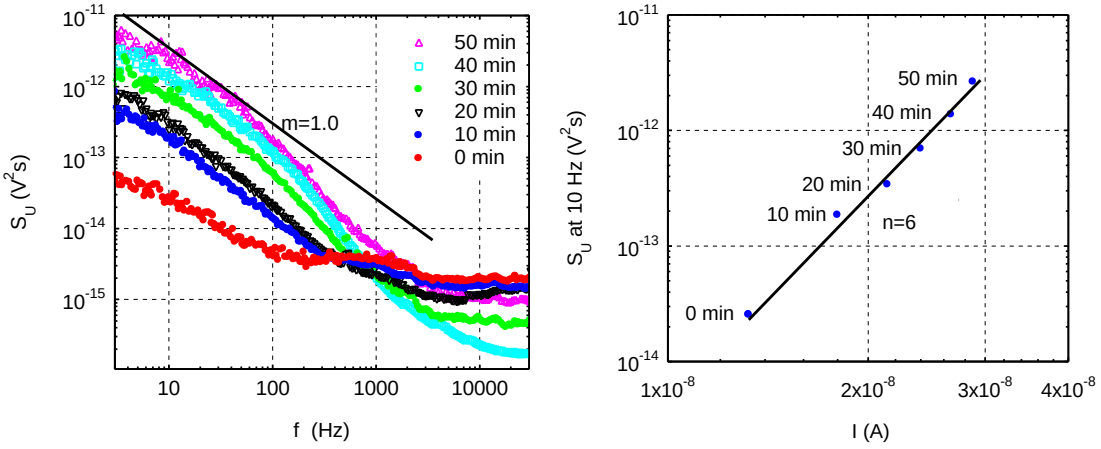

Figure 4.9: Noise spectral density evolution during polarization of the analyzed detector (left) and an increase of the noise spectral density with current. Applied voltage was 100 V.

The signal spectrum sampled in time of biasing shows a dominant $1/f$ noise with a corner frequency of 200 Hz. At higher frequencies, the detector noise signal spectrum showed a shot noise shape, for which the slope m is typically 0. The noise spectrum

acquired 10 minutes after biasing, exhibits a $1/f^m$ noise corner at units of kHz. Later noise spectra, sampled 20, 30, 40 and 50 minutes after detector biasing, exhibit a decrease of shot noise spectral density level, which indicates a lowering effect of the shot noise during the polarization. For certain frequencies, e.g. at 100 Hz (t = 30 min) and at 70 Hz (t = 50 min), I observed an increase of the slope of the $1/f^m$ spectra from m = 1.4 (t = 20 min) to m = 2 (t = 50 min). As in case of the $1/f^{m=1}$ noise, the reason for this increase is a strengthened effect of the generation-recombination noise, which is typical for the trapping-detrapping process of carriers from energy states located in the band gap [38]. The nature of fluctuations is based on temporary excess of carriers during the generation process and its reduction during the recombination process. The resulting sum of the generation and recombination processes produces the Lorentzian shape of the spectrum with its typical slope of m = 2 [38].

Figure 4.9 (right) has information about the dependence of the power spectral density on the leakage current during the polarization process. The increase is proportional to the power of n = 6 of the current. This finding is in contrast with theory, proposed by Hooge, which presumes an increase of the power spectral density with the square of the detector current. This disproportion can be described as follows: Hooge assumes a constant number of charge carriers in the system. This idea can be accepted in case of devices, where polarization is absent (MOSFETs devices etc.). In our case, after biasing the detector, charge carriers are detrapped from deep energy levels also in the space charge region forming a screen to the applied electric field. Carriers situated "in the shadow" of space charge become inactive for the overall electric charge transport of the detector. This mechanism causes an increase of the noise spectral density not only due to the current increase, but also due to the change of total carrier number in the detector system. Of course, this idea is in contraction with the measured increase of the detector current in time, but the increase is primarily a result of the potential barrier height lowering during the polarization [34].

The analysed sample suffers from significant current instability in time. In the observed time interval of 45 000 seconds. Such long time cannot be easily explained by conventional charge accumulation model. Furthermore, the detector current transient towards higher current has not ended. During the investigated time interval, the electric field showed a drop of the strength at the cathode area. As a result of the space charge build-up, the noise spectral density shows a higher increase during the detector polarization than proposed by the Hooge theory.

4.3 Analysis of the contact symmetry and its impact on the low frequency noise.

Manufacturing imperfections, especially difficult reproducibility of the contact deposition lead to variations of the *I-V* characteristics and fluctuations of electric signal that result in determination of the detector performance. This part of my work is aimed to analyse one of the key factors influencing detector performance: the symmetry of electrical parameters of the detector's contacts with the same geometry. For this analysis,

the *I-V* characteristics, long-time current stability and additive noise of contacts are investigated.

For this work, a detector based on an n-type indium doped CdTe crystal is used. Its dimensions are 5 × 5 × 1.4 mm^3. Golden contacts were chemically deposited on the opposite surfaces of the sample from aqueous solution of $AuCl_3$. The sides of the sample were polished with final 3 μm grit and etched in 0.5 % Bromine-Methanol for 1 min. The specific resistivity of the analysed sample is $\rho = 10^8$ Ωcm. This sample was intentionally used since it shows very asymmetric *I-V*s.

4.3.1 Current-Voltage characteristics asymmetry

Results of measurements on the investigated CdTe sample are shown in Fig. 4.10. The *I-V* characteristics are non-linear at low voltages and resistance of the sample increases with decreasing temperature. I have compared rectifying effect of each contact and its dependence on operating temperature. Fig 4.10 (left) shows detector with "poss" polarity. In this bias orientation, the detector shows good rectifying effect with linear reverse current increase with increasing bias. Already at 315 K, apparent instability can be noticed from fluctuation of the current at voltages higher than 20 V. At temperature 325 K and voltage above 20 V, a decrease of resistivity appeared. This is caused by defective state of the contact

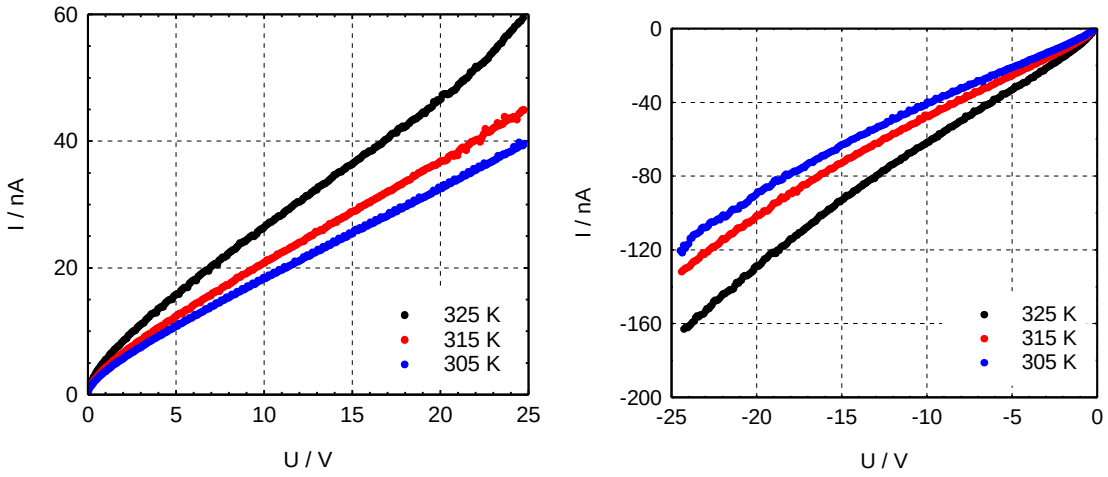

Figure 4.10: Current- Voltage characteristics of the "poss" (left) and of the "neg" (right) biased detector. Operating temperatures were 305 K, 315 K and 325 K.

In the case of "neg" polarity that is plotted in Fig 4.10 (right), the second contact acts as rectifying (Still, the "S" shape at the low voltages is present), but the leakage current is approx. three times greater than in case of the "poss" polarity. The rectifying effect is obviously worse than tin the "poss" polarity. The cause of higher leakage current for the "neg" polarity is increased recombination in depleted layer of the contact. The *I-V* characteristics are bent to become super-linear with increasing bias and the effect of the hole injection is apparent from -15V for all temperatures.

4.3.2 Comparison of the noise properties of asymmetric contacts

In Fig 4.11 are low frequency overall noise spectra of the investigated sample for both bias polarities. Applied voltage was 25 V. As can be seen, the reverse biased contact in the "neg" polarity shows an order higher magnitude of detector's additive noise spectral density. At low frequencies, the slope *m* of $1/f^{\,m}$ noise was close to unity. For the "neg" polarity, change of spectrum slope to higher value *m* = -1.60 at 100 Hz can be seen. In case of the "poss" polarity, the spectrum slope changed to -1.80 from 30 Hz. The non-uniformity of the slope m among both spectra is caused by different distribution of traps / defects in M-S interfaces of each contact.

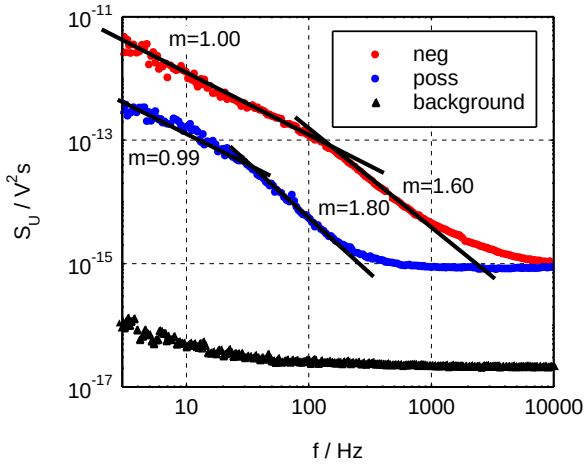

Figure 4.11:Comparison of the Low frequency noise spectra of the detector for both bias orientations. The applied bias was ±25 V, measured at temperature 305 K. Black line denotes noise background.

The $1/f^{\,m}$ noise corner lies at 300 Hz ("poss" polarity) and at 3000 Hz ("neg" polarity). At higher frequencies, the shot noise type with its typical slope *m* = 0 dominates. In Fig. 4.12 are plotted dependence between the value of noise spectral densities at *f* = 10 Hz on operating temperature and the applied voltage for "poss" polarity.

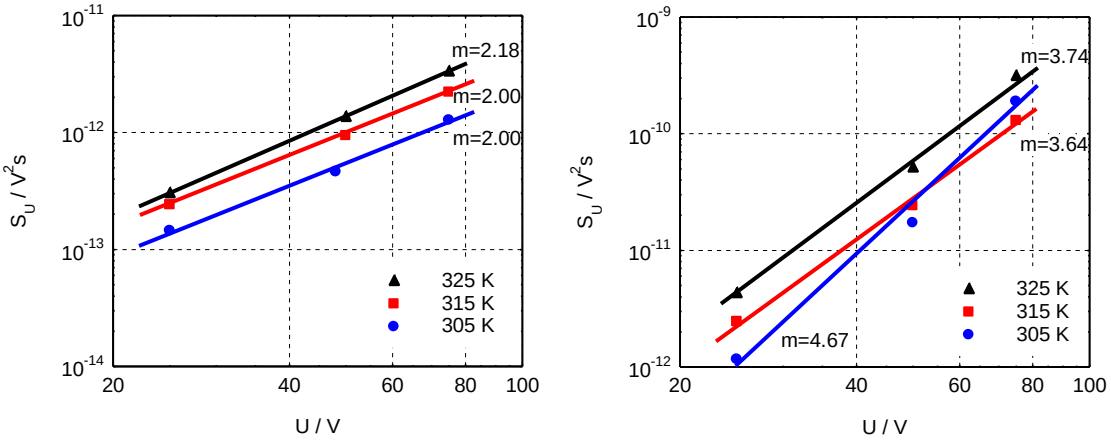

Figure 4.12:The values of the. noise spectral density of sample at frequency *f* = 10 Hz vs. applied voltage. "poss" (left) and "neg" (right) bias voltage orientation. Operating temperatures were 305 K, 315 K and 325 K.

The values of the power spectral density increase with operating temperature of detector. Further information from both graph in Fig. 4.12 is that noise spectral densities increase with temperature. Thus, cooling of the device will be always beneficial and improves its signal-to-noise ratio. The faulty “neg” reverse biased contact shows higher increase of the noise power spectral density than the “poss” one, always higher than half fold between the values at 25 V and 75 V. I find the value for the “neg” contact at 305K for U = 75 V not well measured since taking into account only bias voltages 50V and 25V, the fit will yield similar value of m as for T = 315 K and 325 K, i.e. -3.72. The parameter m denotes by which exponent does the value of noise power spectral density increases with applied voltage at certain frequency. Values of m close to the ideal slope value of 2, assuming increase of the noise spectral density magnitude with the second power of applied voltage. Reverse biased contact at “poss” polarity does not contribute to the detector system overall noise that mostly originated in the bulk and manufacturing quality of such contact is very good. In contrary, the reverse biased contact at “neg” polarity is the dominant noise source in the detector system. The noise spectral density at f = 10 Hz increases with the power of m = 4.67 to 3.64 (depending on operating temperature), which is a result of worse contact quality.

To sum up, the investigated sample showed serious asymmetry of electrical parameters, caused by the difference between qualities of each contact. The measurement results points to presence of higher concentration of defects in metal- semiconductor contract area, which lead to the barrier non-uniformity and increase of the leakage current. The contact imperfection also causes additional noise of the detector, significantly increasing with applied bias voltage.

5 Investigation of thermal stress effect on CdTe detectors

Motivation of this part is the fact that one of typical features of CdTe and CdZnTe is irreversible changes of the detector parameters that start at relatively low temperatures around 400K. This behaviour might be related to different thermodynamic properties of Cd and Te. The nature of irreversible changes in the detector structure and the effect of them on not only electrical, but also structural properties of the CdTe detector system is subject of the following chapter.

For this purpose, the indium doped n-type CdTe with planar Au/CdTe/Au contact configuration with dimensions 4 × 4 × 1.3 mm^3 was chosen. The sample was detector-grade with mobility-lifetime product of electrons $\mu\tau_e \approx 1x10^{-3}$ cm^2/V. Surface polishing and its subsequent chemical etching in the same as for the previous samples. In order to cause thermal degradation of the detector, the sample was exposed to temperature 420 K for 48 hours in the air.

5.1 Effect of high temperatures on transport characteristics

Figure 5.1 (left) shows the *I-V* characteristics of the sample before exposing to high temperatures. As can be seen, the characteristics shows apparent nonlinearity, with typical "S" shape for Au Schottky contacts. For both detector polarities, the slope of the *I-V* curve changes at the bias voltage 7.7 V. The steeper rise of detector current with increasing voltage below above mentioned bias voltage are followed by characteristics that exhibits a linear relationship between the applied voltage and the resulting electric current. The border voltage indicates full operation of the Schottky barrier of the detector. At voltages high enough for complete depletion, the detector has resistance 3.85 GΩ, which is value that meets the requirements for a good spectroscopic detector. The bulk resistivity was estimated from the *I-V* data measured at the low bias voltages. Received value of resistivity is $\rho = 3 \times 10^9$ Ωcm.

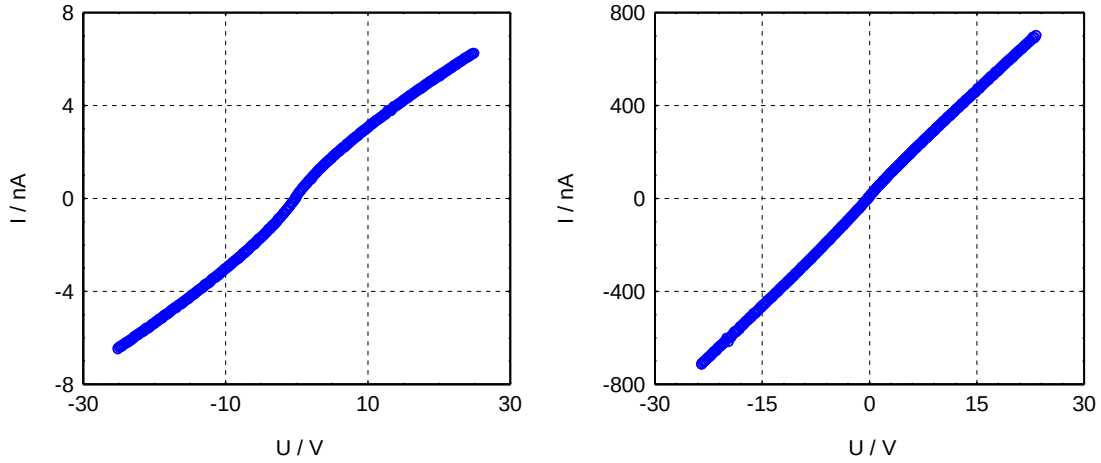

Figure 5.1: The I-V characteristics of detector before (left) and after (right) exposure to 400K for 48 hours.

The *I-V* characteristics of analysed detector after thermal stressing are shown in Fig. 5.1 (right). Compared with the unstressed detector, the leakage current of the sample increased by two orders. Degradation of the crystal caused worsen rectifying effect of the reverse biased Schottky contact. After the thermal degradation caused by heat stressing, the dynamic resistance of the detector decreased to 31.5 MΩ. Such value corresponds to the resistivity of $\rho = 4 \times 10^6$ Ωcm that produce too high leakage current for a good spectroscopic detector. The effect on the metal-semiconductor interface will be explained in later text.

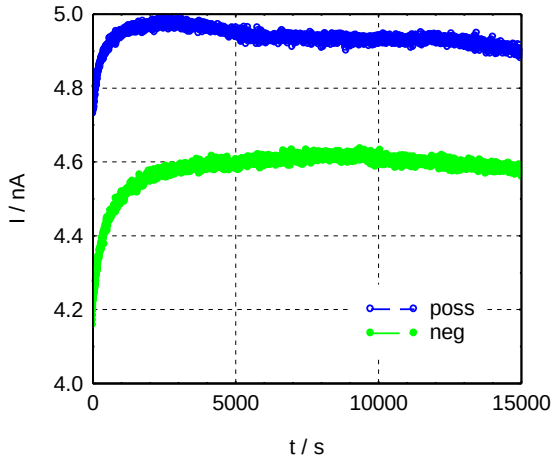

Figure 5.2:Current transients after the detector biasing of the detector before thermal stressing. Applied voltage was 20 V.

To analyse changes of detector polarization, long time current measurements have been carried under applied voltage U = 20 V. Such current transit represents the macroscopic effect of polarization. Current transient recorded for the unstressed detector is in Fig. 5.2. An abrupt rise of the current in time at the first 2000 seconds after biasing is notable. Even though *I-V* characteristics of detector before heat stressing show symmetry for both polarities and the symmetry is maintained after stressing. The differences of the current transients appeared. The current quickly increases with time in the beginning, and reaches saturation after about 2500 seconds. After about 2500 seconds from application of bias, almost all carriers are de-trapped. I observed slight differences of the current transit for each bias polarity in maximal values of leakage currents (5 nA for the "poss" polarity, the 4.6 nA for "neg" polarity at t = 2500 s). In time > 2500 s after the detector biasing, the leakage currents still fluctuate. This is caused by unstable properties of M-S interfaces for both polarities due to ongoing carrier trapping-detrapping processes.

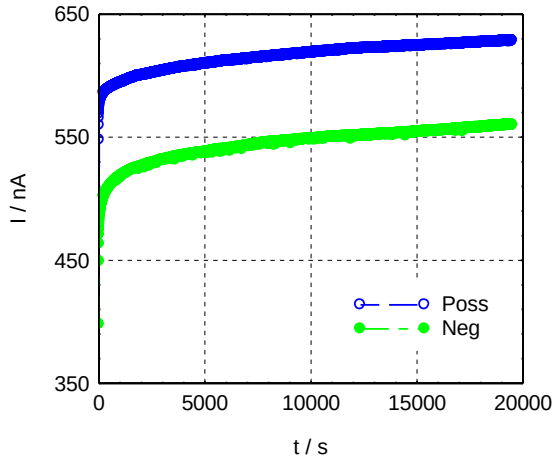

Figure 5.3: Current transients after the detector biasing of the detector after thermal stressing. Applied voltage was 20 V.

Fig. 5.3 shows the current transit of the detector after heat stressing. As in case of the *I-V* characteristics measurement, the detector showed approx. two orders higher

values of leakage currents. After 1000 seconds, when I observed an abrupt rise of the detector current, the detector current was increasing linearly for both polarities. The shape of time evolution of current transit is very similar and the carrier re-trapping processes has not ended in observed time interval. As in the previous case, the detector biased in the "neg" polarity, showed higher values of leakage current. The duration of fast current change was, compared with current transits of the unstressed detector, faster. That point to existence of a new defect energy level situated closer to the conductivity band, which effect is faster detrapping. The continuous increase of the detector current is caused by another, deep level, for which is typical long time detrapping. One can see identical shape of the current transients for both polarities. I attribute this as a result of crystal bulk resistance increase. Therefore, fluctuations of the current transit are masked since they originated in the contact area.

5.2 Effect of high temperatures on noise properties

As I mentioned in section 4.1, I found out that contact behaviour is masked by the most dominant source of the detector additive noise – the surface. Subscription of contacts to the total noise of the detector can be revealed only, if an extra guard ring electrode that grounds surface current is presented. The used sample was not equipped with this electrode, so the total additive noise of the detector is analysed. To avoid the influence of the detector polarization effect, all the noise measurements were carried out 30 000 seconds after the detector biasing.

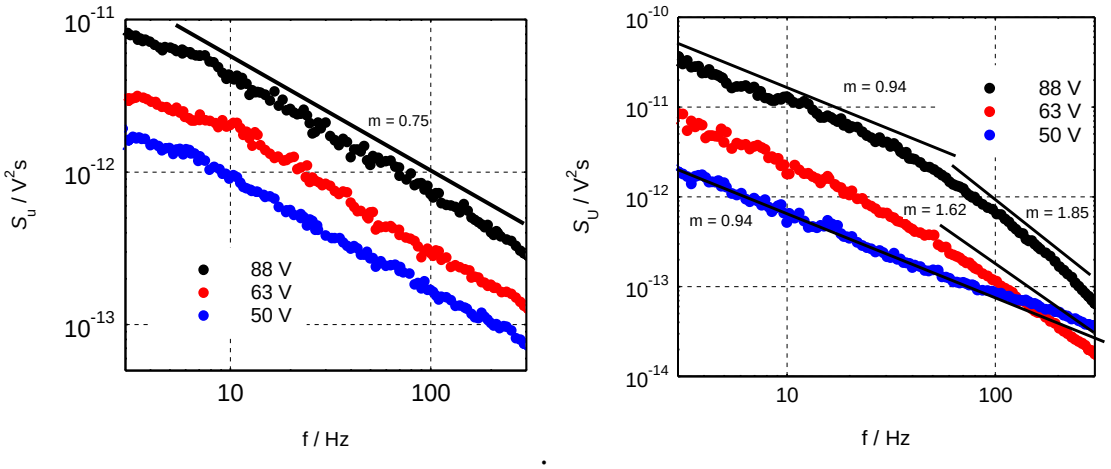

Figure 5.4: Low frequency noise spectra of the detector before(left) and after(right) thermal stressing. Applied voltages were 88 V, 63 V and 50V

Figure 5.4 (left) shows the low frequency noise spectrum of the detector before heat stressing. The detector exhibits the generic $1/f^{m}$ noise with the slope m = 0.8. The value of m is constant in the whole observed frequency range. The low frequency noise spectra of the detector after thermal stressing are shown in Fig.5.4 (right). In the case of U = 50 V (whole frequency range) and frequencies below 30 Hz (U = 63 V and U = 88 V) the slope of the spectra was very close to 1. At frequencies above 30 Hz, the value of spectra slope has increased to the value of 1.62 (U = 66 V) and 1.85 (U = 90 V). As in the previous cases, this is caused by the reinforced effect of the generation – recombination noise. This

change is caused by different distribution of Lorenzians in the spectrum, where each trap is defined by specific detrapping time and has its own Lorenzian. The values of the noise spectral density at f = 10 Hz were measured 6.65 × 10^{-13} V^2s for U = 50 V, 2.20 × 10^{-12} V^2s for U = 63 V and 1.25 V^2s for U = 88 V.

The most remarkable change of the detector additive noise behaviour before and after applying thermal stress is the increase of the noise spectral density with increasing voltage. Voltage noise spectral density increase is in the case of unstressed detector proportional to the power of 2.60 with the applied voltage as it is shown in Fig. 5.5.

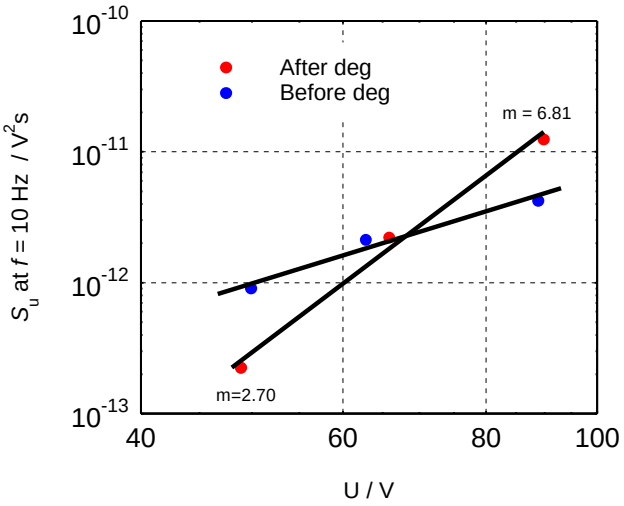

Figure 5.5: Dependence of the power spectral density of the noise signal on the applied bias voltage at f = 10 Hz.

After heat stressing, I observed a distinct change of this parameter to 6.81. The value of 2.6 is close to the value assumed by Hooge. eq 57 can be rewritten for the voltage spectral density

$$\frac{S_U}{U^2} = \frac{\alpha}{Nf}, \tag{70}$$

where S_U is the noise spectral density of a fluctuating voltage U developed in a material bulk between the terminals of a linear system when a current is injected into it; α = 10^{-3} is the Hooge constant for CdTe.This heuristic formula presumes that the value of the noise spectral density is proportional to the square of the applied voltage. Higher value is caused by a fundamental requirement breach – the requirement of a uniform distribution of defects in the material bulk. Imperfections are always present in bulk and, furthermore, just the presence of Schottky barrier is an unexceptionable place of inhomogeneous distribution of charge carriers in the detector system. Further deviations from prefect state cause higher increase of the noise spectral density than with the square of the voltage. So, after the detector heat stressing, input parameters for calculation eq. 70 are changed, especially N, which, due to the generation of defect sites in the crystal structure, increases. To conclude, heat stress caused increased carrier concentration in semiconductor bulk. This fact has a multiple effect. Not only conductivity of the detector bulk increased, but higher concentration of charge carriers caused worsen rectifying properties of reverse

biased contact by thickening the potential barrier. Current transit of detector before thermal stressing lasted 15 000 seconds whereas the current transit of the detector after exposing to high operating temperature has not ended in the observed time period and the detector leakage current was still increasing. The increase of the power spectral density with applied bias voltage was found as the most obvious indicator of the detector ageing.

5.3 Structural and morphological investigation of Metal- Semiconductor interface of CdTe detector exposed to heat stressing.

Motivation of this part of my work is to investigate interfacial chemistry of the Metal-Semiconductor interface of thermally unstressed and stressed detector. Various methods of the contact deposition (magnetron sputtered, e-beam evaporated, chemically deposited) can yield into different elemental composition of the interface that is accompanied with variation of the detector's electrical and spectroscopic performance. For my analyses, I chose X-ray Photoemission Spectroscopy, Atomic Force Microscopy, Scanning Electron Microscopy, Scanning Auger Microscopy X-ray Diffraction and Secondary Ion Mass Spectroscopy as tools for the analysis. Deeper insight to the contacts properties given by the Schottky theory is presented.

I have used two detectors for the analyses. The aged one I used in section 5.1 (ageing) and a newly fabricated sample that was made from the same crystal by the same procedure as the stressed detector. Dimensions of both detectors are the same.

5.3.1 X-ray photoemission analysis

The principle of X-ray Photoemission Spectroscopy (XPS) is based on the photoelectric effect. As a result of inelastic collision of photons with electrons in analysed specimen, the electrons from inner shell (core) are emitted into the vacuum. According to their kinetic energy and count rate *CPS* received from the flux measurement, these electrons are separated in hemispherical analyser. Electrostatic fields within the hemispherical analyser are established to allow only electrons of a given energy range (Pass Energy) to arrive at the counting detector. Pass energy defines the resolution of the analysis.

X-ray sources provide improved energy resolution by filtering a narrower band of X-rays from the resonance. X-ray diffraction through quartz crystal allows only certain wavelengths to be reinforced into a spot and so monochromatic X-rays can be directed at a sample. The crystal spacing is such that X-ray wavelengths that are multiples of the Al K-α X-ray resonance are reinforced by virtue of the Bragg relationship for X-ray diffraction [38].

Due to known photon energy of the irradiating X-ray beam and aquired kinetic energy, this method allows us to study binding energy of every chemical element, whose atom number is higher than 2. Due to relatively low interaction depth of the X-ray source, this method is optimal for surface and interface analysis.

5.3.1.1 Principle of atomic core level photoionisation

The energy of a photon of all types of electromagnetic radiation is given by basic relation $E = hf$ .The process of photoionization $A \rightarrow A^+$ followed by electron emission can be described as

$$A + hf \rightarrow A^+ + e^- \tag{71}$$

and the rule of energy conservation requires

$$E(A) + hf = E(A^+) + E(e^-)\,. \tag{72}$$

The energy of emitted electron is entirely presented as the kinetic energy E_k, formula 72 can be rewritten as

$$E_k = hf - (E(A^+) - E(A))\,. \tag{73}$$

The term in outer bracket represents the difference between the ionized and neutral atoms, which is called the binding energy (*BE*) of the electron. Hence

$$E_k = hf - BE\,. \tag{74}$$

A simplified graphical explanation of the process of ionization is shown in Fig. 5.6.

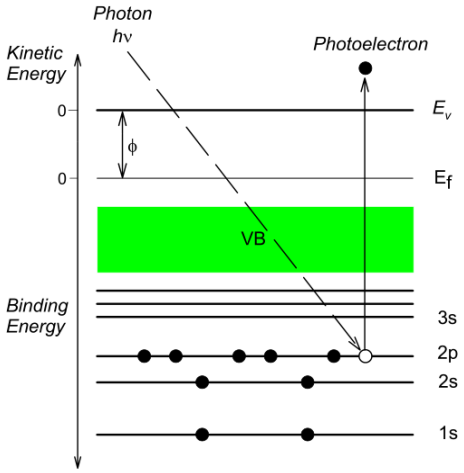

Figure 5.6: A simplified explanation of the atom ionisation by emission of the electron from its core level.

As I shown in Section 5.1, exposure of the detectors to operating temperature above 400 K causes irreversible changes in their electrical properties. To carry out further investigation of these changes, the XPS was used as probably the best available tool to monitor the changes of the chemical composition of the fresh M-S interface and interface after irreversible degradation. I recorded the sets of XPS spectra of the most important elements, i.e. of Te 3d, O 1s, Cd 3d, C 1s for the surface and metal-semiconductor interface of unstressed sample and a thermally stressed sample.

The analyses were carried out with the Kratos Axis Ultra DLD spectrometer using a monochromatic Al Kα (hf = 1486.7 eV) X-ray tube operating at 150 W (filament current was set to 10 mA, 15 kV). The monochromated beam of X-rays were focused into a spot

with dimensions of 2 × 2 mm on the sample. Since relatively strong charging effects were appeared during the photoemission measurements (as an effect of high electric resistivity of the crystals), the Kratos charge neutralizer (low energy electron flood gun) was used to restore the charge balance on the surface for all analyses.

In the first step, wide energy spectrum is acquired. At points of interest (Cd, Te and their metal transitions and oxides), the high resolution spectra were measured with the step size 0.02 eV and with pass energy of 20 eV. Instrument base pressure was 2×10^{-8} Pa. The Kratos spectrometer evaluates atomic concentration with precision of ± 0.1 %. For quantitative XPS analysis, the least-squares fitting of the spectra was performed using the commercially available CasaXPS software. A Doniach–Sunjic line shape was used to obtain the best fit of asymmetric doublets. A standard Shirley background subtraction method is used for all sample spectra. The adventitious C1s photopeak at 284.8 eV was used as the reference for calibration of the peak positions. To identify photoemission peaks, the Thermo Scientific XPS Database [40], the U.S. National Institute of Standards and Technology XPS Database [41], the XPS Reference Pages of the University of Western Ontario [42] and The Scienta ESCA 300 Database [43] were used.

5.3.1.2 Survey scans of the detectors surface.

Figure 5.7 shows survey spectrum of the non-degraded sample and Fig.5.8 depicts the survey spectrum of the degenerated sample. Supposedly, due to expected thickness of electroless deposited gold layer of approx. 10 nm and the depth of X-rays interaction to the sample volume is approximately 4 nm. Wide scans should include only gold with some surface oxides and some surface contaminants, mainly of organic origin. Both spectra already consist Te and Cd with unneglectable atomic concentrations of 8.82 atomic percent (at%) for Te and 6.29 at% for Cd (unstressed detector). For the case of unstressed detector, the detected atomic concentration values of Te were 10.01 at% and 4.84 at% for Cd. Already presented Cd and Te is result inhomogeneous thickness of the gold layer. This is caused by mechanical scratches on the gold layer. Furthermore, it is difficult to control thickness of the gold layer by electroless deposition.

One can see the untagged peak at binding energies of approx. 70 eV. This binding energy can be attributed to Bromine residuals [40], because both samples underwent standard preparation procedure, i.e. were chemically etched in Bromine – methanol solution after polishing. Nevertheless, if bromine is presented in XPS spectrum, we would expect a strong signal from peak at 182 eV, which comes from the Br 3p core. I attribute this peak as a satellite peak. Satellite peaks are results of an incomplete monochromatization of generated X-rays on quartz crystal, which results in minor resonance lines in the X-ray spectrum. Detected Cl should be just a residual from $AuCl_3$. The issue of Cl and its impact on M-S composition will be discussed in later text.

Recorded low concentration of of tin on the contact area (Sn) and silver (Ag) an copper (Cu) for the undegenerated sample are residual contaminations after sample contacting for previous experiments and are results of improper surface cleaning. Nevertheless, these impurities were removed after the first sputtering step. At binding

energies higher than 900 eV, one can notice the O KLL, Cd MNN and Ag MNN peaks. These peaks are related to ejection of electron by different mechanism, Auger effect. Highlighted elements from Fig 5.7 and Fig. 5.8 will be subjects of the detail scans.

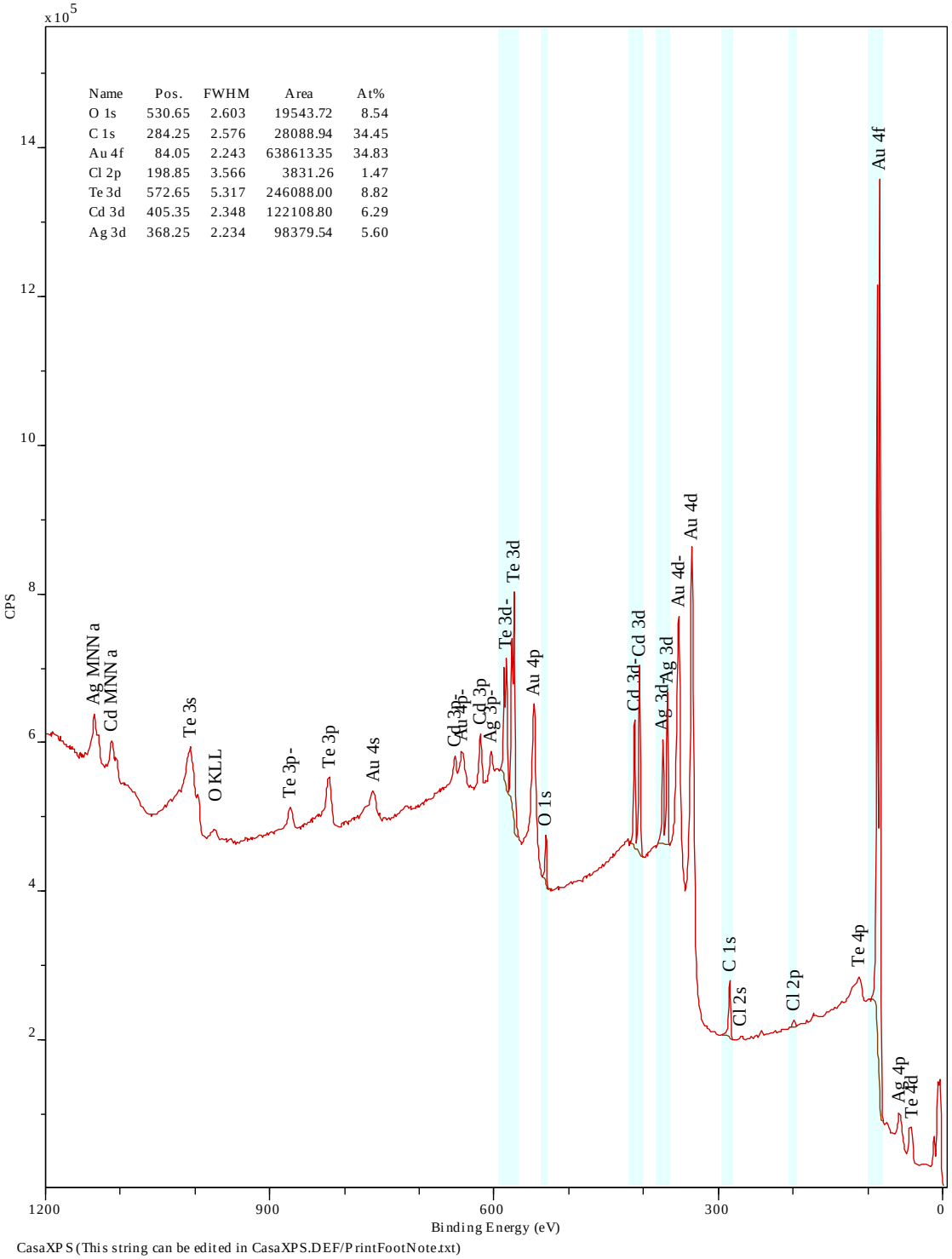

Figure 5.7:Survey (wide) XPS spectrum of the unstressed sample.

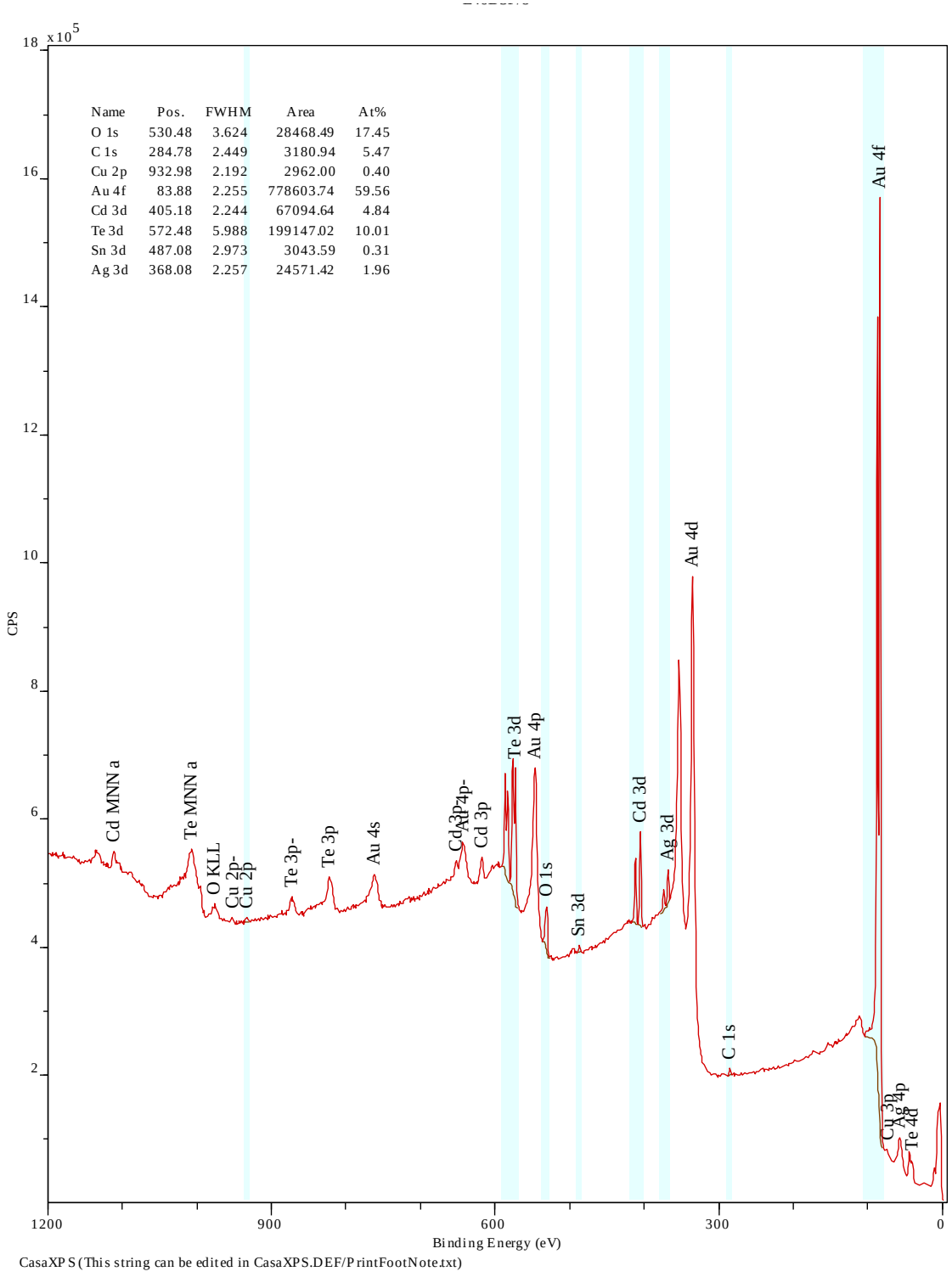

Figure 5.8:Survey (wide) XPS spectrum of the stressed sample.

5.3.1.3 Analysis of the detail XPS scans

After retrieval of survey (wide) spectra, photopeaks of interest were precisely scanned with aim to evaluate oxidation state of each element or its possible chemical bonding to another compound. In interpretation of XPS spectra analysis, existence of any extra bonding results into photopeak deviation from Gaussian shape to non-symmetric peak and at high concentrations of, for example oxidised states of investigated element, to its division into separate peaks.

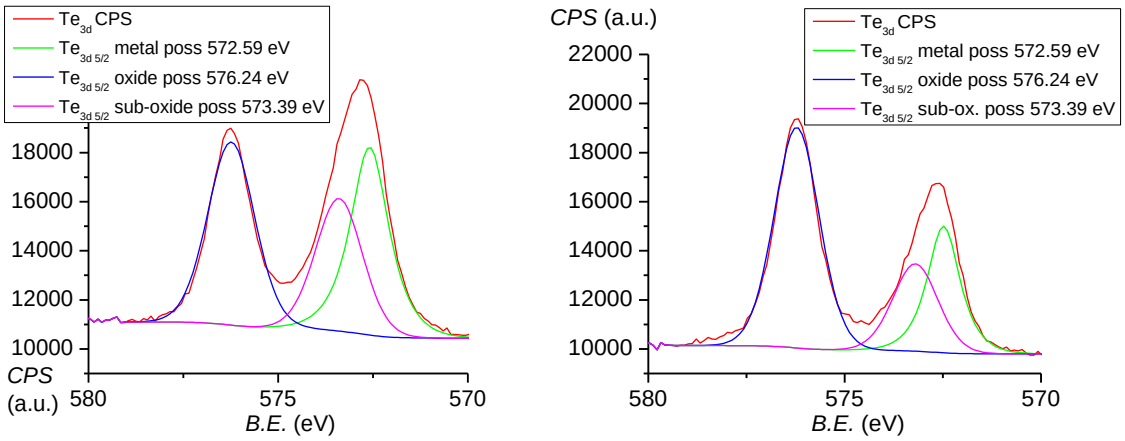

Figure 5.9:The detail scan of the Te 3d 5/2 photoemission peak. The spectrum of the unstressed sample is on the left.

Fig. 5.9 shows the detailed spectra of Te 3d 5/2 photoemission peak of analyzed samples. The red line denotes measured spectrum. Blue, green and violet lines are components representing chemical states of analyzed element. Beside dominant Te 3d peak of energy position of approx. 572.6 eV representing metallic form of tellurium, the detailed scan showed presence of a very clear chemically shifted higher energy peaks (Te 3d 5/2 Metal +3,5 eV). These are due to existence of the Te^{4+} state. with binding energy 576.2 eV for both samples, which was identified as a Telluride dioxide – TeO_2. Another peak that caused broadening of the metallic peak, located at energy 573.4 eV is Tellurium sub-oxide. Generally, sub-oxides are a class of oxides wherein the electropositive element or a radical is in excess relative to the "normal" oxides [44]. When the electropositive element is a metal, the compounds are sometimes referred to as metal-rich. Sub-oxides typically feature extensive bonding between the electropositive elements, often leading to clusters.

As one can see, the analysis of Te photopeak showed the same elemental and compound content for both stressed and unstressed detectors. The key difference lies in various content of each detected tellurium phase. After subtracting the background, including pertinent neighbor peak overlap of each fractional pohotopeak, photopeak area is calculated by its integration. Taking into account relative sensitivity factor (RSF) of each doublet pair / singlet of investigated element, proposed by Wagner and Moulder [45]. In order to obtain even more precise results, the values of RSF, related to the used instrument Kratos Ultra DLD, were taken from [42]. The atomic concentration is calculated as shown in following example for bimetal compound: For element A (A= peak area of A/Sensitivity factor of A). The same procedure is applied on element B. then,

% of A in bimetal A+B can be calculated as %A= A*100/(A+B). For the case of element B, calculation is made by formula %B= B*100/(A+B).

After retrieval of the "real" atomic concentration fractions of each chemical samples are easily received from as a fraction of the total area of the photopeak. Obtained values of concentration of each tellurium stages are summed in Table 4.

Table 4: Concentrations of Te chemical states measured without sputtering

	Stresed sample			Unstressed sample		
Te stage	**area**	**% area**	**at %**	**area**	**% area**	**at %**
Te Metal	6042.42	24.75	2.48	10920.12	34.98	1.70
Te Oxide	43123.31	53.94	5.94	11749.27	37.77	1.82
Te Sub- oxide	5199.75	21.31	2.13	8502.87	27.26	1.32

From the table above it is apparent that in the case of the stressed sample, the metallic form of Te is substituted by its oxide. The difference of concentration of TeO_2 between stressed sample and unstressed sample has highest influence on metal-semiconductor interface. Apart from conductive metallic Te, TeO_2 is a degenerative semiconductor with wide band gap 2.2 eV and high specific resistivity of approx. 10^{12} Ωcm [46]. Reader might this confusing since increase of TeO_2 should strength rectification effect of the Au / CdTe barrier, but the key difference will be explained in later text.

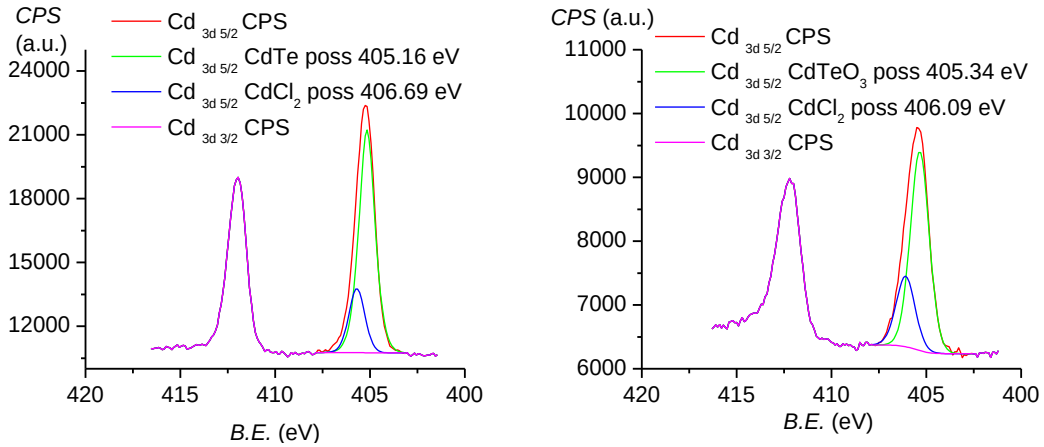

Figure 5.10:The detail scans of the Cd 3d photoemission peak. The spectrum of the unstressed sample is on the left.

Figure 5.10 shows expanded spectra of the Cd 3d photopeaks. Closer inspection of the spectrum shows that emission from some core levels (typically 3d and 4p) does not exhibit only a single photoemission peak, but a closely spaced doublet. The 3d photoemission is split between two peaks, one at 405.1 eV and the other at 411.78 eV, with intensity ratio of 3:2. This arises from spin-orbit coupling effects in the final state. The inner core electronic configuration of the initial state of the Cd is:[47].

$$1s^2 2s^2 2p^6 3s^2 3p^6 4s^2 3d^{10} 4p^6 4d^{10}. \quad (75)$$

The photoionization process of the 3d sub-shell with subsequent removal of an electron changes electron configuration of the sub-shell from $3d^{10}$ to $3d^9$ configuration of the final stage. Because of non-zero orbital angular momentum (for *d* orbital $l = 2$), coupling appears between the unpaired spin and the angular orbital momenta. One of the most commonly used approximation to determine coupling of the electronic state of the element [48]. Taking into account the ionized Cd, the $3d^9$ yields to two states and each of the states has different energy.

Considering **S** as the resultant spin quantum number for a system of electrons, which is the sum of individual spin quantum numbers for the separate electrons and the orbital angular momentum **L** defines the energy state for a system of electrons, vector sum of ***l*** and **S** is the total angular momentum **J**. The Russel term is given by formula

$$^{(2\mathbf{S}+1)}\mathbf{L} \tag{76}$$

and gives the ground term 2D [48]. The two states coupling for $\mathbf{L} = 2$ and $\boldsymbol{S} = 1/2$ vectors to give permitted states values of *j* as a total quantum momentum number,

$$2D\ 5/2\ g\ j = 2 \times \{5/2\} + 1 = 6,$$

$$2D\ 3/2\ g\ j = 2 \times \{3/2\} + 1 = 4.$$

The values of ***L*** and ***S*** must be combined from the total angular momentum values of 3/2 and 5/2. The lower energy final state of the photoionization is the one with maximum $j = 5/2$, hence this gives rise to the "lower binding energy" peak. The relative intensities of the two again gives permitted *j* values of 3/2 and 5/2 with the latter being lower in energy. The peak area ratio between coupled peaks is 2:3.

The difference of Cd photoemission spectra between stressed and unstressed detector is in term of atomic concentration negligible. Namely atomic concentration of Cd, which was 6.29 at% for unstressed and 4.65 at% for the stressed sample. I assume this difference rather to presence of scratches of Au layer rather than result of thermal stress. Both samples showed presence of $CdCl_2$ in the stressed sample. This caused clear Cd 3d peak shift towards higher binding energies and the concentration of detected Cd bonded to Cl_2 was 21.6 percent of overall atomic concentration of Cd for the fresh sample and 73.8 percent for the stressed sample. Existence of $CdCl_2$ can point to presence of voids in M-S interface, which were filled by not completely died out aqueous solution of $AuCl_3$, whilst solid metal layer was already formed. From the first XPS scan, I do not attribute this to a consequence of thermal stress of the sample, but as a result of improper contact deposition. The answer if this assumption is correct in later text.

Analysis of Cd and its oxide forms from C 3d core level is very difficult due to very low chemical peak shift (binding energy change) of oxidized Cd, which most often forms $CdTeO_3$ and these peaks cannot be resolved clearly. When Cd oxidizes to form $CdTeO_3$, there is no change in its chemical state and only line width broadening, which covers slight chemical shift of Cd binding energy caused by its oxidation. Efforts to quantitative description of the effects of amorphous oxides, such as $CdTeO_x$, Al_2O_3 and TiO_2 on core level shifts are published in [49]. This interpretation cannot be used because of non-stoichiometry of the M-S interface on semiconductor side (typically Te-rich structure,

depleted from Cd and with presumably low concentration of oxidized Cd). Moreover, $CdTeO_3$ was proposed as the most stable phase among several other oxide phases predicted based on the equilibrium phase diagram of the Cd–Te–O system [50]. Analysis of the detail scans of the Cd (LMM) Auger spectra published in [51] showed that there was no evidence of any shift to lower kinetic energy by 1 eV as observed for CdO. Hence it may be inferred that there is no evidence of the formation of any Cd oxide on the surface. From survey spectra of both investigated detectors in areas of energies higher than 1000 eV (Figs 5.7 and 5.8) a lower intensity of Cd (LMM) auger peak for thermally stressed detector can be seen in Fig. 5.8. However, the Cd (LMM) peaks were not subject of the detail scans. On the other hand, the detailed scans of Cd 3d core line yields the same information with better contrast to background.

Figure 5.11 shows the detail scans of oxygen. From the first sight, one can see that scanned O 1s peak does not split into spin-orbit components, but only a singlet appeal in the spectrum. As mentioned above, the total angular momentum quantum number ***J*** is given as a sum of the orbit angular momentum quantum number ***L*** and the spin angular momentum quantum number *S*. Since $l = 0$ for the *s* core shell, no coupling appeal and the whole energy is concentrated in a single photopeak.

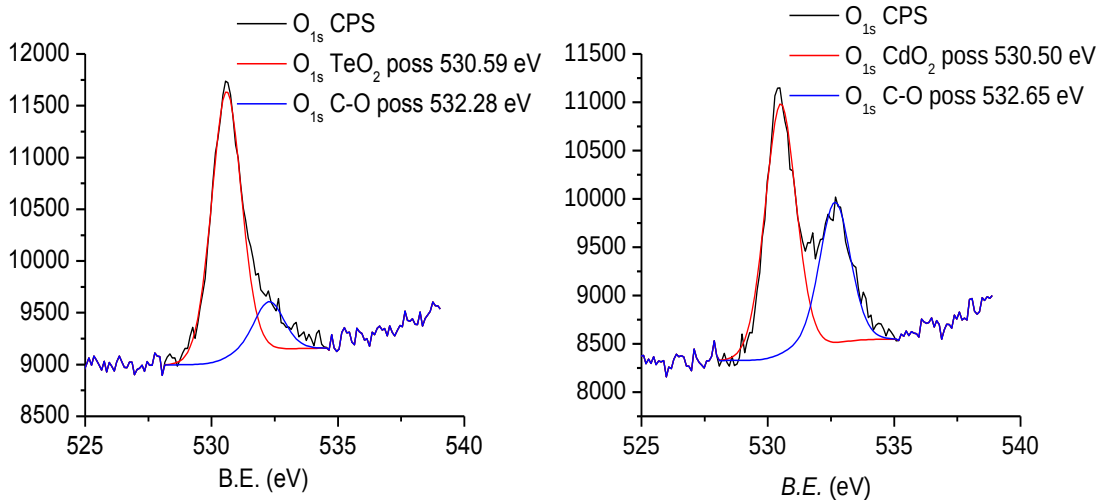

Figure 5.11: Detailed scans around binding energy of oxygen on surface Au-CdTe interfacial structure. Spectrum for thermally stressed sample are on the right, the ustressed sample is on the left.

Oxygen present within the interface of electroless contacts has generally been found to be in the form of oxide, with an O1s binding energy of ~530.5 eV. The presence of Oxygen may be due to its incorporation in grain boundaries. SEM micrograph of sputtered structure shown in Fig 5.12 of the stressed sample confirms presence of such grain boundary. Vertical line on secondary electron image on the left side presents mechanical scratch, which was not detected by screen capture in backscattered mode. Optically, the grain boundary seemed shallower than the mechanical scratch. This difference comes from electron emission depth from scanned area, which is significantly deeper for backscattered electrons image. Thus, shallow mechanical scratch cannot be seen in the BSE image.

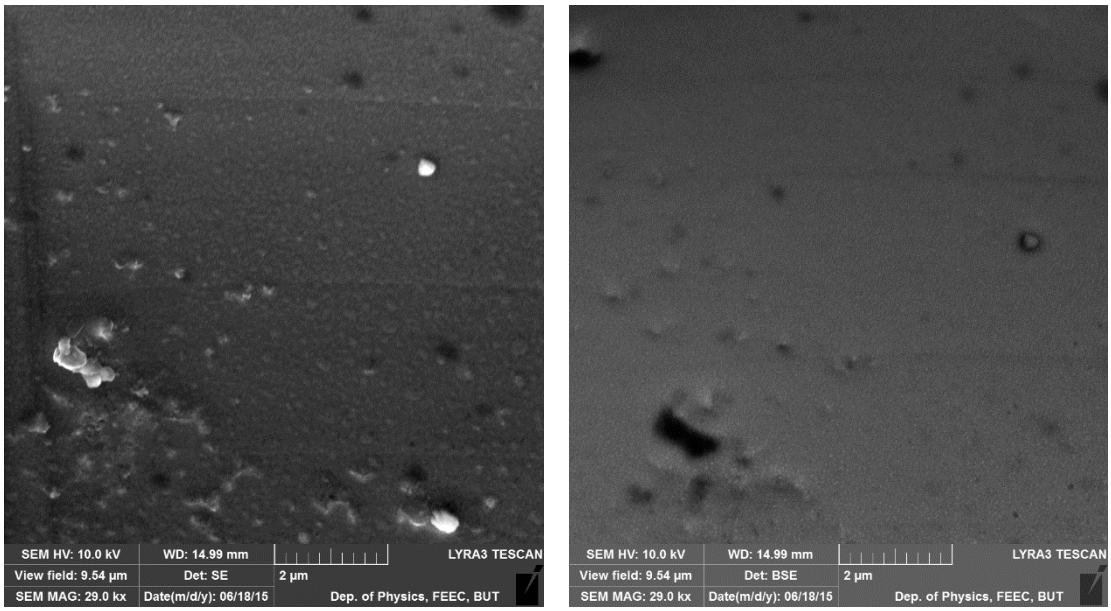

Figure 5.12: Secondary (left) and backscattered (right) emission micrographs of unstressed detector after gold layer removal by argon sputtering. Horizontal lines denote existence of grain boundaries in the detector bulk. SE and BSE are slightly shifted due to charging effect of semi-insulating CdTe.

Sometimes, the O 1s peak is more generally resolved into two peaks: one peak with a lower binding energy (between those of CdO and Te oxides) ions with the formal valence state O_2, the other higher binding energy component located at 532.3–532.5 eV attributed to the presence of loosely bound oxygen on the surface of the film such as CO_3 [50]. Therefore, the presence of C 1s could not be only a result of surface contamination, but possible explanation is desorption of C during surface oxidation of CdTe assisted with carbon oxides.

Variation of the C-O peak position is caused by different nature of C desorption, which is influenced by higher operating temperature, which was applied for thermally stressed detector. Similar findings were concluded during driven oxidation of CdTe surface in UHV system by molecular oxygen in [52]: The amount of oxygen adsorbed on the surface grows remarkably with further increase of gas exposure. If the ratio between carbon atoms and oxygen atoms per unit area is significantly higher than 1, the adsorption of intact molecules is not observed as adsorption of carbon compounds (like CO) but separate atoms of C and O. The ratio between compound adsorption and separate atoms adsorption results in widespread of the photoemission peaks energies.

Another interpretation of the O 1s photopeak split / broadening is given in [53]. O 1s peak is broadened by a significant shoulder-peak at a binding energy 532.3 eV. The split is related to higher concentration of OH^- / H_2O within the within the interface (I must remind that the contacts are deposited from aqueous solution of $AuCl_3$). Binding energy of OH - species is typically ~ 1.5 eV higher than the oxide binding energy. The H_2O binding energy is in turn ~ 1.5 eV higher than the OH peak. It was not possible to resolve the two peaks within the shoulder-peak so only a single, combined OH^- / H_2O peak has been fitted and quantified. It is proposed that $OH^- /H\ 2\ O$ was incorporated in a subsurface region of damage. This interpretation can be explained as a result of the

effect of air humidity on M-S structure. Furthermore, increased concentration of $Cd(OH)_2$ leads to higher leakage current of material, enhances recombination and thus reduce detector performance [54].

From obtained data, I cannot distinguish the exact origin of ~ 532 eV photoemission peak in O 1s spectrum. This peak is can be assigned to hydroxide and carbonate species. Both suggested options can take place simultaneously and are effect of ambient environment. Separation of each effect is also very difficult since carbon monoxide is probably the second dominant component (after molecular hydrogen) of the residual atmosphere in stainless UHV system. Similarly, application of moisture in well controlled environment without presence of carbon gases is nearly impossible. Comparing spectra of both samples, the degenerated sample showed slightly lower intensity of the peak and this can be result of desorption of carbon, activated by thermal stressing. Surface scan of the O1s photopeak showed no distinguishing feature caused by thermal stress.

In Fig. 5.13 are plotted photoemission spectra of the gold Au 4f photopeak. For both investigated samples, no binding energy shift from metallic reference. Measured binding energy of Au 4d 7/2 peak for the sample fresh was 84.0 eV and 84.07 eV for the stressed sample. The ratio of areas between each spin-orbit components is exactly 4:3, which unstrengthens my conclusion that no intermetallic or oxide forms were found on gold layer surface and longtime heat stress has no influence on gold. Furthermore, only a negligible photopeak broadenings within measurement error was recorded. Even if gold oxidized during heat stressing, the gold oxide state is unstable and formed oxide has tendency to decompose immediately after its formation and Au tends to return to ist purely metallic form [55].

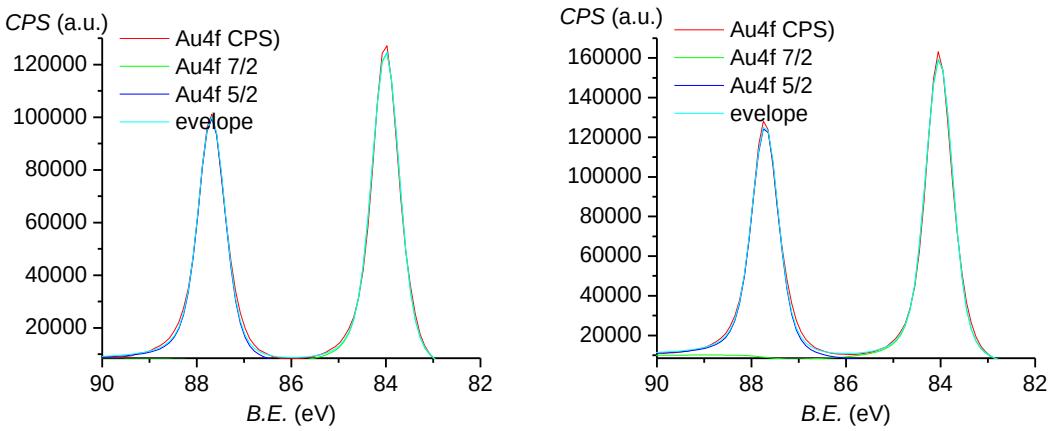

Figure 5.13: Detailed scans around binding energy of oxygen on surface Au-CdTe interfacial structure. Spectrum for thermally stressed sample are on the right, non-stressed sample is on the left.

Typical morphologic feature of oxidized gold and after its reconstruction is notable change of its restructuring. SEM image of gold oxidized at 100°C is shown in Fig. 5.14. Ridges in the gold foil only in areas that were exposed to oxygen (region B). On the left side, where the surface was covered by the sample holder lid, no ridges are observed.

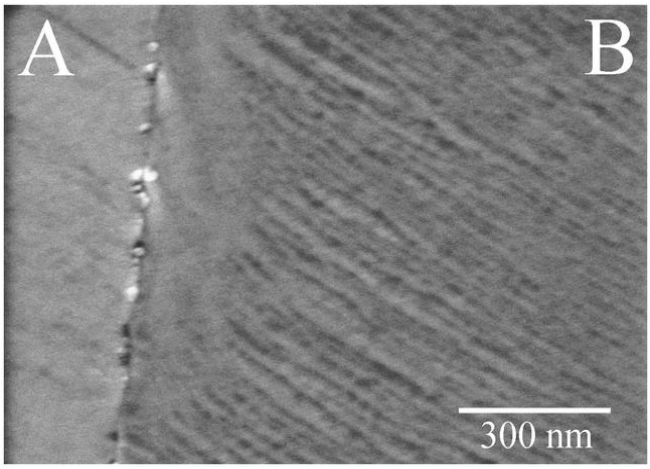

Figure 5.14:SEM image of gold surface exposed to molecular oxygen (B) and a part covered from exposition to oxygen (A). Image taken from [55].

The possibility of such a structural change was not part of our experiment since XPS spectral data were not acquired during the sample heat stress. Nevertheless, process of reversible oxidation described in [55] might have impact on electrical quantities of the M-S interface of the detector system.

5.3.2 XPS depth profiling of the M-S structure

Depth profiling at each sputtering steps consists of two actions after application of desired ion dose: i) Wide XPS spectra of M-S interface as are shown in Fig. 5.15 (unstressed sample) and in 5.16 (thermally stressed sample). For sake of readiness. The spectra are vertically shifted. After retrieval of wide spectrum, ii) the detail scans at areas of binding energies of elements of interest are conducted. Table 5 shows the relation between sputtering step order, sputtering time and ion fluence corresponding to sputter time.

Table 5: Sputtering parameters for XPS depth profiling

Sputtering step	Sputtering time (s)	ion fluence (ions/cm2)
1	30	2.7E+15
2	60	5.4E+15
3	90	8.1E+15
4	120	1.08E+16
5	150	1.35E+16
6	180	1.62E+16
7	240	2.16E+16
8	300	2.7E+16
9	360	3.24E+16
10	420	3.78E+16
11	600	5.4E+16
12	1200	1.08E+17
13	1800	1.62E+17
14	2400	2.16E+17
15	3000	2.7E+17
16	3600	3.24E+17
17	4200	3.78E+17
18	4800	4.32E+17
19	5400	4.86E+17
20	6000	5.4E+17
21	6600	5.94E+17
22	7200	6.48E+17

Sputtering was done by the Ar^+ ion gun irradiation with energy of 4 keV. The ion beam current density was 4 μA / cm^2. Accidental angle between the ion beam and the sample was 40°, given by the default detector arrangement of the Kratos system.

5.3.2.1 Analysis of wide scans of XPS depth profile

For both cases, after the first sputtering step, the C 1s photopeak disappeared from the spectra. From less sensitive wide scan of the spectra, I conclude that the presence of carbon is related to the surface contamination only, not to the diffusion of carbon into the M-S interface. Similar situation appeared with the presence of Cl_2 of the unstressed sample. The first dose was satisfactory to remove the loosely bonded surface contaminants based on organics and residuals after etching / chemical deposition.

Comparing wide spectra of both samples, one can see two main differences between them: i) Higher peak for O 1s and its existence at high sputtering times and ii) different Te x Cd doublet ratios. No “new” chemical element appeared during sputtering. Resulting elemental depth profile and further discussion is in following two chapters.

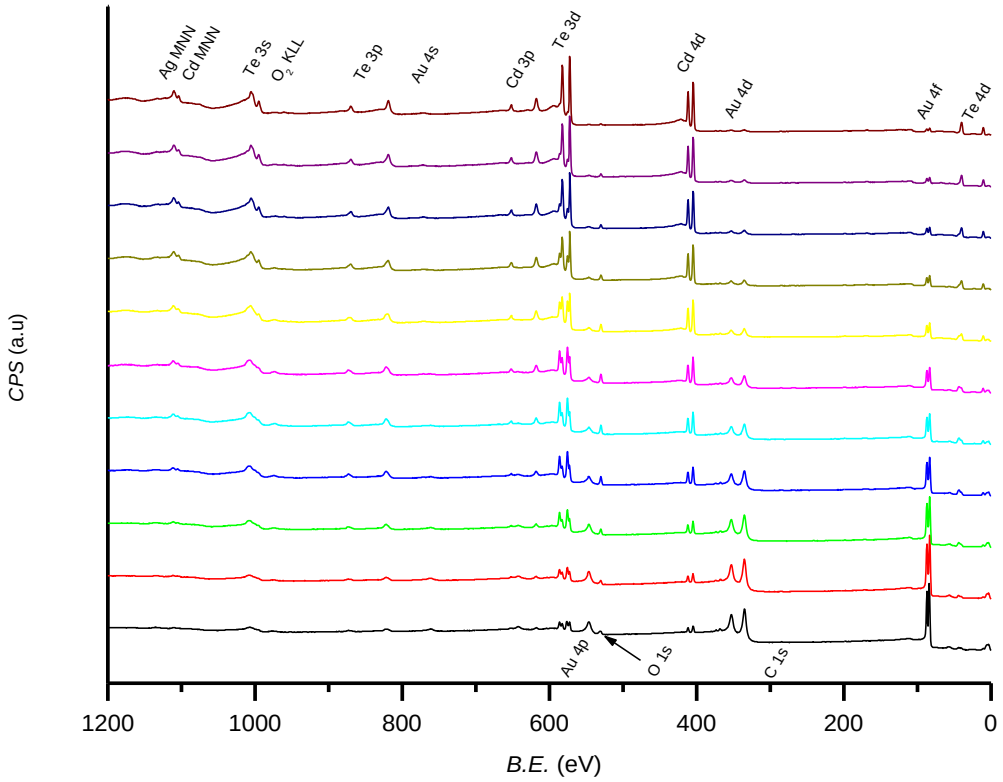

Figure 5.15: Survey XPS spectra during depth profiling of the unstressed sample.

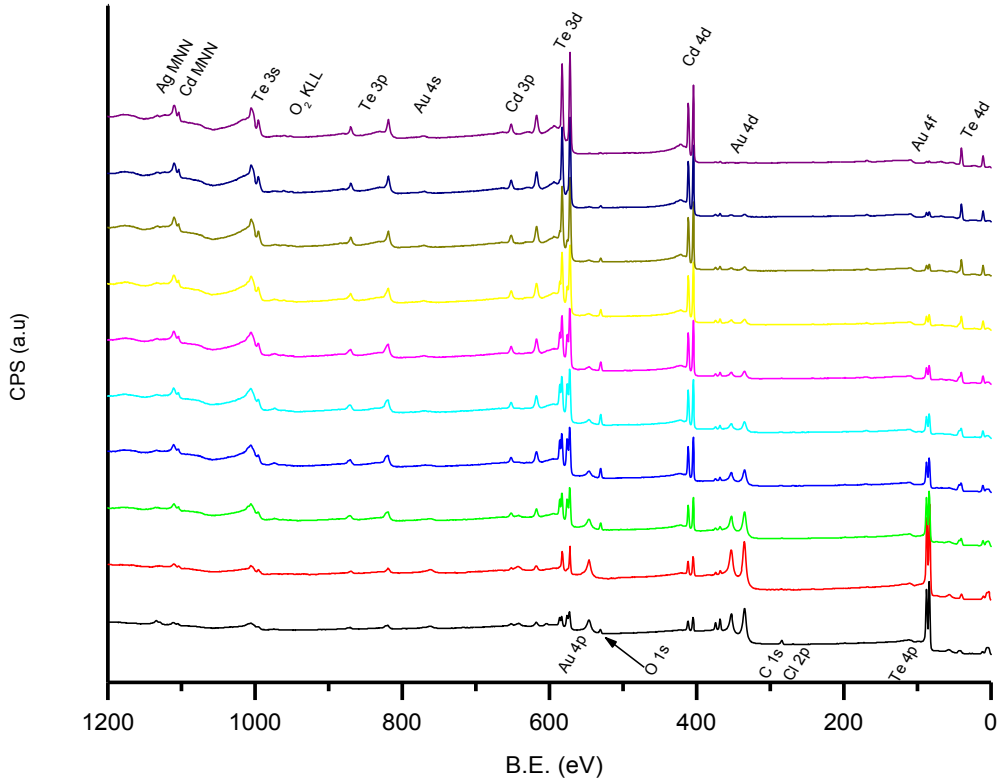

Figure 5.16:Survey XPS spectra during depth profiling of the stressed sample.

5.3.2.2 Analysis of detail scans of XPS depth profile

The O1s peak of the XPS spectra of the stressed sample was presented up to the 11th sputtering step, equal to dose of 5.4E+16 ions / cm2. The O1S photopeak for the case of unstressed sample was present only up to 9th sputter step (3.24E+16 ions / cm2).

The stressed sample shows more significant split of the peak towards higher binding energies. This is related to the C-O bond and shows some diffusion of C into the M-S surface. As shown in Fig. 5.16, the first dose already has sputtering / surface removal effect. In all other cases, the presence of oxygen is linked with Te in form of TeO_2 and it disappears simultaneously with the sub-peak of Te3d at binding energy of 567 eV for Te3d 5/2 in Fig 5.20. For the case of stressed sample, the shift of the main peak is caused by binding of oxygen to CdTe in form of $CdTeO_3$.

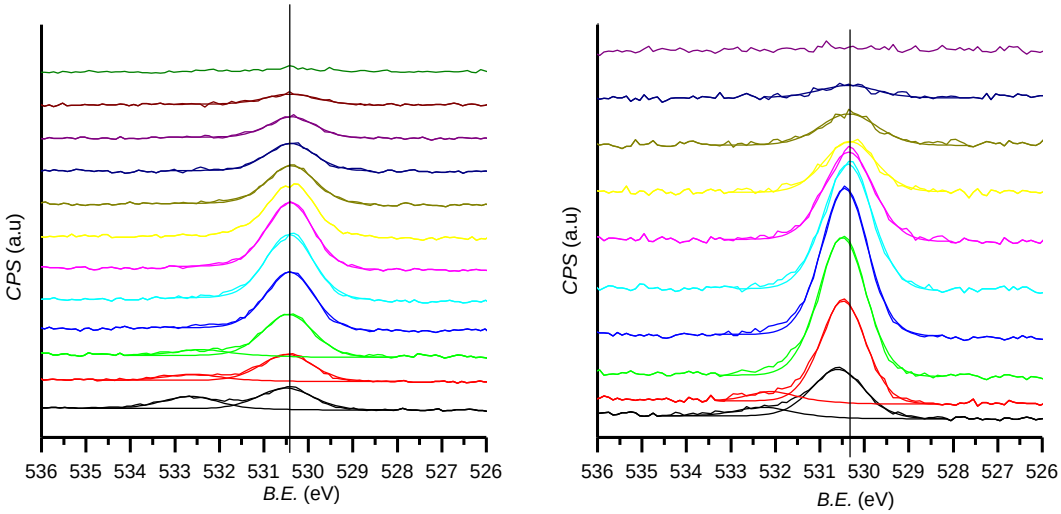

Figure 5.17:The depth profile of the detail scans of the O 1s photoemission peak. The spectrum of the unstressed sample is on the left.

In Fig 5.18, the detailed spectra of Cd are shown. Apparent chemical shifts of photoemission peaks take place only for unsputered samples. This situation is already explained text related to Fig. 5.10. Comparison with spectra acquired deeper in the M-S interface shows that the fresh sample shows less significant chemical shift of Cd for unsputtered state than the stressed one. I conclude that highly concentrated unwanted Cd compounds in M-S surface, $CdTeO_3$ and $CdCl_2$ are presented as a nearly monolayer thickness just at the interface between the crystal and Cd. As written above, it is extremely difficult to estimate the exact chemical state of Cd by the most used method: from the photoemission peak fitting. In study on pristine CdTe [51], no binding energy shifts of Cd 3d photoemission peaks were reported as a result of XPS depth profile.

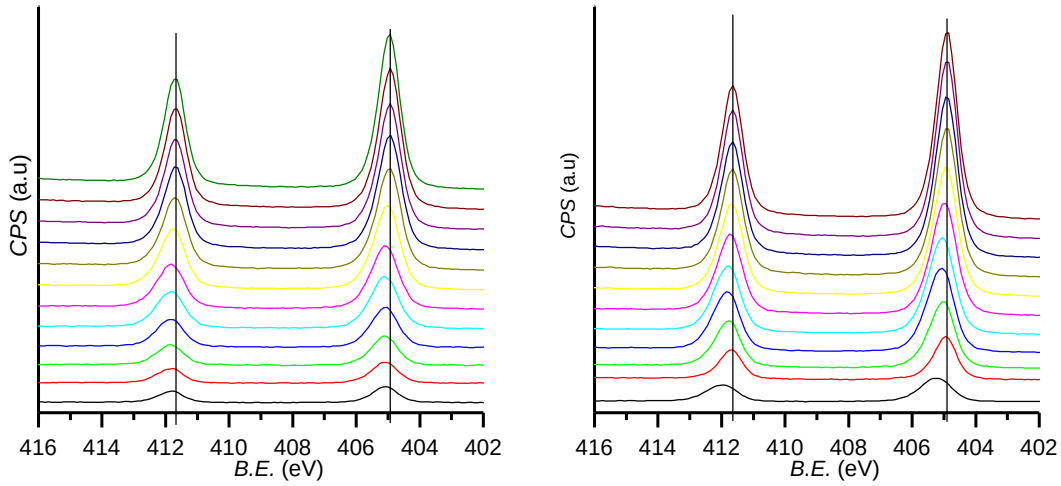

Figure 5.18:Depth profile of the detail scans of the Cd 3d photoemission peak. The spectrum of the unstressed sample is on the left.

To analyse such small chemical shifts (binding energy variances are below 0.2 eV) I used different, less common method: Comparison of Cd 3d photoemission peaks possitions with atomic concentrations of sub-oxide chemical states of Te and atomic concentration of Cl in M-S interface of both samples. This relation is depicted in Fig. 5.19.

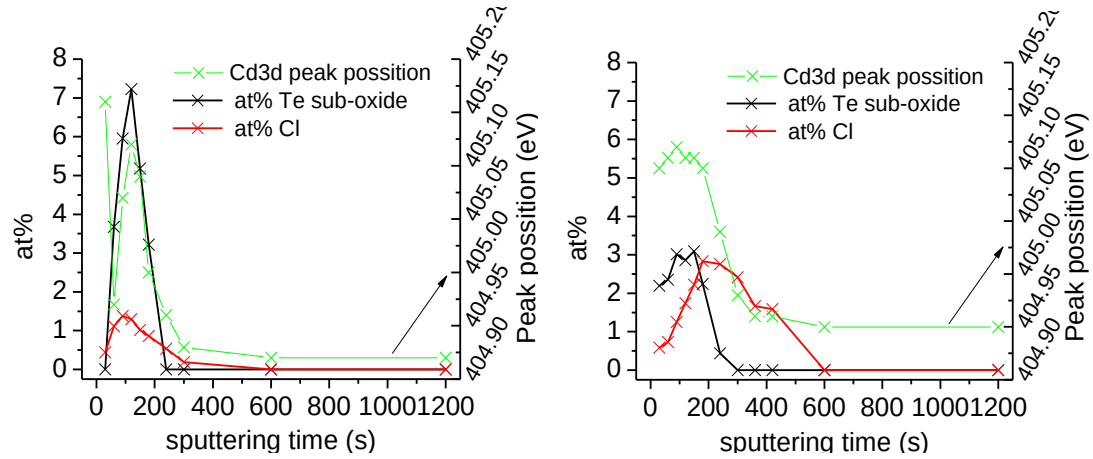

Figure 5.19:Comparison of chemical shifts of the Cd 3d photoemission peaks with the atomic content of Cl and Te sub-oxide. The unstressed sample is on the left.

Figure 5.19 clearly justifies the existence of sub-oxide form of Te and the origin of binding energy shift of Cd, which is closely linked with existence of Cl, dissociated from $AuCl_3$. The reaction of $AuCl_3$ with the CdTe surface is described by the formula

$$4AuCl_3 + 6CdTe \rightarrow 4Au + 12Cl^- + 6Cd^{2+} + 6Te. \qquad (77)$$

Onwards, Cl reacts to cadmium chloride ($CdCl_2$ with binding energy 406.1 eV) with concentration below detection threshold of the XPS system, i.e. concentration $< 10^{19}$ cm^3 (considering the atomic density of CdTe of approx. 10^{22} atoms / cm^3). Even though $CdCl_2$ is not clearly detected by XPS, a shift of the Cd 3d 5/2 peak towards higher binding energies can be observed. Te partially or segregates into pure metal during deposition or oxidize into TeO_2 delivered from the aqueous solution of $AuCl_3$, since $AuCl_3$ dissolved

in water forms $H[AuCl_3(OH)]$ [56]. For both Cd and Te, volume of $AuCl_3$, which is (approx. 10 nm × contact area) is much smaller than the volume of CdTe crystal. Furthermore, from eq. 77 can be clear that there is not enough oxygen for complete transformation of Te into TeO_2, leading to formation of the sub-oxide form of Te. Aqueous solution of $AuCl_3$ is initially neutral and decomposes gradually in time with separation of gold. Therefore, the $AuCl_3$ solution has ageing features and its actual chemical state has unneglectable influence on chemical composition of the M-S interface and reduces repeatability of of chemical / electrical parameters of the M-S interface.

Comparing depth profiles of the quantities depicted in Fig 5.19 for both samples, concentrations / Cd 3d photoemission peak positions are quite comprisable. Some distortion of distribution is visible for the stressed sample (Fig 5.19 right), showing less abrupt increase of concentration of sub oxide and $CdCl_2$. Constant binding energy shift approximately of 0.05 eV to higher energies, which is present for the Cd3d photopeak of the stressed detector among the whole scanning interval up to 7200 s (not shown), is a result of permanent deviation from stoichiometry (see Fig. 5.24). Higher atomic concentration of Cl and its unpredictable diffusion might be the reason of difficult reproducibility of contact deposition by aqueous solution of $AuCl_3$.

Fig. 5.20 shows the depth profiles of the Te 3d photoemission peaks of both samples.

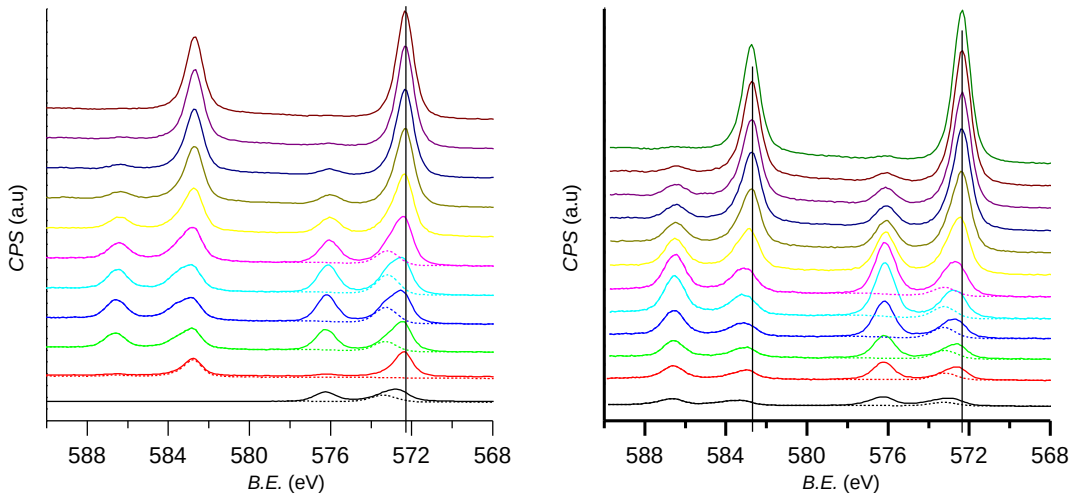

Figure 5.20: Depth profile of the detail scans of the Te 3d photoemission peak. The spectrum of the unstressed sample is on the left.

The Te 3d 5/2 peaks (the right pair in the pictures) are shifted to higher binding energies and have asymmetric shape and are shifted towards higher binding energies. The asymmetry and the value of the shift is related to the fraction of Te in its sub-oxide form and are depicted by broken lines in figures. For the unstressed sample, after 30 seconds of sputtering, Te was detected in its nearly clear metallic form. Only 6.6 percent of Te was oxidized into TeO_2 and no sub oxide form Te was found. At this this sputtering step, the plateau value Au concentration was found (70 %) and some 7 % C bonded to O (see

Fig. 5.17) contamination was present. Te had 10 % share on total atomic concentration and this closest layer to Au is not oxidized.

Similarly, for both samples, the asymmetry related to the Te sub-oxide disappears after the 6th sputtering step (300 s of sputtering). After this sputtering step, the Te 3d 5/2 photoemission peak position is for both samples constant at 572.34 ± 0.02 eV for the unstressed sample and 572.36 ± 0.03 eV for the thermally stressed one. These values are within measurement error of the used system. Different intensities of the Te 3d 5/2 photopeak are given by variation between of concentration of ratio Te and (TeO_2 + Te sub-oxide). For further analysis of the Te forms and their concentration, I re-plotted the depth profiles and the atomic percentages of each Te chemical state are enumerated in the following picture:

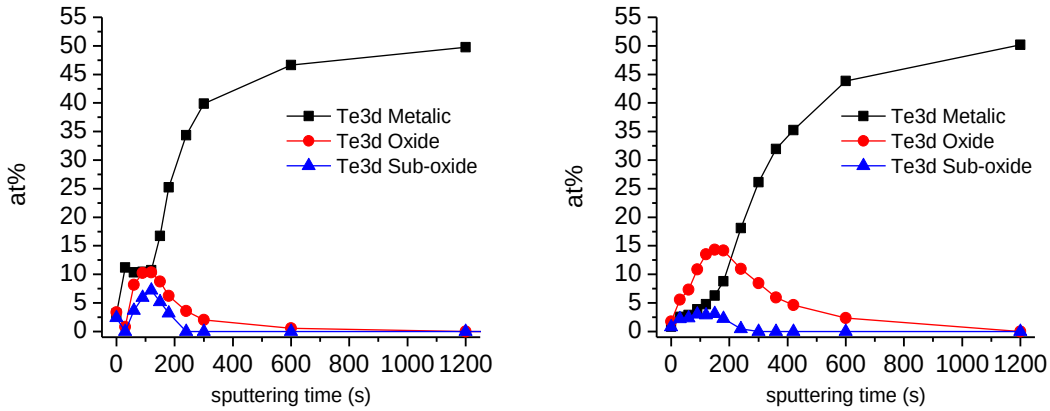

Figure 5.21:Depth profiles of atomic concentrations of Te in its metallic form, oxidized form and sub-oxide form. The unstressed sample is on the left.

Figure 5.21 further confirms conclusion that diffusion of Te sub- oxide as a result of thermal treatment is negligible. On the other hand, different situation occurs for the Te 3d peak in its TeO_2 form. The stressed sample shows the presence of TeO_2 remarkably deeper in the sample bulk. After 1200 s of sputtering, TeO_2 is still detected with atomic concentration of 0.45 %.

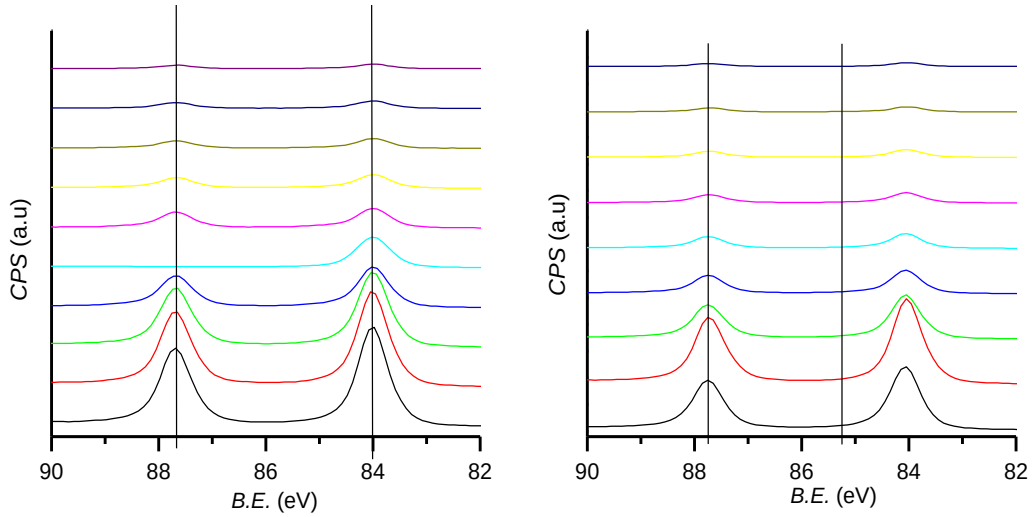

Figure 5.22: Depth profile of the detail scans of the Au 4f photoemission peak. The spectrum of the unstressed sample is on the left.

Figure 5.22 depicts the detail scans of the Au 4f doublets for both samples. I have conducted similar investigation as in the case of the Cd 3d photoemission peak, but no certain information come out from the analysis. There was no variation of the Au 4f 7/2 photopeak for the unstressed sample. Binding energy had a constant value of 84.00 eV. Thermally stressed sample showed variation of binding energies from 84.03 eV to 84.06 eV. Such small, 0.03 eV variation did not show any trend in depth profile of Au-Cdte interface. Published study [57] that deals with with chemical states of $AuCl_3$ shows that the presence of the Au^{3+} state leads to clear, nearly 3 eV binding energy shift towards higher binding energies. Furthermore, the presence of the ionic state of Au results in formation of a new sub-peak at 95.6 eV in the spectrum, similarly as it is for Te^{4+} (TeO_2) state of Te. Therefore, I can surely conclude that Au is present only in its purely metallic form and its chemical state is not influenced by increased temperature. Nevertheless, the evolution of atomic concentration with depth differs for each sample. This issue is discussed in paragraph below Fig. 5.23 and Fig. 5.24.

5.3.2.3 Elemental XPS depth profile

Figures 5.23 and 5.24 show depth profile of elemental composition of M-S interfaces for thermally stressed and unstressed detector. Reader might be looking for very useful information about the volume / thickness of the bulk removed by each sputter interval in these figures. During depth profiling, I did not evaluate sputter rate for each sputtering step. It was impossible to calculate sputter yield because its variation with elemental content of the structure. Furthermore, the Kratos spectrometer is not equipped with instrumentation that allows in-situ depth measurements, such as ellipsometer, optical inferometer or any other adequate instrumentation. Removal of investigated samples from UHV chamber, measurement of the crater depth / morphology followed by subsequent re-inserting of the samples to the samples holder might have negative effect on analysis results (oxidation, contamination by dust, different sample alignment etc.) and is time demanding – the UHV conditions in the system are reached after approx. 45 minutes after insertion of the samples into the load-lock chamber.

From comparison of figures 5.23 and 5.24 show apparent structural change caused by increased operating temperature of the semiconductor crystal. M-S interfaces of both samples were Te-rich. The non-stoichiometry for the case of unstressed detector shows was present up to 600 s of sputtering. Even more significant deviation from stoichiometry is remarkable for the stressed detector. For both samples, highest deviation of non-stoichiometry was measured after 120 s of sputtering. The stressed sample showed Te / Cd ratio 1.893, whereas the unstressed sample was Te rich with ratio of 1.310. In both cases, the maxima of non-stoichiometry are linked with the highest concentration of oxygen. Measured values of O atomic concentrations are 31.53 % (stressed sample) and 26.22 % (not stressed sample). Distinctive, more than 5% difference between oxygen in favour of the stressed sample points to adsorption of oxygen at higher temperatures.

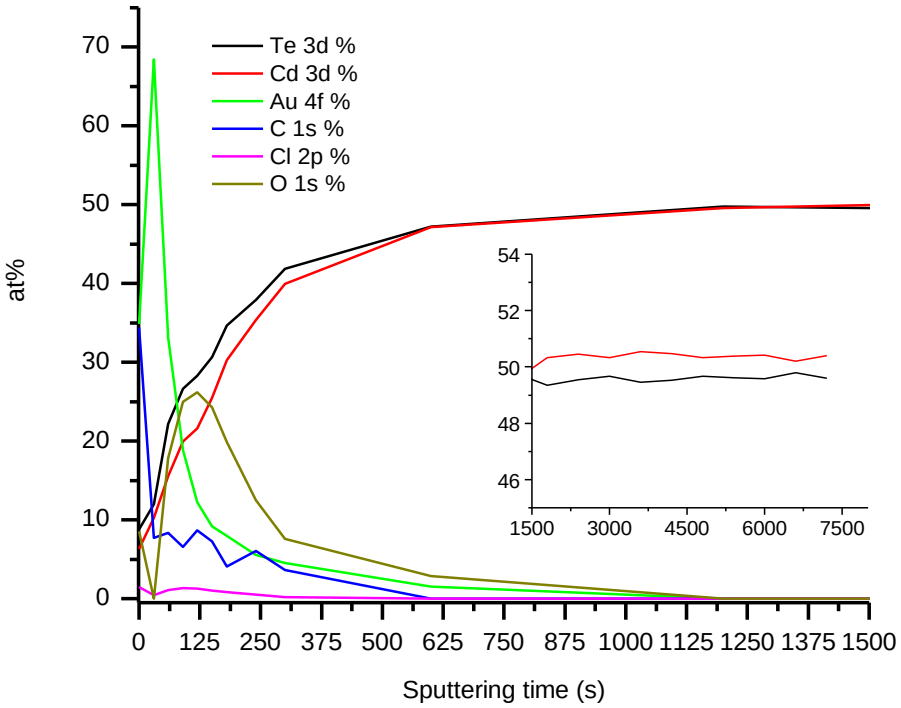

Figure 5.23:XPS depth profile of the M-S interface of the unstressed sample.

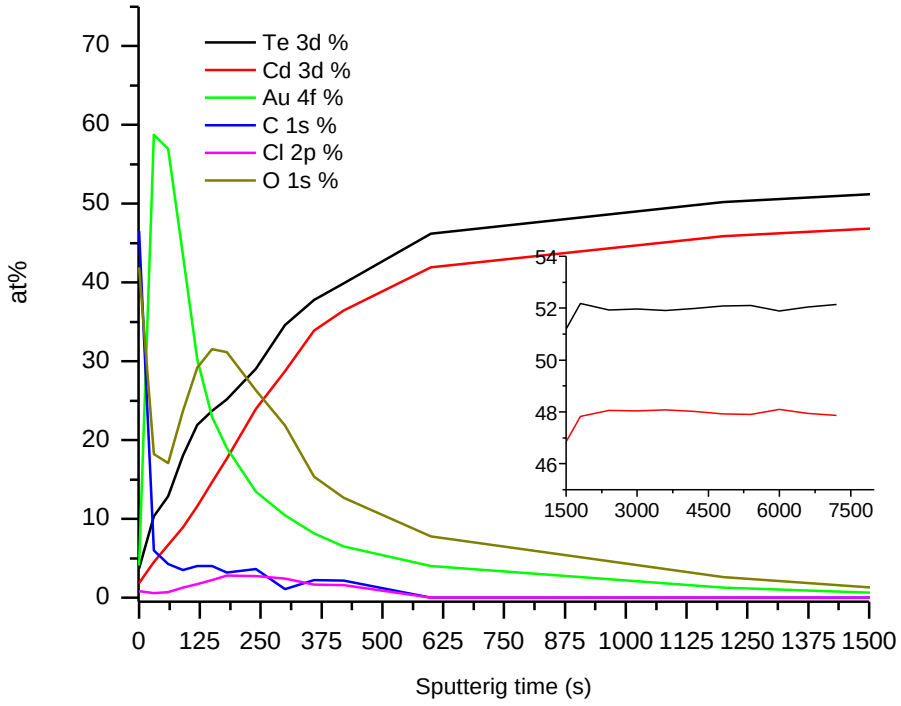

Figure 5.24:XPS depth profile of the M-S interface of the stressed sample.

Insets in the Fig. 5.23 and Fig.5.24 show Cd/Te atomic concentrations at higher sputtering times. The only detected elements by XPS were purely metallic Cd and Te. The unstressed sample show nearly stoichiometric ratio of Cd and Te deeper in the crystal bulk. The atomic concentration difference within 0.2 % can be attributed to measurement error of the used instrumentation. On the other hand, the stressed sample shows significant depletion of Cd in its volume. At all XPS scans at longer sputtering times, The Te/Cd ratio had constant value of 1.085. I can omit the effect of large (> 1 μm) Te inclusions since the sputtered area was large enough. From these apparent differences revealed by XPS, I can conclude that ambient temperature higher than 400 K cause release of Cd from the crystal structure and it is the main effect of irreversible change of the bulk properties as a consequence of thermal stress of the detector

Interesting feature caused by higher operating temperature is enhanced diffusion of Au into the detector bulk. In the case of the unstressed detector, the Au photoemission signal disappeared after 1200 s of sputtering, whereas gold signal was presented up to 1800 s for the case of stressed detector. Evolution of Au concentration decrease with depth was much steeper for unstressed sample than for the stressed one, put integration of both curves yield the same results. For both sample, the presence of oxygen, which is hand-in-hand with existence of TeO_2 in the structure is connected with presence of Au.

5.3.3 Secondary Mass Ion Spectroscopy depth profiling

Secondary Ion Mass Spectroscopy (SIMS) analytical method is based on analysis of the mass analysis of ions released from the structure by bombardment of the surface by a beam of primary ions. Typically, the ion energy is in interval 0.2 – 20 keV [58]. During bombardment, the sputtered particles carry information about studied surface. Most of sputtered atoms are in neutral state. Only approx. 1% of atoms are ionized. Analysis of these secondary ions by mass spectrometer is basis of SIMS. The key advantages of SIMS are:

- Extremely high sensitivity (up to parts per billion for systems with ion implantation)
- Ability of detection of all elements, including hydrogen, isotopes distinction
- High lateral resolution (~ 30 nm), possibility of elemental composition depth profiling with depth resolution 1 nm that is lower than XPS (~5 nm).
- Allows arrangement of 3D profiles (precipitates spatial distribution etc.)

Nevertheless, SIMS also suffer from some disadvantages:

- SIMS is destructive. This disallows us to conduct analysis at the same spot, e.g. after chemical modification of the surface
- Difficult data quantification. In some cases, it is extremely difficult to distinguish ions with comprisable mass.
- With increasing depth resolution of analysis, sensitivity decreases

- Problem with preferential sputtering. Some precipitates can have higher radiation hardness and are removed with lower sputter yield (ration between released particles per one incoming ion). To find suitable sputtering, many methods have to be tried out, such as sample rotation, sample cooling, cluster ion bombardment, choice of suitable primary ions.
- Crater effect. This phenomenon has similar feature like preferential sputtering. Secondary ions generated from walls of sputter crater degrade accuracy of depth profiling. Generally, this effect is reduced by use of large diameter of primary beam. If it is possible to deflect the primary beam, "gating" techniques that, only collect data when the beam is in the central flat part of the crater. There are two ways of gating: i) electronic and ii) optical. Simultaneous application of both methods yields the best depth resolution, bot for cost of signal lowering [59].

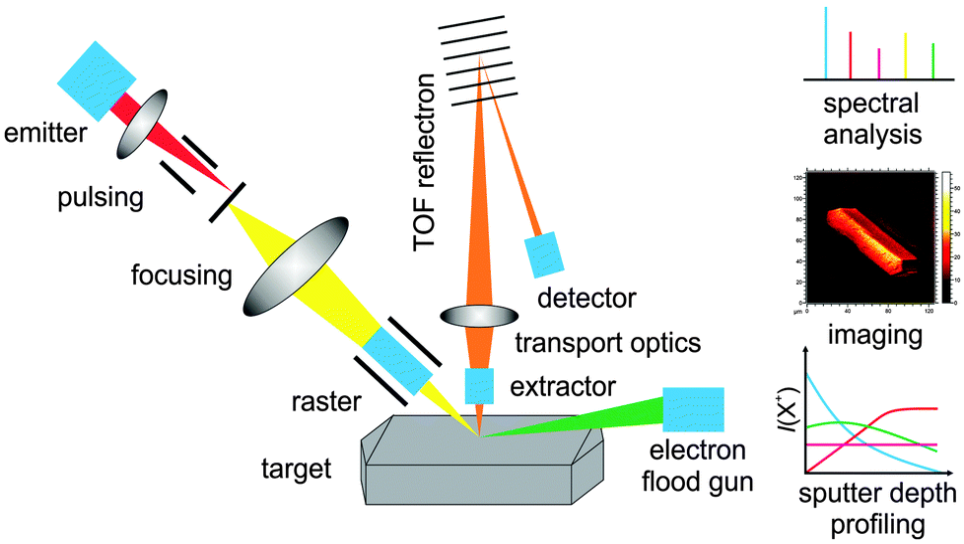

Figure 5.25:Typical schematics of the functional principle of a ToF-SIMS instrument and options for surface and bulk analysis of solid catalyst samples by (i) mass spectrometric analysis of surface borne secondary ions, (ii) imaging of the lateral distribution of secondary ions, and (iii) sputter depth profiling. Image taken from [60].

Primary ion source is used to ionize the surface. Three basic kinds of ion sources are used. i) ion guns passed on ionization of noble gasses (Ar+, Xe+…) by duoplasmatrons or electron ionization. This type of ion gun is easy to implement, produces high ion beam currents, but focusing abilities are limited. ii) 133Cs+ surface ionization gun. Ions are created by evaporation through tungsten grid. This type generates relatively high ion currents and the beam can be easily focused. iii) Liquid metal ion guns. This guns operate with metals with low melting points (Ga, Bi), which is evaporated by a sharp tungsten tip. Evaporated metal is accelerated by high electric field towards the target. This type of source produces very thin beams (tens of nm) and is able to operate in pulsed mode. Up-to-date systems are equipped with more primary ion guns, combination of type iii) and type ii) is the most common.

Mass analyser (ToF reflector, flight tube) is analytical part of the system. From variety of mass analysers suitable for SIMS, used used system was based on Time-of-Flight mass spectrometry, which is based on the fact that ions with the same energy but different masses travel with different velocities. An electrostatic field accelerates the generated ions to a common energy. The accelerated ions then travel over a drift path to the detector. The lighter ions fly with a higher velocity and arrive at the detector before the heavier ions. Measuring the flight time for each ion allows the determination of its mass. This cycle is repeated with a repetition rate of up to 50 kHz.[61] This type of mass spectrometry requires pulsed secondary ion generation using either a pulsed primary ion gun or a pulsed secondary ion. The key advantage is, apart from e.g. quadrupole detector is that it is the only analyser detecting all generated ions simultaneously.

Detector is the end unit of mass analyser. For high currents, the Faraday cap is used to measure secondary ions signal. Other detection techniques employ electron multiplier, when the impact ion creates a burst of 10^8 electrons on the output of multiplier. This pulse is directly recorded as an electric current pulse. Microchannel plate detector (grid of thin tubes, where each tube acts as an electron multiplier) has similar features like electron multiplier, but with the advantage of its position sensitivity. The used detector designed by Ion-Tof is combination of single plate detector- photomultiplier-scintillator.

For my analysis, measurements were done on the IonTof Sims5 spectrometer. As a primary gun, the Bi nanoprobe with ultimate lateral resolution of 50 nm was used. This gun emits clusters of Bi_3^{++} ions. The key advantages of clustering are lower preferential sputtering rates at lower local temperatures of irradiated areas. In spectroscopic mode, the sensitivity of the spectrometer is ~10^{12} atoms / cm^3. Resulting 3D elemental profiles are depicted in Fig. 5.26 (unstressed sample) and Fig. 5.27 (stressed sample).

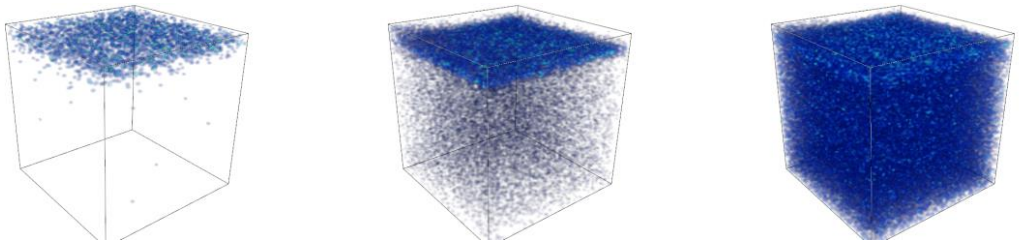

Figure 5.26: 3D ToF SIMS profiles of Au, Cd,Te, Cl, In and Na of the unstressed sample.

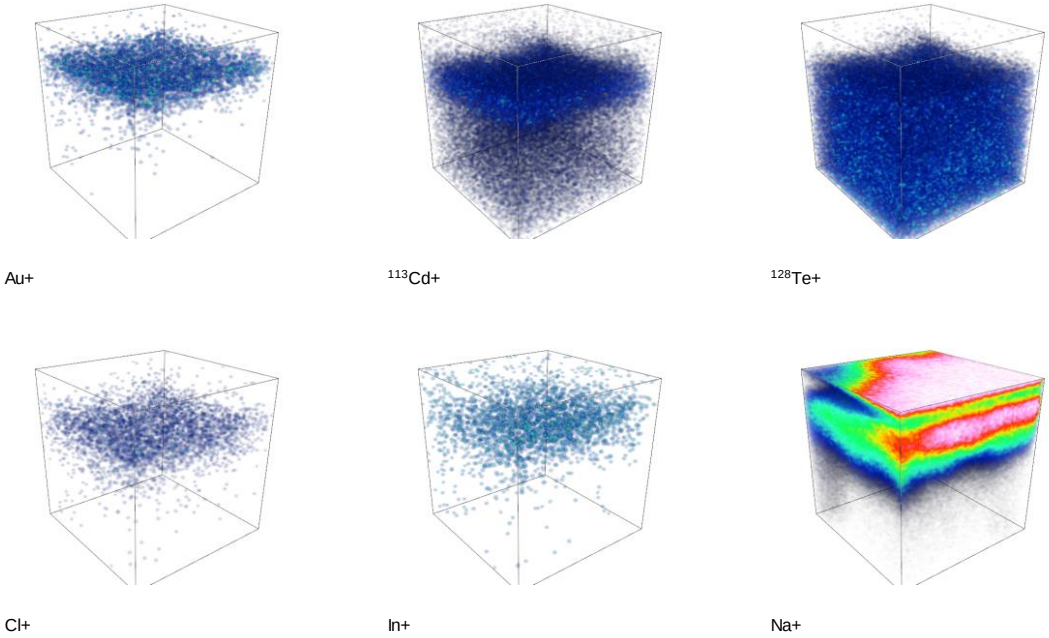

Figure 5.27: 3D ToF SIMS profiles of Au, Cd, Te, Cl, In and Na of the stressed sample.

More than 5 orders higher sensitivity allowed me to observe trace elements in the structure, such as dopant In and expected native impurity in CdTe – sodium. As like observed by XPS, Au shows significant diffusion into the bulk after thermal stressing. Similarly, Cl is diffused deeper into the bulk after stressing. Lower threshold detection limits of SIMS showed that Cl has the same spatial distribution as Au. This allowed me to more specify the results of XPS analysis: Even though Cl and O bonded to Cd cause in both cases chemical shift of the Cd 3p core level photoemission peak towards higher binding energies. Cd primarily reacts to $CdCl_2$. Oxygen is bonded to Te in TeO_2 and due to the lack of O, the sub-oxide form of Te appears.

Interesting was behavior of In as a donor that compensate cadmium vacancies V_{Cd} in CdTe. This feature is used to reach semi-insulating state of CdTe. For both samples, in the vicinity of Au, higher concentrations of In were detected. This phenomenon was even more enhanced in the case of the stressed sample. Depletion of In in the bulk leads to breach of compensation of V_{Cd}. Furthermore, Cd and In can react into conductive eutectic alloy with melting point 400 K [62].

Soudium was detected on the surface of both samples. Na is a frequent surface contaminant, but measurements on more spots always showed significantly higher intensities for Na in favor of the stressed sample. Both samples were stored at the same place ant were identically treated. As for other so far mentioned elements, the stressed

sample showed thicker layer of Na. In contrary with the unstressed sample, Na was found below the gold layer, not only on the surface.

From these I conclude that higher temperature squeezes out Na and In from the bulk towards the surface. This can be beneficial, if well controlled low temperature annealing will be performed with result of clear out Na from the crystal bulk. This procedure has to be controlled precisely in order not to break compensation.

Concentration of Cd showed different behavior than recorded by XPS. This might be the result of too high sputtering steps during profiling. Craters after profiling by SIMS were only 5 μm deep and 180 scans were done. Presence of Cd enriched layer is due to preferential formation of $CdCl_2$ during manufacturing. Furthermore, cluster sputtering has lower tendency to mill preferentially Cd at high ion doses. For the unstressed sample an increased concentration of Te is visible just below the Cd rich layer This situation is described in XPS analysis in the left panel of Fig. 5.21 as a result of existence of the thin layer of not oxidized Te. This area corresponds to the detail scan of the 2nd sputtering step in Fig. 5.20. This is not visible for the case of the stressed sample.

5.3.4 Morphological, SEM, AES and XRD study of craters after depth profiling

This chapter is focused on investigation of chemical states and morphology of areas of M-S interfaces of both investigated samples that were uncovered by material removal during sputtering. Study of crystallography of areas uncovered by sputtering is also conducted.

5.3.4.1 SEM and AES analysis

Disequilibrium of the Cd/Te ratio, structural changes in CdTe single crystal caused by heat stress have an effect on radiation hardness of the semiconductor bulk and this is reflected on surface morphology of the craters originated by argon sputtering. SEM micrographs of distinctively different surfaces after ion bombardment (ion dose was 6.48E+17 Ar^+ ions / cm^2) are shown in Fig 5.28.

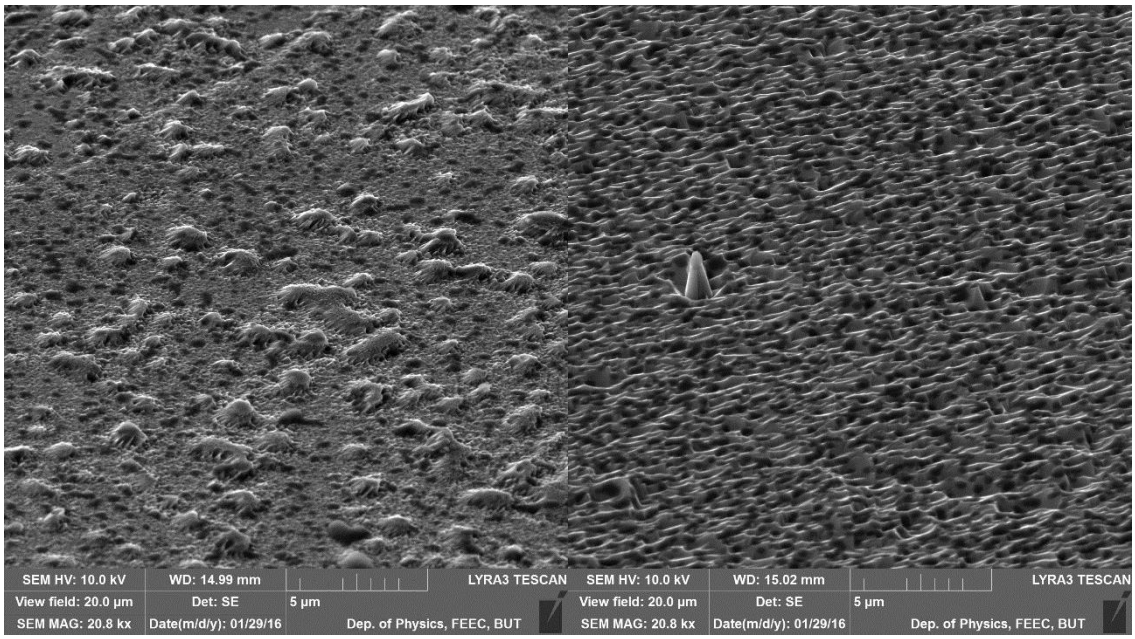

Figure 5.28: SEM micrographs of the surface after depth profiling. Unstressed sample is on the left.

One would expect the smoother, periodically arranged surface with typical ripple stricture of the crater belongs to the unstressed crystal. Surprisingly, situation is opposite. The ordered structure is the surface of the stressed crystal. The reason of more periodically organized structure with much lower signs of preferential milling is the broken crystal heat-damaged structures and lower radiation hardness of the bulk and tendency to its amorphisation. As I mentioned previously, the sputter rate was higher for the stressed sample (20 µm vs 14.5 µm deep craters after depth profiling.). There is a similar feature if both samples are the black dots on the micrographs. One can expect these black dots are etch pits caused by preferential milling. SEM micrograph taken on UHR SEM microscope FEI Magelan (note the used HV and the electron current. Image taken after immersion of the sample in magnetic field) showed this black dots have character of different material widespread on the whole surface. Solidity of these black spots is confirmed on the top the spike in the top of the Fig. 5.29. Two large spots below the spike exhibit charging effect, so I expect low conductivity of these strains.

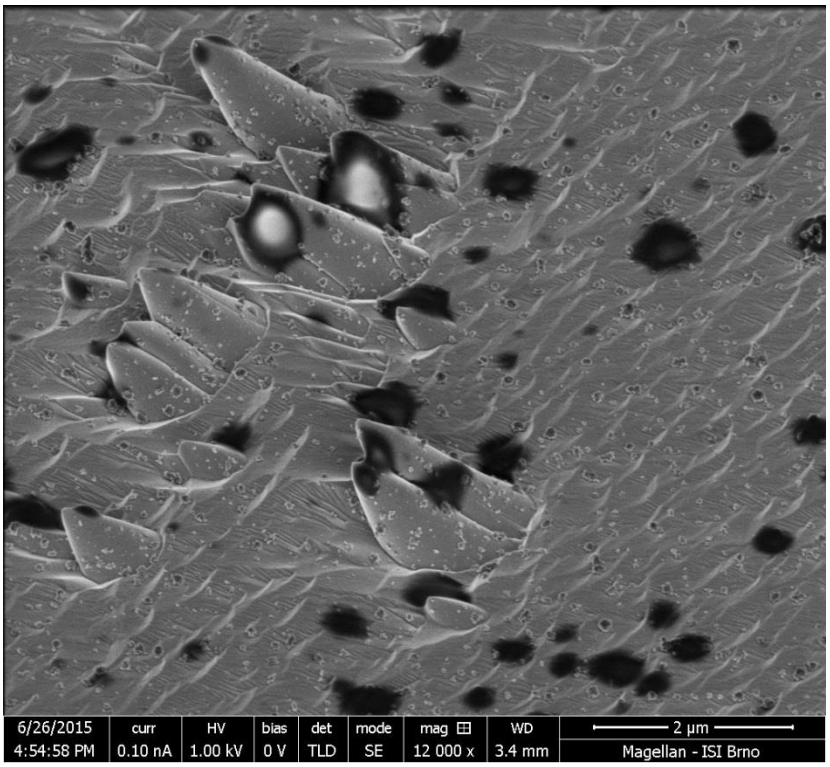

Figure 5.29: SEM micrograph taken on Ultra High Resolution microscope. Black spots on the crater show their solidity.

In search of the elemental composition of these spots, I needed surface sensitive (~ units of nm) instrumentation with high lateral resolution (< 50nm). XPS fulfils the requirement of the surface sensitivity, but its lateral resolution in raster mode is around 2 µm. Scanning Auger Microscope (SAM) was my choice to find composition of these spots. This experiment was done on the Omicron NanoSAM Lab auger microscope. Analysis was done on the unstressed sample.

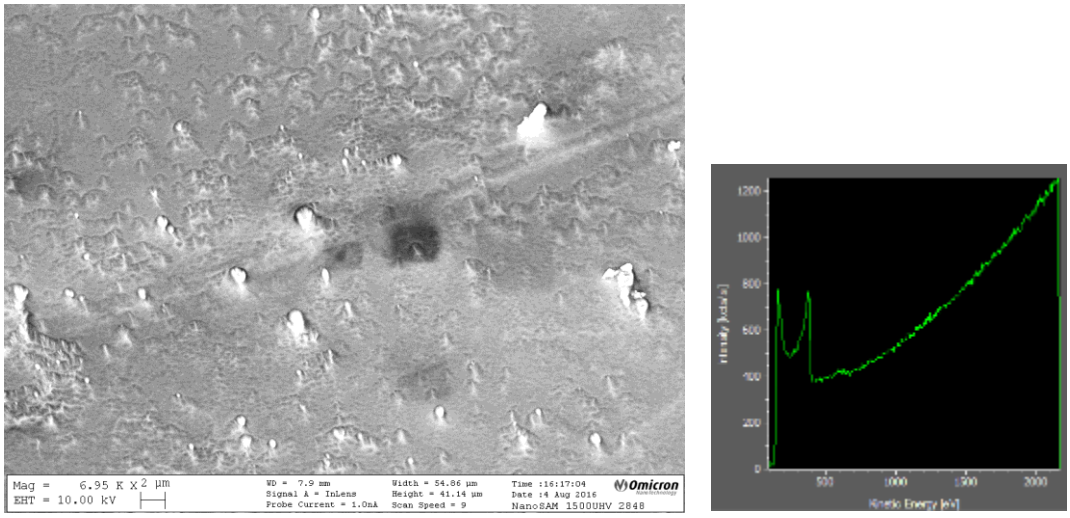

Figure 5.30: SEM micrograph of AES scanned spot in black square. The change of the contrast at AES scan area is caused by the sample charging. Right: Typical AES spectrum.

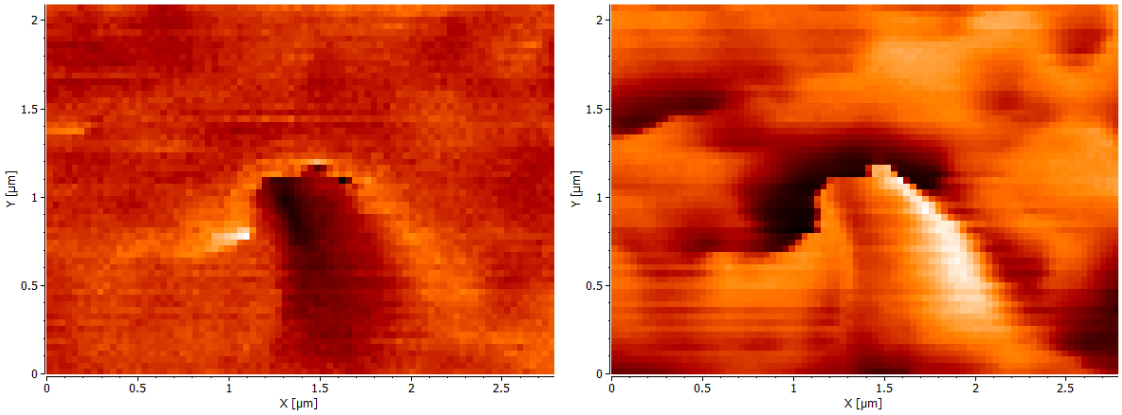

Figure 5.31: Auger maps of Cd (left) and Te (right) of area indicated in Fig. 5.30. Colour closer to white stands for higher concentration.

Unfortunately, I failed in search of componential content of the black spots since the crater underwent some post sputtering structural changes from the time of sputtering (6 months). Nevertheless, the same features of preferential milling as in Fig 30 (left) are still present. The surface was cleaned from surface contamination by short exposure to 500 eV Ar^+ ions broad beam. The artifact that was subject of the scan is the darker area in Fig 5.30 (left). The change if brightness is caused by the charging effect. Auger spectrum showed only Cd and Te in Fig. 5.30 (right). Kinetic energies were 383.70 eV for Cd and 491.50 eV for Te. Visualization by means of AES intensity maps proved that the elevated part of the artifact is Te-rich (Fig. 5.31 right), whereas the snowdrift surrounding this artifact rather Cd-rich (Fig. 6.31 left).

5.3.4.2 AFM analysis

Further study of both samples was focused on the morphology of the surface after sputtering. This was carried out by AFM. The used system was Bruker Dimension ICON. All measurements were done with the ScanAssist probe in semi-contact mode. The AFM high resolution images of the surface of unstressed sample is shown in Fig. 5.32. The AFM image of the stressed sample is in Fig. 5.33.

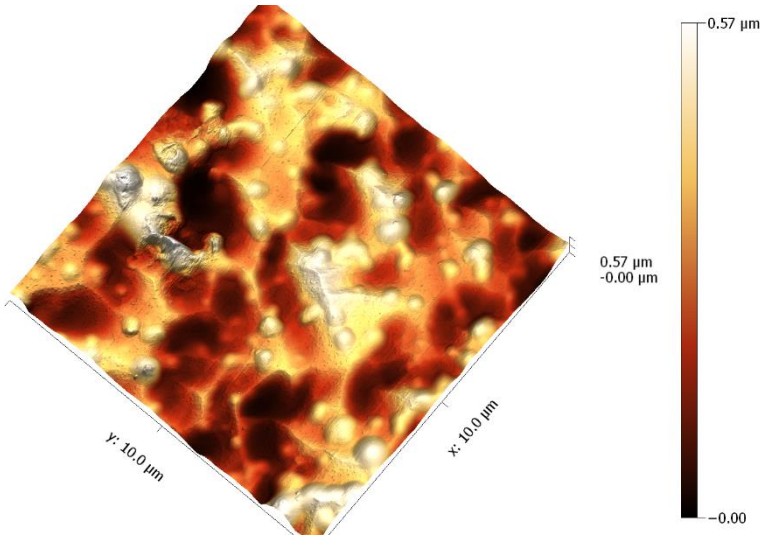

Figure 5.32: AFM scan of the sputter crater of the non-stressed sample.

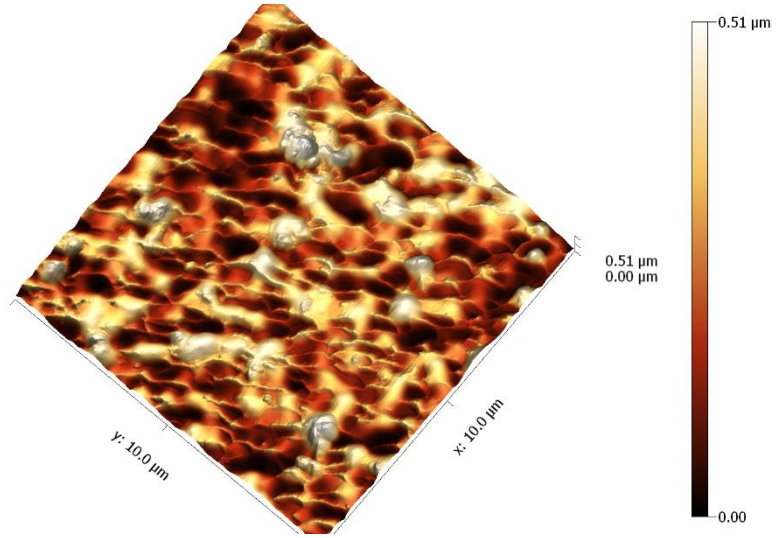

Figure 5.33:AFM scan of the sputter crater of the stressed sample.

Measured RMS roughness of the surface of the unstressed sample was 67.65 nm. The surface of stressed sample was 52.7 nm rough for the case of the stressed sample. The average peak-to-valley height ratios of eroded surfaces were similar for both samples, around 500 nm. As one can see, rather removal rate showed distinctive difference between the stressed and the unstressed sample. The surface shows different nanopatterning of the surface. On the top figure,

The images show that sputtering induces the spontaneous formation of a clear ripple nanopattern on the target surface. The ion beam projection on the sample surface is 40 degrees to the horizontal axis. Hence, as already reported for other materials and different sputter systems [63], the pattern is determined by the ion incidence angle since the ripple wave vector lies parallel to the beam projection on the target surface (i.e. ripples are aligned perpendicular to the ion beam). The ripple wavelength increases with the ion

energy (at this constant dose condition) and, interestingly, a second orthogonal ripple mode with a larger wavelength. Sputter crater of thermally unstressed sample has distinctively different morphology that does not exhibit any oriented pattern even at bigger surface areas (not shown). round-like hillocks are present. Structural analysis those showed these artifacts are highly Te-rich, as proved by AES. From this, I suppose that the origin of such artifacts is that disassociated Cd from the CdTe lattice by long time exposure to 400 K melt and aggregate during sputtering - local temperature of the surface can easily exceed 500 K during long sputtering [63] and Cd melting temperature is 594 K. More detailed study of surface behavior during argon ion bombardment is in Sect. 6.

5.3.4.3 XRD analysis

Methods based on X-ray diffraction (XRD) analysis are well established tools to analyze crystal properties of materials. Very vast quantities can be obtained by XRD, such as preferred crystallographic orientation, lattice mismatch, grain sizes, effect of mechanical stress etc. The wavelength of X-rays is similar to the distance between atoms. The scattering of X-rays from atoms produces a diffraction pattern, which contains information about the atomic arrangement within the crystal. Stress (thermal, mechanical etc.) can lead to increased crystal structure impropriation, which, in complete amorphization, do not have a periodic array with long-range order, so they do not produce a diffraction pattern.

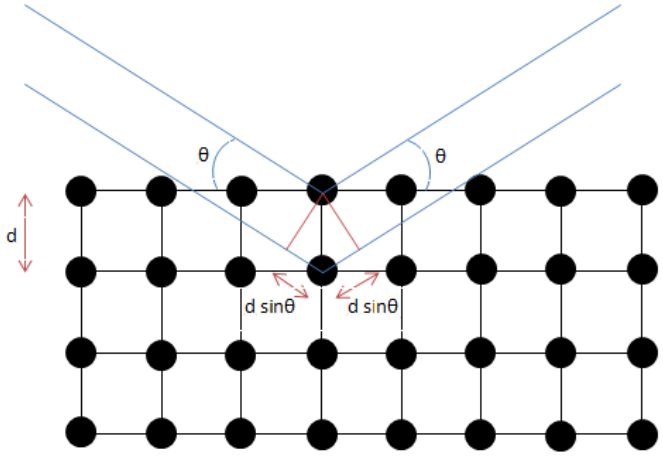

Figure 5.34: Constructive interference of X-rays in the crystal structure

Every crystal contains set of parallel, at some points interleaved planes. These parallel, constantly spaced, crystallographic planes, are identified by Miller indices (*h*, *k*, *l*). These indices carry information about planes position in the crystal. Interplanar distance *d* is related to the Miller indices by relation

$$d = \frac{a}{\sqrt{h^2 + k^2 + l^2}}, \tag{78}$$

where for cubic lattice systems as CdTe single crystals is *a* the only the lattice constant with value of 0.648 nm for CdTe. For X-ray diffraction analysis, an X-ray tube that produces characteristic X-ray radiation is used since it contains spectral lines with exactly defined wavelengths. Sources, generate X-rays by striking the anode target with an

electron beam from a tungsten filament. Wavelengths are given by material of anode. Al or Cu are the most frequent anode materials. Similar X-ray sources are used for XPS.

When the monochromatic X-ray beam irradiates the crystal, the beam is scattered inside the crystal. Because of periodic atom arrangement in lattice, constructive interference from X-rays scattered by parallel planes of atoms will produce a diffraction peak. From Fig 5.34 can be seen origin of diffraction maxima and we are able to formulate conditions necessary to obtain amplified diffracted signal. There are two parallel plains with distance d between them. Two rays of monochromatic X-ray radiation hit the crystal under angle θ. Amplification of diffracted rays (= constructive interference) occurs only between those rays that fulfill that: i) incoming beams are parallel and ii) their distance is integer multiple of X-ray wavelength, $n \times \lambda$, Condition i) is fulfilled when angle of incidence of X-ray equals to the angle of scattered ray, θ. Condition ii) requires fulfillment of well-known Bragg equation

$$n\lambda = 2d \sin\theta \,. \tag{79}$$

This equation tells us that the lower ray in Fig.5.34 has to has to travel, $n \times \lambda$ ($n = 2$ for displayed pair of rays) longer distance than the upper one. From geometrical point of view, this distance difference presents two equal legs $d \sin\theta$ (resp. $n \times \lambda/2$) of two equal right triangles. The XRD method realization comes above mentioned conditions of diffraction. If the sample is rotated by means change of accidental angle of X-rays, the conditions of eq. 79 are fulfilled and constructive interference of scattered rays occurs. From very vast variety of XRD method arrangements, the Brag Brentano geometry was applied in my experiment. The arrangement is shown in Fig. 5.35.

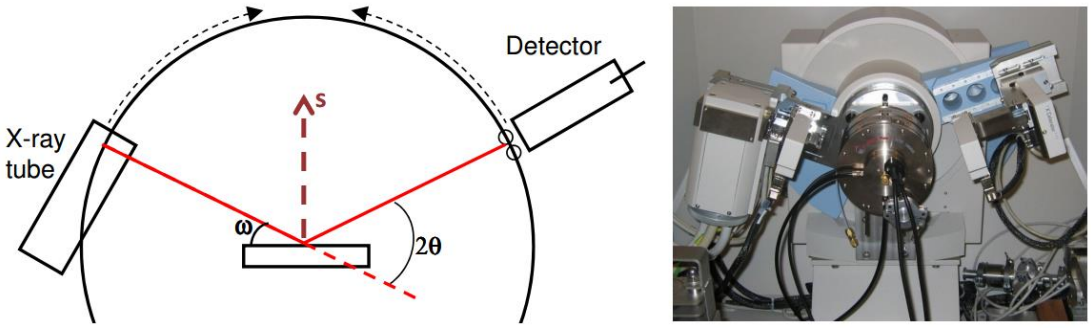

Figure 5.35: Bragg-Brentano configuration for XRD measurements.

The incident angle, ω, is defined between the X-ray source and the sample. The diffraction angle, 2θ, is defined between the incident beam and the detector and incident angle ω is always one half of the detector angle 2θ. In the Bragg-Brentano geometry, the diffraction vector $\boldsymbol{s}$ that bisects the angle between the incident and scattered beam is always normal to the surface of the sample. A single crystal specimen in a Bragg-Brentano diffractometer configuration would produce only one family of peaks (or just a single peak) in the diffraction pattern.

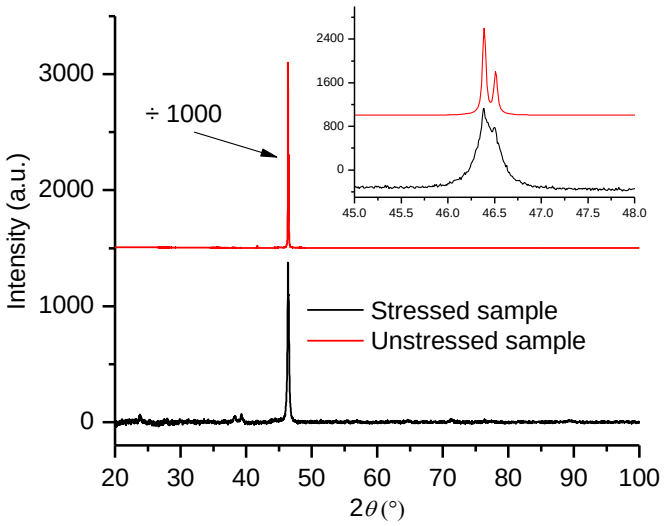

Figure 5.36: X-ray diffraction patterns of both samples. For sake of readiness, the pattern of the unstressed sample is divided by 1000 and vertically shifted.

Figure 5.36 shows the X-ray diffraction patterns corresponding to thermally stressed and unstressed crystals. All the observed XRD maxima can be indexed in the basis of a face centred cubic CdTe phase. Both single crystals have distinctive (311) orientation. Comparison of diffraction intensities of the samples (311) reflection showed 3 orders higher intensity for the case of unstressed sample. This significant difference is caused by increased disorder in the crystal structure of the stressed sample that has some features of polycrystalinity. This structural changes lead to lower constructive diffraction in the stressed sample. Another feature of the (311) diffraction peaks is their shift from theoretical value of $2\theta = 36.40°$ is their shift towards lower angles. For the case of the unstressed sample, the shift is 0.02° and for the stressed sample, the shift is 0.05°. Shift of diffraction peak towards lower angles is generally known as a result of compressive stress. This can be result of argon beam sputtering. Inset of Fig. compressive stress. This can be result of argon beam sputtering. Inset of Fig. 5.36 shows detail of (311) diffraction maxima of both samples. We can see distinctive separation of K_α peak from (311) peak of the sample. Stressed sample showed immersion of those peaks. FWHM of (311) peak is for unstressed sample 0.0437°, whereas this maximum for the stressed sample is 0.1616°. Such notable difference is sign of further polycrystalisation of the stressed sample. Employing eq..78 and 79, the lattice constants a calculated from measured data are 0.64883 nm for the unstressed sample and 0.64887 nm for the stressed sample. Such values are in good respect with theoretical value of 0.6482nm. Beside the K_β peak at $2\theta = 38.34°$ From Fig 5.36 can be seen that some new peaks appear. Diffraction peak at 23.82° belongs to CdTe (111) orientation and the diffraction maximum at 39.31° is typical for (220) orientation.

5.4 Analysis of the effect of thermal stressing on charge transport properties by Schottky theory

The diffusion of Au and other elements is a very important feature with serious impact on electrical behaviour of the M-S interface. Ito investigate charge transport properties of both crystals, I carried out further investigation based on the Schottky theory.

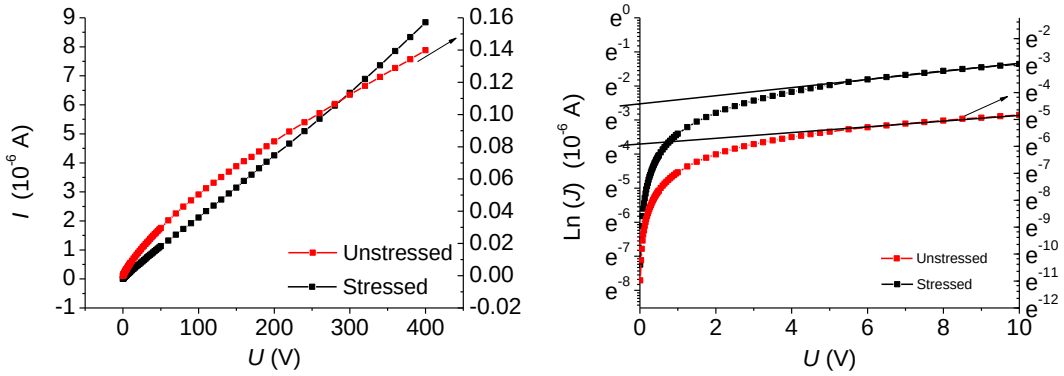

Figure 5.37: I-V characteristics of stressed and unstressed samples (left). Right picture: Transformed ln(*J*)-V curves for low biases of each sample.

Fig 5.37 shows comparison of the *I-V* characteristics from (left) 0 V to +400 V, and (right) are transformed *J-V*s from 0 V to +10 V. My previous measurements showed symmetry of the characteristics biased with the negative polarity. Similarly, as in Section 5.1 the resistivities obtained from the *I-V*s at bias voltage < 0.2 V were $\rho = 1\times10^9$ Ωcm for the unstressed sample and of $\rho = 4\times10^6$ Ωcm for the stressed sample. Remarkable change can be seen from comparison of shapes both characteristics. Unstressed detector shows typical S shape of the *I-V* characteristic, which is given by rectification effect of the contact ($R_c > R_s$), whereas the stressed detector shows linear, ohmic character ($R_c < R_s$).

The current responses of both investigated devices at low bias voltages (0 – 10 V) transformed from the *I-V* curves into ln(*J*)-*V* curves as can be seen at Fig.5.37 (right). The current density *J* for Schottky contacts is given by equation [64]

$$J = J_s \exp\left(\frac{qV}{nkT}\right)\left[1-\exp\left(\frac{qV}{kT}\right)\right], \tag{80}$$

where J_s is the saturation current given by

$$J_s = A^* T^2 \exp -\frac{q\phi_B}{kT}, \tag{81}$$

where A^* is the Richardson constant for CdTe and is equal to 120 $Acm^{-2}K^{-2}$, q is the electron charge, V the applied bias voltage, k is the Boltzmann's constant, T the temperature 300 K, ϕ_B the Schottky barrier height, and J_s the saturation current density obtained from the intercept of the linear part ln(*J*)-*V* curves at zero voltage, as shown in Figure 5.37 (right). From all known values of above mentioned quantities, the Schottky barriers heights are calculated as:

$$\phi_B = \frac{kT}{q}\ln\left(\frac{AT^2}{J_s}\right). \tag{82}$$

Received values of the Schottky barriers are 0.786 eV for the degenerated device and 0.867 eV for the undegenerated detector, respectively. I assume this change to thermally activated diffusion of Au into the CdTe bulk. Increased concentration of In in vicinity of M-S interface and permanent depletion of Cd entrenches this effect. Au locally dopes the sample, which changes the electrical properties of the interracial layer. This change in the electrical properties results in reduction of the barrier height. This conclusion is confirmed by the XPS depth profile of Au shown in Section 5.3. I have to note that the results given by eq. 80 should not completely describe reduction of the Schottky barrier height, since the parameter *A* is given as

$$A^* = \frac{4\pi m_e^* k^2 q}{h^3}, \tag{83}$$

where the electron effective mass $m_e^* \sim 0.13 \times$free electron mass m_0 is material dependent. As revealed by XPS, the M-S interface of investigated samples is a very inhomogeneous heterostructure and contains mixture of purely metallic or mixed forms of Cd, Te and its oxides and electrically active Cl. This brings serious uncertainty for M-S electrical properties analysis based on the regular charge transport models.

6 Investigation of the effect of the argon ion beam on CdZnTe single crystals surface structural properties

Motivation of this part of my work was investigation of the surface by "dry" etching method, by argon ion beams. Surface reconstruction with the goal to obtain a stoichiometric, non-amorphous surface can be obtained by thermal treatment methods. Perfectly reconstructed surfaces are shown in [19] and [65]. Such reconstructed surfaces employed thermal treatment techniques. However, important part of my work shows negative effects of such treatment. Furthermore, one of the goals of thermal treatments - reduction of Te- related point defects in the crystal bulk by annealing is also arguable. In [66], the concentration of Te-inclusions was significantly reduced, the the carrier's mobility-lifetime of such treated detector decreased. Like in [67], a new defect band situated approx. 0.15 eV below the band gap appeared after annealing. Above mentioned facts make and the results presented in this thesis, make, from a practical point of view, surface cleaning/reconstruction methods based on the sample heating (either in vacuum or in defined atmosphere and pressure) impossible because of their irreversible destructivity of the crystal bulk.

So, In this this experiment, I tried another way of mechanically and chemically damaged surface removal by relatively low doses of Ar^+ ions ion beam. Due to different

structural properties, my aim is to remove the defective layer without modification of undamaged bulk volume of CdZnTe crystals. The analyses of the crystal structure after ion beam bombardment is conducted SEM, AFM and XPS.

Again, an n-type (111) oriented CdZnTe VGF grown crystal with dimensions $5 \times 5 \times 2.5$ mm^3 was used in this study. The crystal was not metallized. Couple of minutes before interaction with Ar^+ ion beam, I etched the crystal in 0.3% bromine-methanol for 3 minutes. An argon ion gun was used for the irradiation under ultra-vacuum conditions. The ion current was set to 50 nA, the energy of Ar^+ ions was 5 keV. From all used doses of ion irradiation, five are shown: 3.7×10^{15}, 7×10^{15}, 1.4×10^{16}, 4.9×10^{16} and 2×10^{17} Ar^+ ions/cm^2. The area of irradiated spots on the sample was 300×300 μm^2. The incidental angle of emitted ions with the surface was 90°. To enhance morphological information, SEM micrographs were taken under 50° sample tilt. The XPS analysis was carried out on the Kratos Supra spectrometer (Successor model of the Kratos Ultra that I used in Section 5.3.1). The used image mode allowed us to measure at 1% atomic concentration precision with lateral resolution of 2 μm.

6.1 SEM study of irradiated areas

Figure 6.1 shows SEM micrographs of the sample Fig. 6.1(a) depicts the surface before ion bombardments. Even before irradiation, remarkable etch pits after Br-MeOH etching are visible. Similarly, as for some other etching solutions like Everson solution [68], it was reported that Br-MeOH, especially at concentration higher than 2% and with presence of light, has the tendency to uncover structural defects: Pits and delineates etch lines at grain and sub-grain boundaries on all faces [69]. This is attributed to chemically removing more damaged subsurface material with an impact on surface morphology after etching.

Fig. 6.1(b) shows the detector surface after irradiation by a dose of 3.7×10^{15} Ar^+ ions/cm^2. Obviously, the randomly distributed etch pits are smoothened. More apparent features are dislocation-related lines. The single etch pits form cellular or polygonal arrangements. Such a structure is typically observed if the crystal is grown in a high temperature gradient where the dislocations are gathered around sub-grain boundaries [70, 71]. The SEM image of the surface exposed to a dose of 7×10^{15} Ar^+ ions/cm^2 in Fig. 6.1(c) shows complete vanishing of the shallow randomly distributed etch pits. Nevertheless, the surface still contains signs of waviness and shows presence of pitting effects due to the presence Te inclusions/precipitates along sub-grain boundaries. Further improvement of the surface is a result of fluence 1.4×10^{16} Ar^+ ions/cm^2 in Fig. 6.1(d). The surface seems to be reconstructed, no evidence of etch pits, dislocation networks or scratches from mechanical polishing are visible. The bright large volume artifact on the right-hand side of the picture was identified by EDS as a Te inclusion. The Te inclusion shows signs of preferential removal of the substrate and masks its surrounding area. Sort of "snowdrifts" around these clusters of Te can appear during bombardment with higher ion doses, especially if the angle of incident ions

is not perpendicular to the surface. The Ar^+ dose of 2.1×10^{16} ions/cm^2 (not shown) already caused increased waviness of the surface. Artifacts similar to etch pits like in Fig. 6.1(a) appeared again on the whole surface of the irradiated area. I assume the appearance of small holes due to the effect of ion bombardment and its interaction with buried crystal imperfections. This assumption is proven by increasing the dose to the value 4.9×10^{16} ions/cm^2 (Fig. 6.1(e)). Apparently the density of the dimples increased. Furthermore, an additional effect created by ion beam irradiation of the surface appeared. There are circular craters with similar shapes as on the unsputtered surface, but deeper and with higher diameter reaching up to 300 nm. These craters are gathered in structures like in the case of Te inclusions surrounding sub-grain boundaries. Also, the line indicating the shape of a sub-grain boundary is clearly visible. Part of the surface without irradiation induced pits shows increase of its waviness compared to lower doses. The highest applied dose 2×10^{17} Ar^+ ions/cm^2 displayed in Fig. 6.1(f) caused even more significant change of the surface morphology. The irradiation caused craters as described for the previous case, with increased diameters to approx. 1 μm, covering most of the surface area. Herein I explain the nature of these: As a result of imperfect crystal growth, Te inclusions are randomly distributed in the crystal volume. The ion bombardment supplies energy to the crystal structure. Te clusters and dislocation patterns act as attractors for energy exchange. In other words, the energy is preferably given to buried metallic Te located just below the surface and the CdTe layer between the surface and Te cluster location is preferably removed. Furthermore, ion bombardment increases the segregation coefficient for Te and promotes formation of extra Te clusters [72].

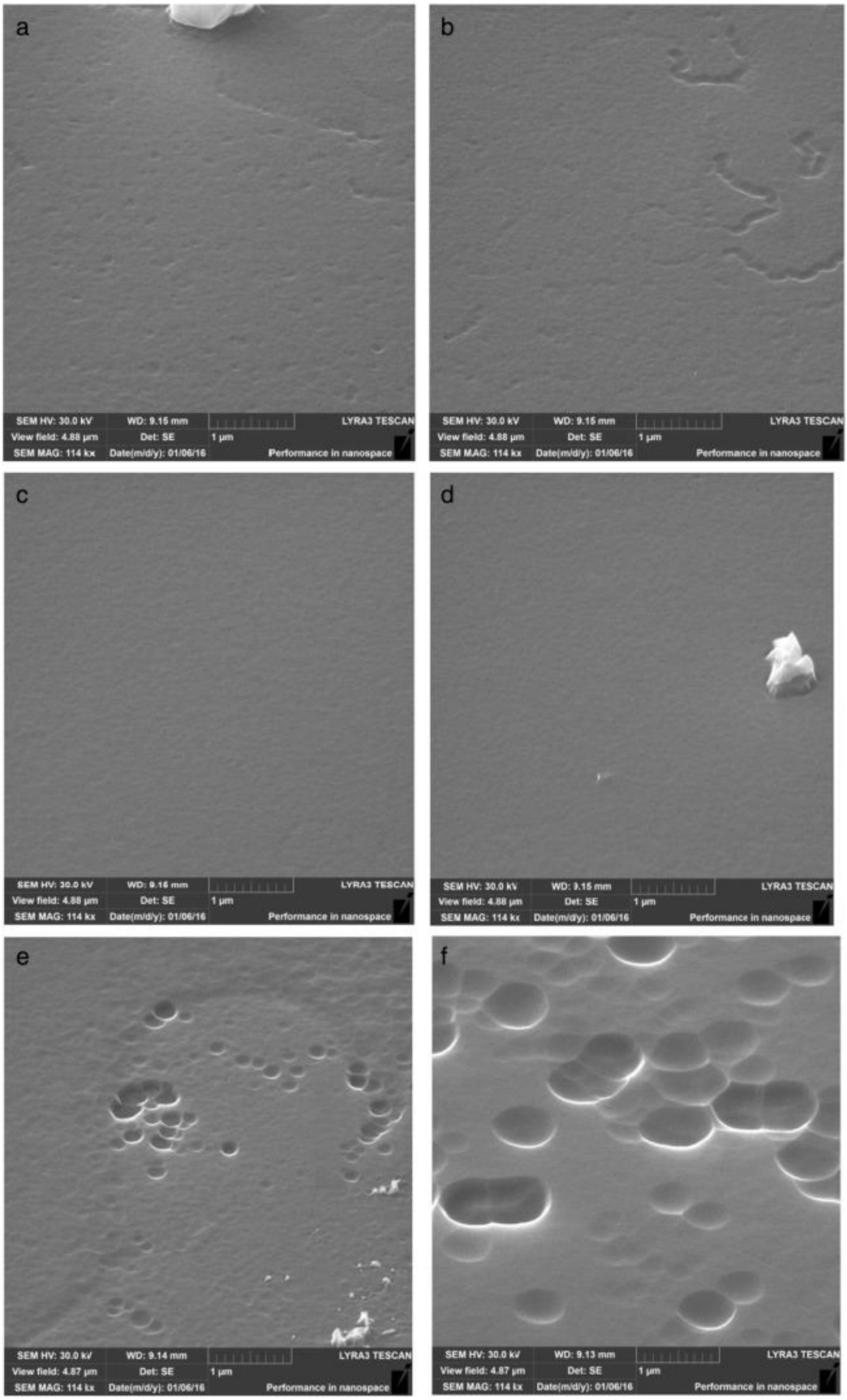

Figure 6.1: SEM images of CdZnTe surface a) freshly etched before ion irradiation b) After Ar^+ ion fluence 3.7 × 10^{15} Ar^+ ions / cm^2, c) 7 × 10^{15} Ar^+ ions / cm^2, d) 1.4 × 10^{16} Ar^+ ions / cm^2, e) 4.9 × 10^{16} Ar^+ ions / cm^2 and f) 2 × 10^{17} Ar^+ ions / cm^2.

6.2 AFM study of irradiated areas

Fig. 6.2(a) shows an AFM image of the just chemically etched surface. Its height is distributed homogeneously; no mechanical scratches; surface waviness is visible. The Inset in the picture shows the 2D morphology of etch cellular structure as the one scanned by SEM in Fig. 6.1(a). After the dose of 3.7×10^{15} Ar^+ ions/cm^2, the surface firstly showed remarkable surface morphology change. Two apparently different regions appear — a smooth one in the lower part of Fig. 6.2(b) and a very rough part in the top part of the picture. The rough part is mutually 15 nm deeper/lower penetrated than the plain of the smooth surface. I assume that creation of these regions is the result of an incomplete removal of mechanically damaged surface, which thickness can be from tens of nm to several μm. The smooth area has more porous-like structure than the unirradiated surface. Furthermore, some signs of waviness of the surface are notable. After irradiation dose of 7×10^{15} Ar^+ ions/cm^2, two distinct surfaces are still visible. Nevertheless, the uplifted plains are crushed into smaller areas, which are only about 10 nm higher than the average height plain of the smoother part of the surface (17 nm). Preferential removal of the surface is present. The average depth of the pits below the average height of the surface reaches up to 25 nm. Fig. 6.2(d) depicts the surface morphology after the dose of 1.4×10^{16} Ar^+ ions/cm^2. For this ion dose, the SEM micrograph in Fig. 6.1(d) showed best morphology. Similar results come from the AFM. However, waviness of the surface is apparent. Our search among the whole crater did not result in finding such heterogeneous surface like in the previous two cases. The surface shows very high smoothness without any steep peaks (dust, residuals on the surface), but apparent waviness with signs of a new crater generation. Nevertheless, the depth of these craters did not exceed 13 nm below the valleys originated by the ion irradiation. The morphology of the surface after ion irradiation fluence of 2.1×10^{16} Ar^+ ions/cm^2 (not shown), the patterning of preferably removed areas has changed, from valley-like to grid-like with craters situated in intersects of the valleys. These round like craters are situated at the intersection of dislocations networks that have this configuration. These dislocation walls can be revealed by using specific etchants [68, 73]. The dislocations behave as non-radiative recombination regions. Both cellular and cross-like dislocation patterns can be clearly seen by panchromatic cathodoluminescence imaging [74]. Measured average depth of the ion etch pits is higher than in the previous case: 20 nm. Very similar morphology of the surface is found for fluence of 4.1×10^{16} Ar^+ions/cm^2 (Fig. 6.2(e)). Etch pits show a tendency to merge together and their average depth increased to 55 nm. Finally, Fig.6. 2(f) represents AFM data for the dose of 2.0×10^{17} Ar^+ ions/cm^2. Such a dose caused conversion of the smooth surface of the sample to a heavily eroded one with randomly distributed pits on the surface, which are up to 110 nm deep.

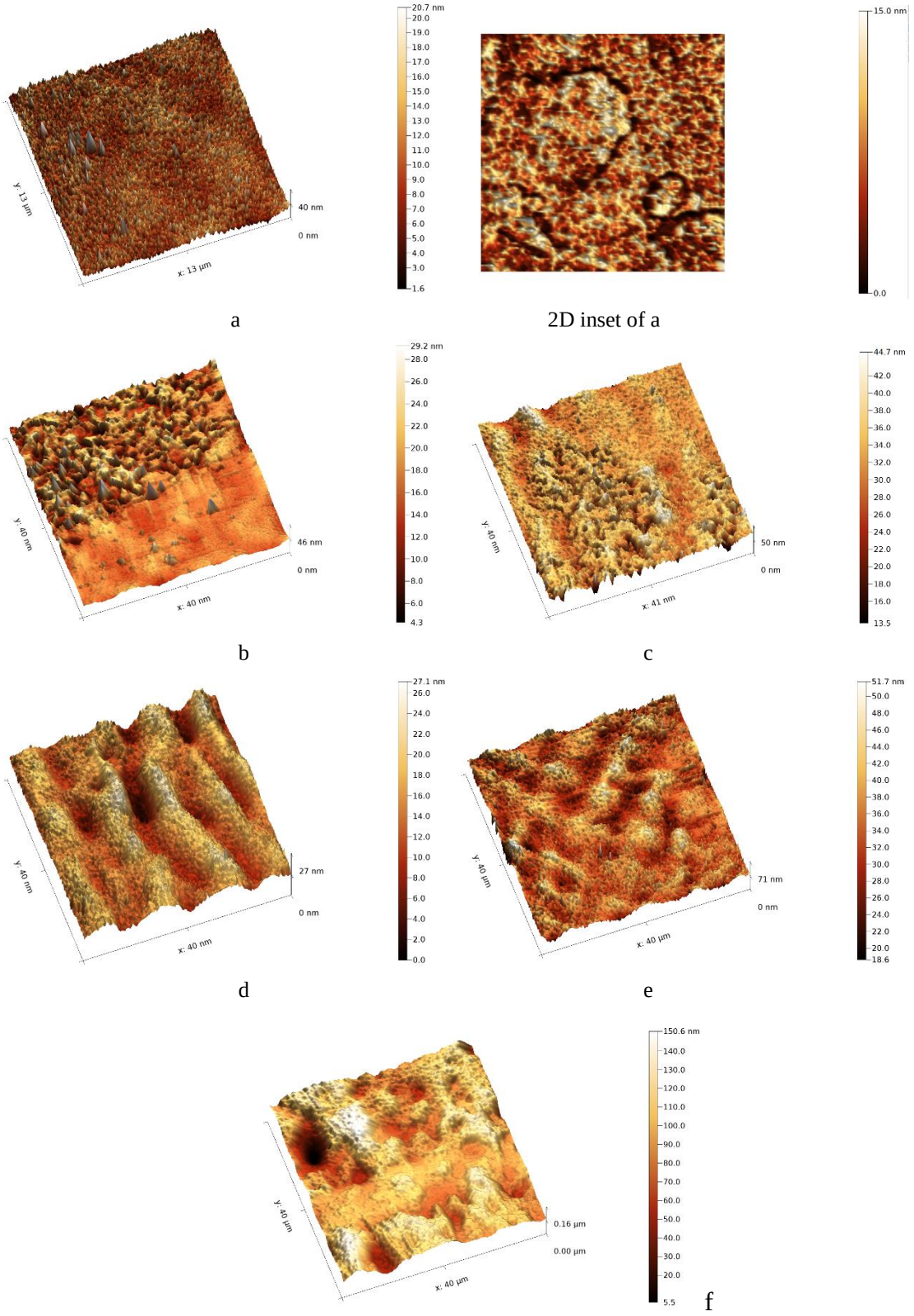

Figure 6.2: 3D AFM images of CdZnTe surface a) freshly etched before ion irradiation b) After Ar^+ ion fluence 3.7 $\times 10^{15}$ Ar^+ ions / cm^2, c) 7 $\times$ 10^{15} Ar^+ ions / cm^2, d) 1.4 $\times$ 10^{16} Ar^+ ions / cm^2, e) 4.9 $\times$ 10^{16} Ar^+ ions / cm^2 and f) 2 $\times$ 10^{17} Ar^+ ions / cm^2

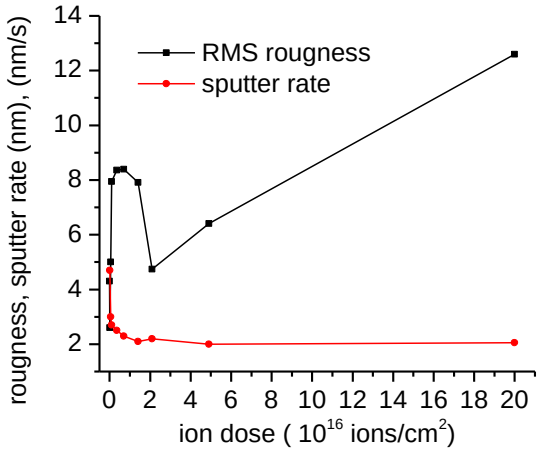

Figure 6.3:Dependence of the surface RMS roughness (squares) and the sputter rate (dots) on the Ar^+ion dose.

Fig. 6.3 shows relation of the surface the RMS roughness (squares) and the sputter rate (dots) on ion dose. Sputter rates were calculated from difference of medium depths of the craters generated by the previous, lower dose and differences of sputtering times between lower and higher dose. The roughness of the unsputtered surface was 4.31 nm. After ion dose 1×10^{14} ions/cm^2, the surface roughness decreased to 2.6 nm. This was followed with the change of etch rate from 4.7 nm/s to 3.0 nm/s. The reason of such a significant change of both parameters is removal of carbon contamination on the surface, a residual from methanol that was used to rinse away the Br-MeOh etchant as reported in other studies, e.g. [75]. This situation is confirmed in Fig. 6.5 that shows XPS map of the C1s photopeak. The Te-rich layer, which also favors the higher sputter rate, originates from chemical etching and has a thickness of about 2 nm [76]. The fluence of 1×10^{14} ions/cm^2 was sufficient to remove the Te-rich layer, since sputtering time to remove a 2 nm thick layer is 400 ms. Sputter rates of higher fluences monotonously decreased to the value 2.2 nm/s (for fluence 1.4×10^{16} ions/cm^2), which corresponds to an approx. 145 nm deep crater, measured by profilometer. For the other higher doses, the sputter rate remained constant.

The surface roughness has remarkably increased just after the first “cleaning” fluence 1×10^{14} ions/cm^2 and had approximately the same value around 8 nm for doses from 1×10^{15} to 1.4×10^{16} ions/cm^2. For the value 2.1×10^{16} ions/cm^2, the roughness of the surface dropped to the value 4.74 nm, but as mentioned previously, extended surface waviness appeared. Surface erosion caused by higher irradiation doses caused increasing surface roughness ending at 12.6 nm for the fluence 2×10^{17} ions/cm^2. 1.3 μm of the surface was removed by this dose.

6.3 XPS study of irradiated areas

The wide XPS spectra showed no presence of the O 1s peak and the detail scans of Te did not show peak broadening / energy shifting from the value 537.0 eV of the Te 3d peak. Thus, chemical etching successfully removed oxidized layer. Furthermore, there was no evidence of bromine contamination on the surface. So, the relative concentration of Te, Cd and C was measured by XPS in imaging mode. Te 3d5, Cd 3d5, Zn 3p and C 1s peaks were selected for imaging. Measured intensities were multiplied by FWHMs of these peaks to obtain the area of the peak. The areas of the peaks were multiplied by the relative sensitivity factors of each element of interest and relative concentration was computed. The relative concentrations of Te and C are shown in Fig. 6.4 and Fig. 6.5, respectively.

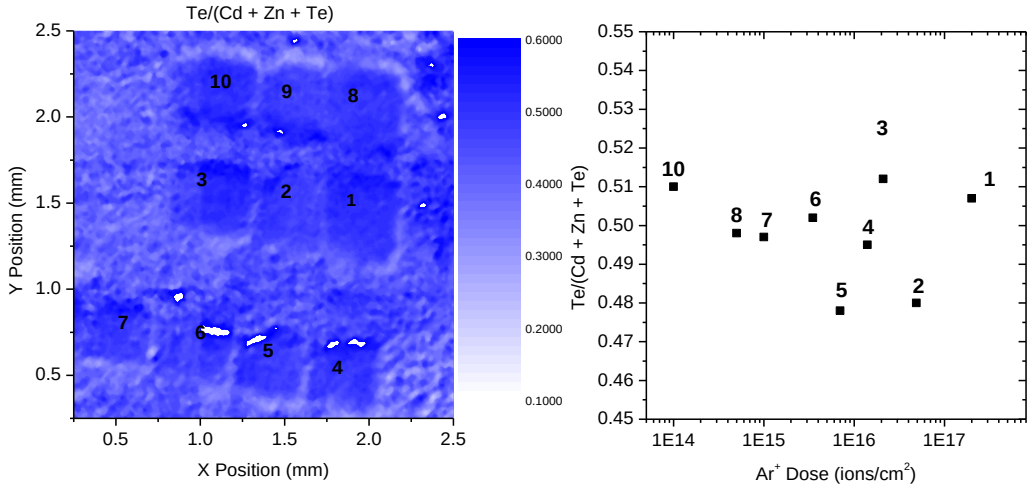

Figure 6.4: Map of relative concentration of Te to Cd+Zn. Craters are marked by numbers (left). Signal from the center of the crater was averaged and plotted depending on the ion dose (right). Spot 9 was used for calibration and as an orientation point.

The relative concentration of Te /(Cd + Zn + Te) that is depicted in Fig. 6.4 shows that the stoichiometry of the surface did not show remarkable changes during sputtering. From this, I conclude that no preferential removal of eider Cd (Zn) or Te happened. Preferential removal is related to structural defects buried beneath the surface. Argon ion irradiation has a similar feature as Br-MeOH etching, i.e. surface smoothening and improve its condition, followed by uncovering structural defects at higher doses / etching times.

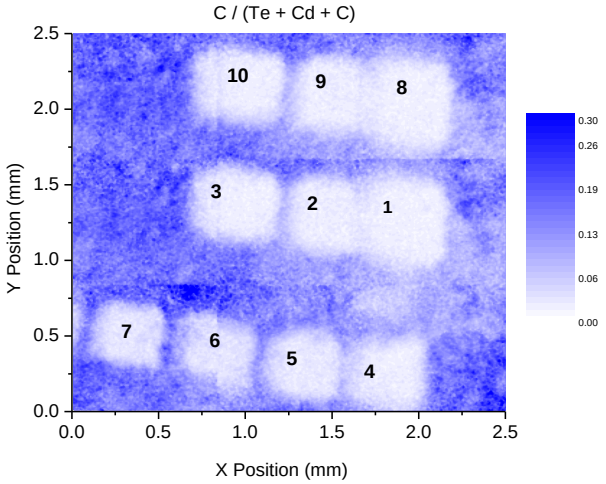

Figure 6.5: Map of relative concentration of C to Te and Cd. Relative concentration of C in craters is ~ 2% and outside of the crater the concentration reaches ~ 18%.

Fig. 6.5 shows the relative concentration of carbon on the surface. The relative concentration of C in craters is ~ 2% and outside of the crater the concentration reaches ~ 18%. After irradiation by the lowest used dose of 1×10^{14} ions/cm^2, the atomic concentration of carbon dropped below 2%. At unsputtered areas, the average ratio of Te/(Cd + Zn + Te) after subtraction of C is 1.37, pointing at the presence of Te-rich layer on the surface.

To conclude, the fluence of 1 -2 $\times 10^{16}$ Ar^+ ions/cm^2 with energy of 5 keV seems to be beneficial for reconstruction of CdTe surface, since lower fluencies unsatisfactory remove the damaged part of the structure. Nevertheless, surface waviness was observed as a result of irradiation at these doses. The dose can vary according to the surface processing: type and concentration of etchant and etching time. Furthermore, mechanical treatment of cut crystals [77] can leave several μm of damaged crystal structure detected by photoluminescence.

Two distinctive regions appear. Initial dose already dramatically increased the surface roughness by removal of loosely bonded parts of the surface, followed by its smoothening up to the fluence of 2.1×10^{16} Ar^+ ions/cm^2. Higher values caused surface roughening due to preferential removal of damaged crystal structure. The nature of surface removal is seriously influenced by the quality of the crystal growth and subsequent annealing [78], because point defects and grain sub-boundaries buried just below the surface enhance the energy transfer between the surface above the inclusions/precipitates and incident Ar^+ ions [72].

A periodically arranged structure of preferentially removed area is attributed to the geometrical arrangement of dislocation walls, as can be seen in [73] and [74]. Intersects of these structural defects are the places of origin of preferentially removed dimples. Periodicity is affected by various depths of dislocations and mixtures between cellular and cross-like shapes of the dislocation walls. At higher fluences, more sputtering effects have to be taken into account, such as increased local temperature of the irradiated area

and the fact that the position of dislocation structures changes with depth from the surface and inclusions located out of dislocation patterns are uncovered. Onset of a significant ripple structure was found at fluences higher than 2.1×10^{16} Ar^+ ions/cm^2. This value was related to an increase of RMS roughness of the surface. The sputter rate was constant from the dose 7×10^{15} Ar^+ ions/cm^2. The stability of the sputter rate is due to the high radiation hardness of CdTe / CdZnTe and the surface does not tend to amorphize during sputtering with fluences below 10^{17} Ar^+ ions/cm^2[79] for Argon ion energy 5 keV. This ion energy and used ion fluences were found to be not high enough to increase sputter yield (as an indicator of the surface amorphisation) as reported in [80] for other materials and ions. Another study on CdZnTe [63] shows periodically formed etching patterns at high Ar^+ ion energies (30 - 200 keV) and two-order higher doses and Ar^+ ions energies than maximum used in this work. This patterning can be imputed to extended thermal stress of the surface, resulting in formation of new cross oriented dislocation sites. However, the 60° incidence of the ion beam used in the quoted study has to be taken into account. I believe that the density of dislocation networks near the surface is also related to up to several μm thick plastically deformed regions damaged by lapping rather than structural defects of the crystal bulk. Relatively short chemical etching times (~ 1 min, concentration of Br in MeOH below 2%) published in literature are rather the result of request of the smooth surface retrieval than complete removal of the damaged layer.

7 Conclusion

In my work, I employed more than eight analytical methods in order to investigate detectors features at various stat of quality. The first part of the work was dedicated to analyse samples by additive noise analysis, *I-Vs*, current stability and electric field distribution. Also, I separated noise sources of the detectors. My findings from this part are:

- Surface leakage current is the dominant source of noise and has highest contribution to leakage currents of the detector system[a1]
- From the Pockels effect measurements, space-charge build-up appears after the detector biasing. This result in creation of inactive, dead layers with zero electric field. Such monitored electric field distribution allowed me to calculate energy level that is responsible for the detector polarization. According to my calculations based on the charge accumulation model, the responsive deep trap has energy 0.88 eV.
- Polarization influences noise properties of the detector system. I observed increase of the $1/f$ noise in time with much higher exponent than two with increasing current. The reason of much steeper increase of the noise with increasing current is screening effect of the space charge and changes of spatial

distribution of charge carriers in the bulk and, especially in vicinity of contacts. On contrary, polarization supresses the shot noise of the detector [a2].

- Improper contacts deposition results in expectable higher leakage currents. Additive noise analysis showed that the most significant change is the how big is the increase of the 1/*f* noise spectral density with applied voltage.
- Long-time exposure of the detector to temperatures higher than 400 K causes its irreversible degradation. This leads to higher leakage current and, again significantly higher increase of 1/*f* noise with applied bias voltage.

To generalize above mentioned facts, a good detector from should show these features:

- Low leakage current that, emphasized by rectification effect of Schottky contacts should have resistivity equivalent to 10^{11} Ωcm. At higher voltages, the characteristics should be linear, without any signs of superlinearity, cause by tunnelling etc.
- 1/*f* noise spectrum should have constant value of *m* in the whole frequency band, where 1/*f* noise applies. The value of *m* should be around unity. Variability of *m* in $1/f^{\,m}$ noise spectrum is a sign of dominating defect level. Opposite case appeared in all defective states of samples, including developed space charge.
- Increase of the value of $1/f^{\,m}$ noise spectral density with power of two with increasing bias voltage / leakage current. Higher values were typical for all defective states of samples, including developed space charge.
- Position of the$1/f^{\,m}$ noise corner at as low frequencies as possible. Unfortunately, higher sensitivity and higher bandwidth of the signal sampling is needed. This will be focus of my work for the future.

The second part of my work dealt with structural and morphological properties of M-S interface of a detector grade detector and irreversively degraded one by exposure to high operational temperatures for long time. For my investigation, I used advanced analytical methods: X-ray Photoemission Spectroscopy, Atomic Force Microscopy, Scanning Electron Microscopy, Scanning Auger Microscopy X-ray Diffraction and Secondary Ion Mass Spectroscopy as tools for the analysis.

The XPS results showed that the borderline between CdTe and Au is not abrupt, but with signs of diffusion of Au into the crystal bulk. The Au 4f photoemission peak was not shifted and gold is present only in its purely metallic form. The O 1s peak was detected during the existence of Au in the XPS spectrum. Even more interesting behavior showed Cd and Te. During depth profiling Cd showed very slight < 0.2 eV shift from its metallic state. This generally known fact makes difficult to distinguish oxidation state of Cd by XPS. Therefore, I carried out unconventional and yet not published comparison of Cd 3d photoemission peaks positions with the atomic concentrations of sub-oxide states of Te and atomic concentration of Cl in M-S interface. This showed that the existence of Te sub-oxide and the slight shift of is linked to presence of Cl in the spectrum. After disappearance of Cl from the XPS spectrum, only Te^{4+} (TeO_2) and metallic Te were found. After vanishing of the Te^{4+} state, the Cd/Te ratio attained stoichiometry, i.e. from

Te-rich to the ratio of Te/Cd = 1. To conclude, presence of Cl is guilty of the presence of highly disordered layer in Au/CdTe interface. SIMS as the most sensitive component analysis method available allowed me to specify the results more precisely. Not only Au and oxygen exist together in M-S interface, but also Cl coexists with those elements. Diffusion depth of $H[AuCl_3(OH)]$ defines the thickness of bilayer between Au and CdTe. This bilayer has serious effect on the detector performance. It is a distorted structure, where CdTe is strongly dissociated, because Cd reacts primarily with Cl and Te forms TeO_2 and some Te is left in its metallic form. Such situation leads to detection of sub-oxide form of Te by XPS. Comparison of the data for stressed and unstressed sample showed permanent depletion of Cd for the case of stressed sample. Otherwise, chemical properties in M-S interface were quite similar, but the stressed detector showed more gradual depth profile of O, Cl and Au, pointing at that thermal stress cause enhanced diffusion of these elements into the bulk. I find the depletion from Cd as the most important result of thermal stress of the detector. This serious structural change results in different morphology and nanopatterning sputtered areas. Similarly, lack of Cd is cause of detected lower diffraction intensity and diffraction peak broadening in case of XRD analysis.

The last part of my work was focused on finding the best dose of Ar^+ ions for the surface bombardment. The aim was reconstruction of the sample surface that was etched in Br-MeOH solution. This requires minimal additional damage of the surface. Found best dose of approx. 10^{16} Ar^+ ions resulted in smooth surface. Such dose showed no damage signs, like irradiated surface waviness, preferential milling of either Te or Cd(Zn) [a3].

8 References

[1] DEL SORDO, S., L. ABBENE, E. CAROLI, A. M. MANCINI, A. ZAPPETTINI and P. UBERTINI. Progress in the Development of CdTe and CdZnTe Semiconductor Radiation Detectors for Astrophysical and Medical Applications. *Sensors*. 2009, **9**(5), 3491-3526. DOI: 10.3390/s90503491. ISSN 14248220.

[2] SCHLESINGER, T. E., J. E. TONEY, H. YOON, E. Y. LEE, B. A. BRUNETT, L. FRANKS and R. B. JAMES. Cadmium zinc telluride and its use as a nuclear radiation detector material. *Materials Science and Engineering: R: Reports*. 2001, **32**(4-5), 103-189. DOI: 10.1016/S0927-796X(01)00027-4. ISSN 0927796x.

[3] SHIRAKI, H., M. FUNAKI, Y. ANDO, S. KOMINAMI, K. AMEMIYA and R. OHNO. Improvement of the Productivity in the THM Growth of CdTe Single Crystal as Nuclear Radiation Detector. *IEEE Transactions on Nuclear Science*. 2010, **57**(1), 395-39. DOI: 10.1109/TNS.2009.2035316. ISSN 00189499.

[4] CHEN, H., R. B. JAMES, L. A. FRANKS, et al. CZT device with improved sensitivity for medical imaging and homeland security applications. In: *Hard X-Ray, Gamma-Ray, and Neutron Detector Physics XI*. SPIE Proceedings Vol. 7449, 2009, 744902-744912. DOI: 10.1117/12.828514. IBSN 1996-756X.

[5] LOVERGINE, N., P. PRETE, L. TAPFER, F. MARZO and A. M. MANCINI. Hydrogen transport vapour growth and properties of thick CdTe epilayers for RT X-ray detector applications. *Crystal Research and Technology*. 2005, **40**(10-11), 1018-1022. DOI: 10.1002/crat.200410478. ISSN 02321300.

[6] CASTALDINI, A., A. CAVALLINI, B. FRABONI, P. FERNANDEZ and J. PIQUERAS. Deep energy levels in CdTe and CdZnTe. *Journal of Applied Physics*. 1998, **83**(4), 2121-2126. DOI: 10.1063/1.366946. ISBN 10.1063/1.366946

[7] TRAVERSA, M., P. PRETE, I. FARELLA, P. PAIANO, F. MARZO, A. COLA, N. LOVERGINE and A. M. MANCINI. A MOVPE technology for fabrication of CdTe-based homoepitaxial p-i-n diode structures as nuclear radiation detectors. In: *2007 2nd International Workshop on Advances in Sensors and Interface*. IEEE, 2007, s. 1-5. DOI: 10.1109/IWASI.2007.4420028. ISBN 9781424412440.

[8] CAPPER, P. *Properties of narrow gap cadmium-based compounds*. London: INSPEC, the Institution of Electrical Engineers, 1994, 240 s. EMIS data reviews series, no. 10. ISBN 0852968809.

[9] SZE, S. M. and Kwok Kwok NG. *Physics of semiconductor devices*. 3rd ed. Hoboken, N.J.: Wiley-Interscience, 2007. ISBN 9780471143239.

[10] WANG, F. F., A. L. FAHRENBRUCH and R. H. BUBE. Properties of metal-semiconductor and metal-insulator-semiconductor junctions on CdTe single crystals. *Journal of Applied Physics*. 1989, **65**(9), 3552 - 3559. DOI: 10.1063/1.342630. ISBN 10.1063/1.342630.

[11] TOMASHIK, Z. F., V. M. TOMASHIK, I. B. STRATIYCHUK, G. M. OKREPKA, I. I. HNATIV, P. MORAVEC, P. HÖSCHL and J. BOK. Chemical–Mechanical Polishing of CdTe and Zn x Cd1−x Te Single Crystals by H2O2(HNO3)–HBr–Organic Solvent Etchant Compositions. *Journal of Electronic Materials*. 2009,**38**(8), 1637-1644. DOI: 10.1007/s11664-009-0692-8. ISSN 03615235.

[12] NILES, D. W., X. LI, P. SHELDON and H. HÖCHST. A photoemission determination of the band diagram of the Te/CdTe interface. *Journal of Applied Physics*. 1995, **77**(9), 4489 - 4495. DOI: 10.1063/1.359444.. ISSN 1089-7550.

[13] GORICHOK, I. V., P. M. FOCHUK, Y. V. VERZHAK, T. O. PARASHCHUK, D. M. FREIK, O. E. PANCHUK, A. E. BOLOTNIKOV and R. B. JAMES. Compensation mechanism of bromine dopants in cadmium telluride single crystals. *Journal of Crystal Growth*. 2015, **415**, 146-. DOI: 10.1016/j.jcrysgro.2014.11.005. ISSN 00220248.

[14] IRFAN, W. XIA, H. LIN, H. DING, C. W. TANG and Y. GAO. Nitric–phosphoric acid etching effects on the surface chemical composition of CdTe thin film. *Thin Solid Films*. 2012, **520**(6), 1988-1992. DOI: 10.1016/j.tsf.2011.08.113. ISSN 00406090.

[15] LEE, S. H., H. SHIN, H. C. LEE and C. KI KIM. New surface treatment method for improving the interface characteristics of CdTe/Hg1−xCdxTe heterostructure. *Journal of Electronic Materials*. 1997, **26**(6), 556-560. DOI: 10.1007/s11664-997-0193-6. ISSN 03615235.

[16] WANG, Linjun, Wenbin SANG, Weimin SHI, Yongbiao QIAN, Jiahua MIN, Donghua LIU and Yiben XIA. Electrical properties of contacts on P-type Cd0.8Zn0.2Te crystal surfaces. *Nuclear Instruments and Methods in Physics Research Section A: Accelerators, Spectrometers, Detectors and Associated Equipment*. 2000, **448**(3), 581-585. DOI: 10.1016/S0168-9002(00)00293-X. ISSN 01689002.

[17] TOMASHIK, Z. F., F. F. SIZOV, J. V. GUMENJUK-SICHEVSKA, O. R. GUMENYUK, V. N. TOMASHIK and S. A. KOSTYUKEVYCH. Chemical etching of CdTe and CdxHg 1-x Te in the H 2 O 2 -HJ-tartaric acid solutions. In:*Sixth International Conference on Material Science and Material Properties for Infrared Optoelectronics*. Kiyv: Proc. SPIE 5065, 2002, s. 241-346.DOI: 10.1117/12.502293. ISSN 0277-786X.

[18] KELLER, R. C., H. ZIMMERMANN, M. SEELMANN-EGGEBERT and H. J. RICHTER. Surface cleaning and etching of CdZnTe and CdTe in H2/Ar, CH4/H2/Ar, and CH4/H2/N2/Ar electron cyclotron resonance plasmas.*Journal of Electronic Materials*. 1997, **26**(6), 542-. DOI: 10.1007/s11664-997-0191-8. ISSN 03615235.

[19] COHEN-TAGURI, G., M. LEVINSHTEIN, A. RUZIN and I. GOLDFARB. Real-space identification of the CZT(110) surface atomic structure by scanning tunneling microscopy. *Surface Science*. 2008, **602**(3), 712-723. DOI: 10.1016/j.susc.2007.11.026. ISSN 00396028.

[20] YANG, Tian-Juh and Tai-Bor WU. Effect of Etching on Composition and Morphology of CdTe(111) Surfaces. *Japanese Journal of Applied Physics*. **34**(Part 1, No. 11), 6184-6194. DOI: 10.1143/JJAP.34.6184. ISSN 00214922.

[21] ANDREEV, A., L. GRMELA, P. MORAVEC, G. BOSMAN and J. SIKULA. Investigation of excess 1/ f noise in CdTe single crystals. *Semiconductor Science and Technology*. 2010, **25**(5), 055016. DOI: 10.1088/0268-1242/25/5/055016. ISSN 02681242

[22] VAN DER ZIEL, A. Unified presentation of 1/f noise in electron devices: fundamental 1/f noise sources.*Proceedings of the IEEE*. **76**(3), 233-258. DOI: 10.1109/5.4401. ISSN 00189219.

[23] CHOO, S.C. Carrier generation-recombination in the space-charge region of an asymmetrical p-n junction. *Solid-State Electronics*. 1968, **11**(11), 1069-1077. DOI: 10.1016/0038-1101(68)90129-9. ISSN 00381101.

[24] SHOCKLEY, W. and W. T. READ. Statistics of the Recombinations of Holes and Electrons. *Physical Review*. 1952, **87**(5), 835-842. DOI: 10.1103/PhysRev.87.835. ISSN 0031-899x.

[25] SAH, Chih-tang, R. NOYCE and W. SHOCKLEY. Carrier Generation and Recombination in P-N Junctions and P-N Junction Characteristics. *Proceedings of the IRE*. 1957, **45**(9), 1228-1243. DOI: 10.1109/JRPROC.1957.278528. ISSN 00968390.

[26] BALANDIN, A. A. *Noise and fluctuations control in electronic devices*. 1. Stevenson Ranch, Calif.: American Scientific Publishers, 2002. ISBN 1588830055.

[27] MAINZER, N., E. LAKIN a E. ZOLOTOYABKO. Point-defect influence on 1/f noise in HgCdTe photodiodes. *Applied Physics Letters* . 2002, **81**(4), 763-766. DOI: 10.1063/1.1494118. ISSN 00036951.

[28] HOOGE, F. N., T. G. M. KLEINPENNING and L. K. J. VANDAMME. Experimental studies on 1/f noise. *Reports on Progress in Physics*. 1981, **44**(5), 479-532. DOI: 10.1088/0034-4885/44/5/001. ISSN 00344885.

[29] MCWHORTER, A. L. *1/f noise and related surface effects in germanium*. Lincoln Laboratory, 1955. Available online at: https://dspace.mit.edu/handle/1721.1/4786. Sc.D. thesis. Massachusetts Institute of Technology, Research Laboratory of Electronics.

[30] SU, Ching-Hua. Energy band gap, intrinsic carrier concentration, and Fermi level of CdTe bulk crystal between 304 and 1067 K. *Journal of Applied Physics*. 2008, **103**(8), 084903. DOI: 10.1063/1.2899087. ISSN 00218979.

[31] KLEINPENNING, T. G. M. 1/f noise in thermo EMF of intrinsic and extrinsic semiconductors. *Physica*. 1974, **77**(1), 78-98. DOI: 10.1016/0031-8914(74)90277-8. ISSN 00318914.

[32] KLEINPENNING, T. G. M. Noise of hot carriers in n-type silicon. *Physica B+C*. 1981, **103**(2-3), 340-344. DOI: 10.1016/0378-4363(81)90137-6. ISSN 03784363.

[33] RICQ, S., F. GLASSER and M. GARCIN. Study of CdTe and CdZnTe detectors for X-ray computed tomography.*Nuclear Instruments and Methods in Physics Research Section A: Accelerators, Spectrometers, Detectors and Associated Equipment*. 2001, **458**(1-2), 534-543. DOI: 10.1016/S0168-9002(00)00922-0. ISSN 01689002.

[34] TOYAMA, H., A. HIGA, M. YAMAZATO, T. MAEHAMA, R. OHNO and M. TOGUCHI. Quantitative Analysis of Polarization Phenomena in CdTe Radiation Detectors. *Japanese Journal of Applied Physics*. 2006,**45**(11), 8842-8847. DOI: 10.1143/JJAP.45.8842. ISSN 00214922.

[35] COLA, A. and I. FARELLA. The polarization mechanism in CdTe Schottky detectors. *Applied Physics Letters*. 2009, **94**(10), 102113-102117. DOI: 10.1063/1.3099051. ISSN 00036951.

[36] NIRAULA, M., A. NAKAMURA, T. AOKI, Y. TOMITA and Y. HATANAKA. Stability issues of high-energy resolution diode type CdTe nuclear radiation detectors in a long-term operation. *Nuclear Instruments and Methods in Physics Research Section A: Accelerators, Spectrometers, Detectors and Associated Equipment*. 2002, **491**(1-2), 168-175. DOI: 10.1016/S0168-9002(02)01175-0. ISSN 01689002.

[37] ELHADIDY, H., J. FRANC, E. BELAS, P. HLÍDEK, P. MORAVEC, R. GRILL and P. HOSCHL. Thermoelectric Effect Spectroscopy and Photoluminescence of High-Resistivity CdTe. *Journal of Electronic Materials*. 2008, **37**(9), 1219-122. DOI: 10.1007/s11664-008-0471-y. ISSN 03615235

[38] HOOGE, F. N. 1/f noise sources. *IEEE Transactions on Electron Devices*. 1994, **41**(11), 1926-1935. DOI: 10.1109/16.333808. ISSN 00189383.

[39] XPS Instrumentation. *CasaXPS: Processing Software for XPS, AES, SIMS and More* [online]. [cit. 2016-07-29]. Available online at: http://www.casaxps.com/help_manual/XPSInformation/XPSInstr.htm.

[40] *Thermo Scientific XPS knowledge base* [online]. [cit. 2016-07-29]. Available online at: http://xpssimplified.com/knowledgebase.php

[41] *NIST X-ray Photoelectron Spectroscopy Database* [online]. [cit. 2016-07-29]. Available online at: http://srdata.nist.gov/xps/

[42] *X-ray Photoelectron Spectroscopy (XPS) Reference Pages* [online]. [cit. 2016-07-29]. Available online at: http://www.xpsfitting.com/

[43] WATTS, J. F. High resolution XPS of organic polymers: The Scienta ESCA 300 database. G. Beamson and D. Briggs. 280pp., £65. John Wiley & Sons, Chichester, ISBN 0471 935921, (1992). *Surface and Interface Analysis*. 1993, **20**(3), 267-267. DOI: 10.1002/sia.740200310. ISSN 01422421.

[44] SIMON, A. Group 1 and 2 suboxides and subnitrides — Metals with atomic size holes and tunnels.*Coordination Chemistry Reviews*. 1997, **163**, 253-270. DOI: 10.1016/S0010-8545(97)00013-1. ISSN 00108545

[45] WAGNER, C. D., L. E. DAVIS, M. V. ZELLER, J. A. TAYLOR, R. H. RAYMOND and L. H. GALE. Empirical atomic sensitivity factors for quantitative analysis by electron spectroscopy for chemical analysis. *Surface and Interface Analysis*. 1981, **3**(5), 211-225. DOI: 10.1002/sia.740030506. ISSN 01422421.

[46] MENÉNDEZ-PROUPIN, E., G. GUTIÉRREZ, E. PALMERO and J. L. PEÑA. Electronic structure of crystalline binary and ternary Cd − Te − O compounds. *Physical Review B*. 2004, **70**(3), 035112- 035125. DOI: 10.1103/PhysRevB.70.035112. ISSN 10980121.

[47] NEWTON, D. E., BAKER, L. W. (ed.). *Chemical elements: from carbon to krypton*. Detroit: Gale, c1999. ISBN 078762845X.

[48] RUSSELL, H. N. and F. A. SAUNDERS. New Regularities in the Spectra of the Alkaline Earths. *The Astrophysical Journal*. 1925, **61**, 38-43. DOI: 10.1086/142872. ISSN 0004637x.

[49] LIZÁRRAGA, R., E. HOLMSTRÖM, A. AMÉZAGA, N. BOCK, T. PEERY, E. MENÉNDEZ-PROUPIN and P. GIANNOZZI. Core-level shift analysis of amorphous CdTeO x materials. *Journal of Materials Science*. 2010, **45**(18), 5071-5076. DOI: 10.1007/s10853-010-4419-2. ISSN 00222461.

[50] YILMAZ, E., E. TUĞAY, A. AKTAĞ, I. YILDIZ, M. PARLAK and R. TURAN. Surface morphology and depth profile study of $Cd_{1-x}Zn_xTe$ alloy nanostructures. *Journal of Alloys and Compounds*. 2012, **545**, 90-98. DOI: 10.1016/j.jallcom.2012.08.028. ISSN 09258388.

[51] BOSE, D. N., M. S. HEDGE, S. BASU and K. C. MANDAL. XPS investigation of CdTe surfaces: effect of Ru modification. *Semiconductor Science and Technology*. 1989, **4**(10), 866-870. DOI: 10.1088/0268-1242/4/10/006. ISSN 02681242.

[52] KOWALSKI, B. J., B. A. ORŁOWSKI and J. GHIJSEN. XPS study of CdTe(110) surface oxidation process. *Surface Science*. 1998, **412-413**, 544-554. DOI: 10.1016/S0039-6028(98)00484-1. ISSN 00396028.

[53] BELL, S. J., M. A. BAKER, D. D. DUARTE, A. SCHNEIDER, P SELLER, P. J. SELLIN, M. C. VEALE and M. D. WILSON. Characterization of the metal–semiconductor interface of gold contacts on CdZnTe formed by electroless deposition. *Journal of Physics D: Applied Physics*. 2015, **48**(27), 275304-275318. DOI: 10.1088/0022-3727/48/27/275304. ISSN 00223727.

[54] OLSEN, L., S. KUNDU and M. ENGLEHARD. Effects on Moisture on CdTe Cell I-V Characteristics. In: *2006 IEEE 4th World Conference on Photovoltaic Energy Conference*. Waikoloa, HI, USA: IEEE, 2006, s. 2138-2140. DOI: 10.1109/WCPEC.2006.279927. ISBN 1424400163.

[55] KLYUSHIN, A. Y., T. C. R. ROCHA, M. HÄVECKER, A. KNOP-GERICKE and R. SCHLÖGL. A near ambient pressure XPS study of Au oxidation. *Physical Chemistry Chemical Physics*. 2014, **16**(17), 7881-7886. DOI: 10.1039/c4cp00308j. ISSN 14639076.

[56] HERRMANN, W. A. (ed.). *Synthetic methods of organometallic and inorganic chemistry (Herrmann/Brauer)*. Stuttgart: Georg Thieme Verlag, 2000. ISBN 0865779716.

[57] HEE SHIN, D., J. MIN KIM, C. WOOK JANG, J. HWAN KIM, S. KIM and S. CHOI. Annealing effects on the characteristics of AuCl3-doped graphene. *Journal of Applied Physics*. 2013, **113**(6), 064305-064309. DOI: 10.1063/1.4790888. ISSN 00218979.

[58] GILMORE, I. S. and M. P. SEAH. Ion detection efficiency in SIMS. *International Journal of Mass Spectrometry*. 2000, **202**(1-3), 217-229. DOI: 10.1016/S1387-3806(00)00245-1. ISSN 13873806.

[59] DAVIS, J. R. *Surface engineering for corrosion and wear resistance*. Materials Park, OH: IOM Communications, 2001. ISBN 978-0-87170-700-0.

[60] HOFMANN, J. P., M. ROHNKE and B. M. WECKHUYSEN. Recent advances in secondary ion mass spectrometry of solid acid catalysts: large zeolite crystals under bombardment. *Phys. Chem. Chem. Phys*. 2014, **16**(12), 5465-5474. DOI: 10.1039/C3CP54337D. ISSN 14639076.

[61] *Time-of-Flight Secondary Ion Mass Spectrometry* [online]. IonToF, https://www.iontof.com/tof-sims-secondary-ion-mass [cit. 2016-07-29].

[62] YIN, X. *Indium solubility in α-gallium and gallium-indium eutectic alloys studied using PAC* [online]. Hyperfine Interactions Group, Department of Physics and Astronomy, Washington State University Pullman, Washington 99164, 2011 [cit. 2016-07-29]. Available at: https://research.libraries.wsu.edu/xmlui/handle/2376/4188. Technical Report 2 National Science Foundation Grant DMR 09-04096 Metals Program.

[63] GAGO, R., L. VÁZQUEZ, F. J. PALOMARES, et al. Self-organized surface nanopatterns on Cd(Zn)Te crystals induced by medium-energy ion beam sputtering. *Journal of Physics D: Applied Physics*. 2013,**46**(45), 455302. DOI: 10.1088/0022-3727/46/45/455302. ISSN 00223727.

[64] CHATTOPADHYAY, K., X. MA, J. O. NDAP, et al. Thermal treatments of CdTe and CdZnTe detectors. In:*Hard X-Ray, Gamma-Ray, and Neutron Detector Physics II*. Dan Diego, USA: Proc. SPIE 4141, 2000. DOI: 10.1117/12.407595. ISSN 1996-756X.

[65] REN, J., L. FU, G. BIAN, et al. Spectroscopic studies of CdTe (111) bulk and surface electronic structure. *Physical Review B*. 2015, **91**(23). DOI: 10.1103/PhysRevB.91.235303. ISSN 10980121.

[66] BUGAR, M., E. BELAS, R. GRILL, et al. Inclusions Elimination and Resistivity Restoration of CdTe: Cl Crystals by Two-Step Annealing. *IEEE Transactions on Nuclear Science*. 2011, **58**(4), 1942-1948. DOI: 10.1109/TNS.2011.2159394. ISSN 00189499.

[67] DAVIS, C. B., D. D. ALLRED, A. REYES-MENA, J. GONZÁLEZ-HERNÁNDEZ, O. GONZÁLEZ, B. C. HESS and W. P. ALLRED. Photoluminescence and absorption studies of defects in CdTe and ZnCdTe crystals. *Physical Review B*. 1993, **47**(20), 13 363 - 13 369. DOI: 10.1103/PhysRevB.47.13363. ISBN 10.1103/PhysRevB.47.13363. ISSN 1550-235X.

[68] EVERSON, W. J., C. K. ARD, J. L. SEPICH, B. E. DEAN, G. T. NEUGEBAUER and H. F. SCHAAKE. Etch pit characterization of CdTe and CdZnTe substrates for use in mercury cadmium telluride epitaxy. *Journal of Electronic Materials*. 1995, **24**(5), 505-510. DOI: 10.1007/BF02657954. ISSN 03615235.

[69] WATSON, C. C. R. *Structural defects in CdTe and related materials* [online]. Durham, 1993 [cit. 2016-07-29]. Available at: http://etheses.dur.ac.uk/5500/1/5500_2939.PDF?UkUDh:Cy. Ph.D. thesis. Durham University.

[70] SZELES, C., S. E. CAMERON, J. O. NDAP and W. C. CHALMERS. Advances in the crystal growth of semi-insulating CdZnTe for radiation detector applications. *IEEE Transactions on Nuclear Science*. 2002, **49**(5), 2535-2540. DOI: 10.1109/TNS.2002.803882. ISSN 00189499.

[71] SZELES, Csaba, R. B. JAMES, R. C. SCHIRATO, E. E. EISSLER, D. J. REESE and S. E. CAMERON. Radiation detector performance of CdTe single crystals grown by the conventional vertical Bridgman technique. In:*Hard X-Ray, Gamma-Ray, and Neutron Detector Physics*. San Diego: Proc. SPIE 3768, 1999, s. 98-106. DOI: 10.1117/12.366626. ISSN 1996-756X.

[72] BENSALAH, H., V. HORTELANO, J. L. PLAZA, O. MARTÍNEZ, J. CROCCO, Q. ZHENG, V. CARCELEN and E. DIEGUEZ. Characterization of CdZnTe after argon ion beam bombardment. *Journal of Alloys and Compounds*. 2012, **543**, 233-238. DOI: 10.1016/j.jallcom.2012.07.109. ISSN 09258388.

[73] BUIS, C., E. GROS D′AILLON, A. LOHSTROH, G. MARRAKCHI, C. JEYNES and L. VERGER. Effects of dislocation walls on charge carrier transport properties in CdTe single crystal. *Nuclear Instruments and Methods in Physics Research Section A: Accelerators, Spectrometers, Detectors and Associated Equipment*. 2014, **735**, 188-192. DOI: 10.1016/j.nima.2013.08.084. ISSN 01689002.

[74] SALVIATI, G., P. FRANZOSI, M. SCAFFARDI and S. BERNARDI. Panchromatic cathodoluminescence investigation of defects in CdTe bulk crystals and homoepitaxial layers. *Applied Physics Letters*.**65**, 3257-3259. DOI: 10.1063/1.113026. ISBN 10.1063/1.113026. ISSN 1077-3118.

[75] REESE, M. O., C. L. PERKINS, J. M. BURST, et al. Intrinsic surface passivation of CdTe. *Journal of Applied Physics*. 2015, **118**(15), 155305. DOI: 10.1063/1.4933186. ISSN 00218979.

[76] ROUSE, A. A., C. SZELES, J. O. NDAP, et al. Interfacial chemistry and the performance of bromine-etched CdZnTe radiation detector devices. In: *2001 IEEE Nuclear Science Symposium Conference Record*. IEEE, 2002, s. 2459-2463. DOI: 10.1109/NSSMIC.2001.1009316. ISBN 0780373243.

[77] ZÁZVORKA, J., P. HLÍDEK, J. FRANC, J. PEKÁREK and R. GRILL. Photoluminescence study of surface treatment effects on detector-grade CdTe: In. *Semiconductor Science and Technology*. 2016, **31**(2), 025014. DOI: 10.1088/0268-1242/31/2/025014. ISSN 02681242.

[78] FOCHUK, P., R. GRILL, O. KOPACH, et al. Elimination of Te Inclusions in CdZnTe Crystals by Short-term Thermal Annealing. *IEEE Transactions on Nuclear Science*. 2012, **59**(2), 256-263. DOI: 10.1109/TNS.2012.2187069. ISSN 00189499.

[79] RISCHAU, C. W., C. S. SCHNOHR, E. WENDLER and W. WESCH. Ion-beam-induced damage formation in CdTe at a temperature of 15K. *Nuclear Instruments and Methods in Physics Research Section B: Beam Interactions with Materials and Atoms*. 2012, **272**, 338-341. DOI: 10.1016/j.nimb.2011.01.096. ISSN 0168583x.

[80] STEVIE, F. A. Secondary ion yield changes in Si and GaAs due to topography changes during O 2 or Cs ion bombardment. *Journal of Vacuum Science*. 1988, **6**(1), 76-80. DOI: 10.1116/1.574972. ISSN 07342101.

[81] FERRARI, G., M. SAMPIETRO, G. BERTUCCIO, G. GOMILA and L. REGGIANI. On the origin of shot noise in CdTe detectors. *Applied Physics Letters*. 2003, **83**(12), 2450- 2453. DOI: 10.1063/1.1611648. ISSN 00036951

List of selected publications – published in journals with Impact factor

A1. ŠIK, O., P. BÁBOR, P. ŠKARVADA, M. POTOČEK, T. TRČKA, L. GRMELA and E. BELAS. Investigation of the effect of argon ion beam on CdZnTe single crystals surface structural properties. *Surface and Coatings Technology: ACCEPTED, IN PRINT* . DOI: 10.1016/j.surfcoat.2016.05.006. ISSN 02578972.

A2. ŠIK, O., L. GRMELA, H. ELHADIDY, et al. Study of electric field distribution and low frequency noise of CdZnTe radiation detectors. *Journal of Instrumentation*. IOP, 2013, **8**(C06005), 1-5. DOI: 10.1088/1748-0221. ISSN 17480221.

A3. ŠIK, O., ŠKARVADA, GRMELA, O. ŠIK, P. ŠKARVADA, L. GRMELA, J. ŠIKULA and J. FRANC. Contact quality analysis and noise sources determination of CdZnTe-based high-energy photon detectors. *Physica Scripta*. IOP, 2013,**T157**(2013), 1-4. DOI: 10.1088/0031-8949/2013/T157/014064. ISSN 1402-4896.

A4. ELHADIDY, H., R. GRILL, J. FRANC, O. ŠIK, P. MORAVEC and O. SCHNEEWEISS. Ion electromigration in CdTe Schottky metal–semiconductor–metal structure. *Solid State Ionics*. 2015, **278**, 20-25. DOI: 10.1016/j.ssi.2015.04.016. ISSN 01672738.

A5. ANDREEV, A., O. SIK, L. GRMELA and J. SIKULA. Ageing of Cadmium Telluride Radiation Detectors and its Diagnostics with Low Frequency Noise. *Metrology and Measurement Systems*. 2013-01-1, **20**(3), 385–394. DOI: 10.2478/mms-2013-0033. ISSN 08608229.

A6. KNÁPEK, A., L. GRMELA, J. ŠIKULA and O. ŠIK. Cold Field-Emission Cathode Noise Analysis. *Metrology and Measurement Systems*. 2012-01-1, **19**(2), 417-422. DOI: 10.2478/v10178-012-0036-5. ISSN 0860-8229

Curriculum Vitae

Profesional experience

2012 - 2016	PhD student **Central European Institute of Technology** Analysis of transport and noise properties of CdTe- based IR/ gamma ray semiconductor detectors
2006 – 2009	SMT technician **DuHa system, Brno** Operation of pick-and-place SMT system Prototypes testing, firmware programming, PCB design

Education

1999 – 2003	**Secondary Technical School Zlin,** electrical engineering and radio communications
2003 – 2008	**Brno university of Technology**, MsC degree in programme "Electrical, Electronic, Communication and Control Technology".
2008 – 2016	PhD, **Brno university of Technology**, branch Physical Electronics and nanotechnology. PhD thesis " Study of Transport Properties of CdTe Radiation Detectors".

Fellowships abroad

2014	2 months at Faculty of Engineering and Physical Sciences at the University of Surrey, UK. α particle Time-of-Flight measurements.
2015	2 months at National Research Council of Italy, Lecce division. Current Transient Technique and Pockels effect measurements.

Profesional skills

Skilled in pulsed (Time-of-Flight, Current Transient Technique) methods of semiconductor electrical quantities - charge carrier mobility, lifetime, trapping, direct mapping of electric field distribution by the Pockels Effect, Current voltage and noise characteristics analysis. Currently, I am interested in surface analysis by XPS, Auger Spectroscopy, Low Energy Ion scattering and in vibrathonic methods like FTIR, Raman spectroscopy, Cathodoluminiscence.

Computer and Language Skills

Czech, English (proficient, CEFR C1), Spanish (low) and Russian (low)

Word, Excel, Matlab, Origin – advanced user

Hobbies and interests:

Sports, mainly swimming and cycling, gardening; discovering cultures around the world, literature; physics and new technologies.

Participated Projects:

GA15-05259S, Surface passivation of CdTe/CdZnTe radiation detectors, started 01.01.2015.

GAP102/11/0995, Electron transport, Noise and Diagnostic of Shottky and Autoemission Cathodes, 01.01.2011 - 31.12.2013

GD102/09/H074, Diagnostika defektů v materiálech za použití nejnovějších defektoskopických metod, 01.01.2009 - 31.21.2012